## **POLITECNICO DI TORINO**

# Master's Degree in Materials Engineering for Industry 4.0



# **MASTER's Degree Thesis**

# Optimization of the hot-wire laser additive manufacturing process

## **Supervisors**

Candidate

Prof. Christophe TOURNIER

Barkin AYDIN

Prof. Daniele UGUES

Prof. Cedric BOSCH

Prof. Cedric COURBON

# Erasmus Mundus Joint Master in Manufacturing 4.0 by intElligent and susTAinable technologies



## **MASTER's Degree Thesis**

# Optimization of the hot-wire laser additive manufacturing process

#### **Supervisors**

Prof. Christophe TOURNIER

Prof. Daniele UGUES

Prof. Cedric BOSCH

Prof. Cedric COURBON

#### Candidate

Barkin AYDIN

# September 2025













# **Abstract**

This thesis investigates the optimization of the hot wire laser additive manufacturing (HWLAM) process with a focus on Inconel 718 deposition. HWLAM is a wire-based directed energy deposition technique that combines laser power with resistive wire preheating to improve energy efficiency and deposition stability. Compared to conventional wire laser additive manufacturing (WLAM), the introduction of current as an additional process parameter significantly affects heat input, material flow, and final part quality. In this study, four key process parameters (laser power, current, scanning speed, and wire feeding speed) were systematically examined to evaluate their influence on bead geometry, overall surface quality, and microstructural characteristics. The objective of this work is to define stable process windows that enable defect-free and dimensionally accurate bead production.

A mathematical model was first established to calculate the theoretical wire linear energy required for complete melting of IN718 wire. Guided by this model, a comprehensive set of experiments was performed using a robotized manufacturing cell. In total, 142 parameter sets and around 450 depositions were tested, applying both coarse and fine process mapping strategies. Each deposition was characterized in terms of bead geometry, surface quality, and process defects, while microstructural analyses provided additional insights into dilution, contact angle, and grain morphology.

The results show that successful manufacturing is achieved within a process window centered around the calculated wire linear energy of 8.7 J/mm. It is observed that joule heating should be used as a supplementary source in terms of energy proportions. Introduction of joule heating as additional heat source resulted in smoother depositions. Additionally, much faster deposition rates were achieved using significantly less laser energy than with the WLAM process. This reduces both energy consumption and production time.

# **Acknowledgments**

First of all, I would like to sincerely thank Professor Christophe for his guidance during my internship and for always being approachable and easy to reach. Our weekly meetings and discussions were very valuable, not only for following the progress of the project but also for shaping new questions and my way of thinking along the way. I am very thankful for your patience in listening to all my questions and ideas and for always being ready to help.

I would also like to thank Nicolas and Leo for teaching and helping me with the use of robot cell. Without your support with the robot cell, this project would not have reached this stage. Michéle, I have learned so much thanks to you. I really appreciate your patience in answering all my questions and for all the help you gave me during this process. I hope you enjoy your new work and Châlons-en-Champagne! I would also like to thank Mr. Denis for his assistance with the microstructural analysis and for allowing me to use his lab, as well as Mr. Bonnet for his help with EBSD analysis.

I would also like to thank all the other PhD students and staff at LURPA: Khalil, Michéle, Filippo, Charles, Leo, Alyssa, Baptiste, Marc, Floriane, and Yan. It was a real pleasure to talk with you, get to know you, and spend time in the lab together. I will never forget the table tennis, pétanque, and babyfoot we played (I am still not good enough at babyfoot). Khalil, good luck with your post-doc, and maybe one day we can watch a Fenerbahçe match together in the stadium. I wish Filippo the best of luck with your next crazy idea (maybe cycling across Europe or swimming to England or something).

Finally, I would like to give endless thanks to Jeanne for her constant support and motivation. Thank you for always supporting me through this challenging process (it sounds like I did a PhD, but you know the difficulties outside the lab). I am very happy to have explored Paris, Angers, and Aix with you over these five months. I would like to write much more but I must keep this page short. I'm so happy and lucky to have you in my life. I love you.

# **Table of Contents**

Abstract		I
Acknowle	dgments	II
Table of C	III	
List of Fig	ures	v
List of Tab	oles	IX
Nomencla	ture	X
Chapter 1	Introduction	1
1.1. Wire	Additive Manufacturing Process	1
1.2. Proce	ess Parameters of HWLAM	4
1.2.1.	Wire and Substrate Material	5
1.2.2.	Wire Size	5
1.2.1.	Scanning Speed	5
1.2.2.	Wire Feeding Speed	6
1.2.3.	Input Energy	6
1.2.4.	Laser Types	8
1.2.5.	Wire Feeding Types	9
1.2.6.	Focal Spot Size	12
1.2.7.	Focal Spot Distance	12
1.2.8.	Literature Review on Parameter Selection	13
1.3. Bead	Geometry and Characteristics	15
1.3.1.	Height and Width	15
1.3.2.	Dilution and Contact Angle	16
1.4. Proce	ess Defects of HWLAM	18
Chapter 2	Methodology	21
2.1. Math	ematical Model	21

2.2. Robo	ot Cell	24
2.3. Expe	eriments and Measurements	27
2.3.1.	Experiments	27
2.3.2.	Manufacturing Planning	29
2.3.3.	Measurements	30
Chapter 3	Results and Discussion	31
3.1. Man	ufacturing Results	31
3.2. Bead	l Geometry Results	36
3.2.1.	Laser Power and Scanning Speed	36
3.2.2.	Wire Feeding Speed	37
3.2.3.	Current	38
3.3. Surfa	ace Roughness Results	40
3.3.1.	Laser Power and Scanning Speed	41
3.3.2.	Wire Feeding Speed	43
3.3.3.	Current	43
3.4. Dilut	tion and Contact Angle Results	44
3.4.1.	Laser Power and Scanning Speed	44
3.4.2.	Wire Feeding Speed	46
3.4.3.	Current	48
3.5. Micr	ostructure Results	49
Chapter 4	Conclusion and Future Work	53
4.1.1.	Conclusion	53
4.1.2.	Future Work	54
Appendix	<b>A</b>	55
Appendix	<b>B</b>	56
Annondiv	. C	57

# **List of Figures**

Figure 1 : Classification of different AM processes1
Figure 2 : Schematic representation of the WLAM process [2]2
Figure 3: Geometries manufactured using manually controlled WLAM (a): Multiple-beac
wall. (b): Cutting edge deposited on a chamfered edge, (c): final shape is obtained after
machining. (d): An aero engine casing with three different bosses deposited on the
surface [17]3
Figure 4 : Schematic of HWLAM process
Figure 5 : HWLAM process parameters4
Figure 6 : The schematic of the preheating wire [27]7
Figure 7 : Comparison of pulsed and continuous laser [28]9
Figure 8 : Schematic of two different feeding strategies [8]
Figure 9: Wire positions within a circular Gaussian-profile laser beam with wire feeding
a) Process schematic, b) Different feeding types, c) wire placed at front edge, d) wire
placed at the center, and e) wire placed at the rear edge of the melt pool (top row is for
rear feeding and bottom row is for front feeding) [30]10
Figure 10: Schematic of three-beam laser with internal coaxial wire feeding laser head
[39]11
Figure 11: Example of different beam position configurations [8]. The parameter of
represents the rotation of the robot head around its z-axis relative to the substrate. The
scanning direction is from right to left11
Figure 12: Schematic of three-beam laser: a) transmission characteristic, b) beams at
negative defocus, c) beams at focal plane, and d) beams at positive defocus [37]13
Figure 13 : General shape of beads [8]15
Figure 14: Deposited beads: a) acceptable contact angle b) high contact angle17
Figure 15 : Dripping defect while manufacturing from different angles18
Figure 16: Manufactured single layer beads: a) good manufacturing, b) severe dripping
and c) moderate dripping18
Figure 17 : Stubbing defect while manufacturing19

Figure 18: Manufactured single layer beads: a) good manufacturing, b) moderate
stubbing c) excessive stubbing
Figure 19: Lack of fusion defect while manufacturing20
Figure 20: Manufactured single layer beads: a) good manufacturing, b) lack of fusion. 20
Figure 21: Diagram of the laser-wire interaction with the working distance and heights
relative to the intersection plane and the substrate [8]23
Figure 22: Evolution of the value n as a function of h for a straight inclined wire $[8]$ 23
Figure 23: Wire tip: a) before the start of production, b) after the production25
Figure 24: Picture of the production cell [75]26
Figure 25: Components of the additive manufacturing robot and cell26
Figure 26: Components in Section A in Figure 2527
Figure 27: a) Overview of HWLAM depositions with the target geometry and deposition
strategy. b) Manufactured tracks
Figure 28: Example of selected points (shown as black) for coarse approach when
<i>Vf</i> =2m/min30
Figure 29: Fine approach process mapping test results when $Vf=2$ m/min and k=232
Figure 30: Fine approach process mapping test results when $Vf=3$ m/min and k=233
Figure 31: Fine approach process mapping test results when $Vf=4$ m/min and k=233
Figure 32: Fine approach process mapping test results when $Vf=5\mathrm{m/min}$ and $k=234\mathrm{m/min}$
Figure 33: Safe manufacturing zone when $Vf=2$ m/min and $k=2$ 34
Figure 34: The distribution of laser and current wire linear energy values. Green dots
represent good productions, red dots represent productions where dripping is observed,
and yellow dots represent productions where lack of fusion and stubbing are observed.
35
Figure 35: Distribution of laser energy participation into the system. Participation of
laser represents the ratio of laser wire linear energy (J/mm) to the total wire linear
energy (J/mm)35
Figure 36: Effects of laser power and scanning speed on bead height with varying $Pl$ and
$Vs$ , while the other parameters were kept constant: $Vf = 2m/\min$ and $I = 100A$ 37
Figure 37: Effects of laser power and scanning speed on bead width with varying $Pl$ and
$Vs$ , while the other parameters were kept constant: $Vf = 2m/\min$ and $I = 100A$ 37

Figure 38: Effect of wire feeding speed on bead height with varying $Vf$ , while the other
parameters were kept constant: $Pl=1600W$ , $Vs=1$ m/min and $I=100$ A38
Figure 39: Effect of wire feeding speed on bead width with varying $Vf$ , while the other
parameters were kept constant: $Pl=1600W$ , $Vs=1$ m/min and $I=100$ A38
Figure 40: Effects of current on bead height with varying $I$ and $Vs$ , while the other
parameters were kept constant: $Pl=1600$ and $Vf=2$ m/min39
Figure 41: Effects of current on bead width with varying $I$ and $Vs$ , while the other
parameters were kept constant: $Pl=1600$ and $Vf=2$ m/min39
Figure 42: Roughness profile of track 104 where $Vs = 1$ m/min, $Pl = 1900$ W, $Vf = 2$
m/min and $I = 100A$ 40
Figure 43: Waviness profile of track 104 where $Vs = 1$ m/min, $Pl = 1900$ W, $Vf = 2$
m/min and $I = 100A$ 40
$Figure\ 44:\ Alicona\ images\ of\ two\ different\ tracks\ with\ the\ following\ varying\ parameters:$
a) $Vs = 0.8 \text{ m/min}$ , $Pl = 1000 \text{ W}$ and b) $Vs = 0.8 \text{ m/min}$ , $Pl = 1900 \text{ W}$ . The remaining
parameters were kept constant: $Vf = 2 \text{ m/min}$ and $I = 100 \text{A}$ 42
Figure 45: Effects of laser power and scanning speed on penetration area with varying
${\it Pl}$ and ${\it Vs}$ , while the other parameters were kept constant: ${\it Vf}$ =1m/min and ${\it I}$ =100A45
Figure 46: Effects of laser power and scanning speed on dilution with varying $Pl$ and $Vs$ ,
while the other parameters were kept constant: $Vf=1$ m/min and $I=100$ A45
Figure 47: Effects of laser power and scanning speed on contact angle with varying $Pl$
and $Vs$ , while the other parameters were kept constant: $Vf=1$ m/min and $I=100$ A46
Figure 48: Effect of wire feeding speed on penetration area with varying $Vf$ , while the
other parameters were kept constant: $Pl$ =1600W, $Vs$ =1m/min and $I$ =100A47
Figure 49: Effect of wire feeding speed on dilution with varying $Vf$ , while the other
parameters were kept constant: $Pl=1600W$ , $Vs=1$ m/min and $I=100$ A47
Figure 50: Effect of wire feeding speed on contact angle with varying $\mathit{Vf}$ , while the other
parameters were kept constant: $Pl=1600W$ , $Vs=1$ m/min and $I=100$ A47
Figure 51: Effects of current on a) penetration area and b) dilution with varying $I$ and $Vs$ ,
while the other parameters were kept constant: $Pl=1600$ W and $Vf=2$ m/min48
Figure 52: Effects of current on contact angle with varying $I$ and $Vs$ , while the other
parameters were kept constant: $Pl=1600W$ and $Vf=2m/\min$ 49

Figure 53: Optical microscope image of Bead 138 where $Vs=1$ m/min, $Vf=1.75$ m/min,
<i>I</i> =100A and <i>Pl</i> =1600W50
Figure 54: Optical microscope images of beads with a) $Pl=1000W$ and b) $Pl=1900W$ ,
with all other parameters kept constant: $Vs=0.8 \text{m/min}, Vf=2 \text{m/min}, I=100 \text{A}50$
Figure 55: Optical microscope images of beads with a) $Pl = 1600W$ , $Vs = 1$ m/min,
Vf =1.5m/min, $I$ =100A and $El$ , $w$ = 12.93 J/mm and b) $Pl$ =1600W, $Vs$ =1m/min,
Vf=2m/min, $I$ =115A and $El$ , $w$ = 10.97 J/mm51
Figure 56: EBSD results of two beads produced with the same wire linear energy $El$ , $w=$
7.9 J/mm , but with different energy proportions : a) $Pl=2200W$ and no current; b)
Pl=1000W and $I=105A$ . Other process parameters were kept constant: $Vs=1$ m/min,
<i>Vf</i> =2m/min,
Figure 57: Table of all tested recipes with their process parameters and results55 $$
Figure 58: Experimental and model-predicted bead geometry values with associated
$error\ percentages.\ The\ yellow\ column\ indicates\ the\ bead\ track\ number,\ the\ blue\ columns$
represent the measured (real) height and width, the pink columns show the model-
$predicted\ height\ and\ width, and\ the\ grey\ columns\ present\ the\ corresponding\ percentage$
errors 56

# **List of Tables**

Table 1 : Experimental configurations and parameters recorded in literature14
Table 2 : Effect of Process Parameters on the Bead Geometry16
Table 3: Effect of Process Parameters on the Bead Characteristics17
Table 4: Thermophysical and dimensional properties of Inconel 718 wire [72]21
Table 5: <i>cp</i> values for IN718 [73]22
Table 6: Parameters for process mapping experiments
Table 7: Chemical compositions of IN718 wire and substrate (wt%)28
Table 8: Roughness and waviness values of different tracks with varying laser power and
scanning speed, where $Vf$ =2m/min and $I$ =100A42
Table 9: Roughness and waviness values of different tracks with varying wire feeding
speed, where $Vs=1$ m/min, $I=100$ A and $Pl=1600$ W43
Table 10: Roughness and waviness values of different tracks with varying current, where
VS=1m/min, $Vf=2$ m/min and $Pl=1600$ W44
Table 11: Measurement uncertainty for roughness and waviness parameters. The values
shown represent the expanded uncertainty (±) at the 90% confidence level for each
parameter. Corresponding main measurement values are reported in Section 3.2 of the
main text57

# **Nomenclature**

#### **Abbreviations & Acronyms**

AM Additive Manufacturing

W-LDED Wire Laser Directed Energy Deposition

WLAM Wire Laser Additive Manufacturing

**HWLAM** Hot Wire Laser Additive Manufacturing

DVL Deposited Volume per Unit Length of Travel

#### Other symbols

 $V_f$  Wire Feeding Speed  $\theta$  Contact Angle

 $V_{\rm S}$  Scanning Speed  $\lambda$  Aspect Ratio

 $P_l$  Laser Power  $c_p$  Specific Heat Capacity

I Current  $T_m$  Melting Temperature

 $P_{total}$  Total Power  $T_0$  Room Temperature

 $P_i$  Joule Heating Power T Temperature

 $E_{l,w}$  Wire Linear Energy  $\delta H$  Latent Heat

 $E_{l,t}$  Track Linear Energy m Mass

k Ratio of  $V_s/V_f$  V Volume

 $\dot{m}$  Mass Flow Rate r Wire radius

 $A_w$  Wire Cross Section L Wire Length

 $\rho$  Density  $\pi$  Pi number

W Bead Width E Energy Required to Melt the Wire

A Bead Area n Laser Absorptivity Constant

 $A_p$  Penetration Area R Electrical Resistance

H Height  $ho_e$  Electrical Resistivity

P Penetration Depth  $z_s$  Wire Section and Substrate Distance

*D<sub>t</sub>* Laser Intersection Point

# **Chapter 1**

# Introduction

## 1.1. Wire Additive Manufacturing Process

Additive manufacturing (AM), also known as 3D printing or rapid prototyping, is a process of joining materials to make objects from a 3D model data, usually layer upon layer, as opposed to subtractive manufacturing technologies [1], [2]. As a result, this technology eliminates the need for tools like molds and dies, making it a cost-effective solution for producing customized, high-value, and intricate products in low to medium quantities [3].

To build the parts with AM, a feed material such as a liquid, solid, or powder is transformed into a solid part with the desired shape using a source of energy. Different classifications were made based on the choice of feed material, process, or energy source. ISO/ASTM 17296-2 [4] offers a standard classification according to the process type, whereas alternative classifications based on the type of feed material are also presented in the literature [5], [6], [7], [8]. Figure 1 shows the classification of the different AM processes, organized by process type and feed material state.

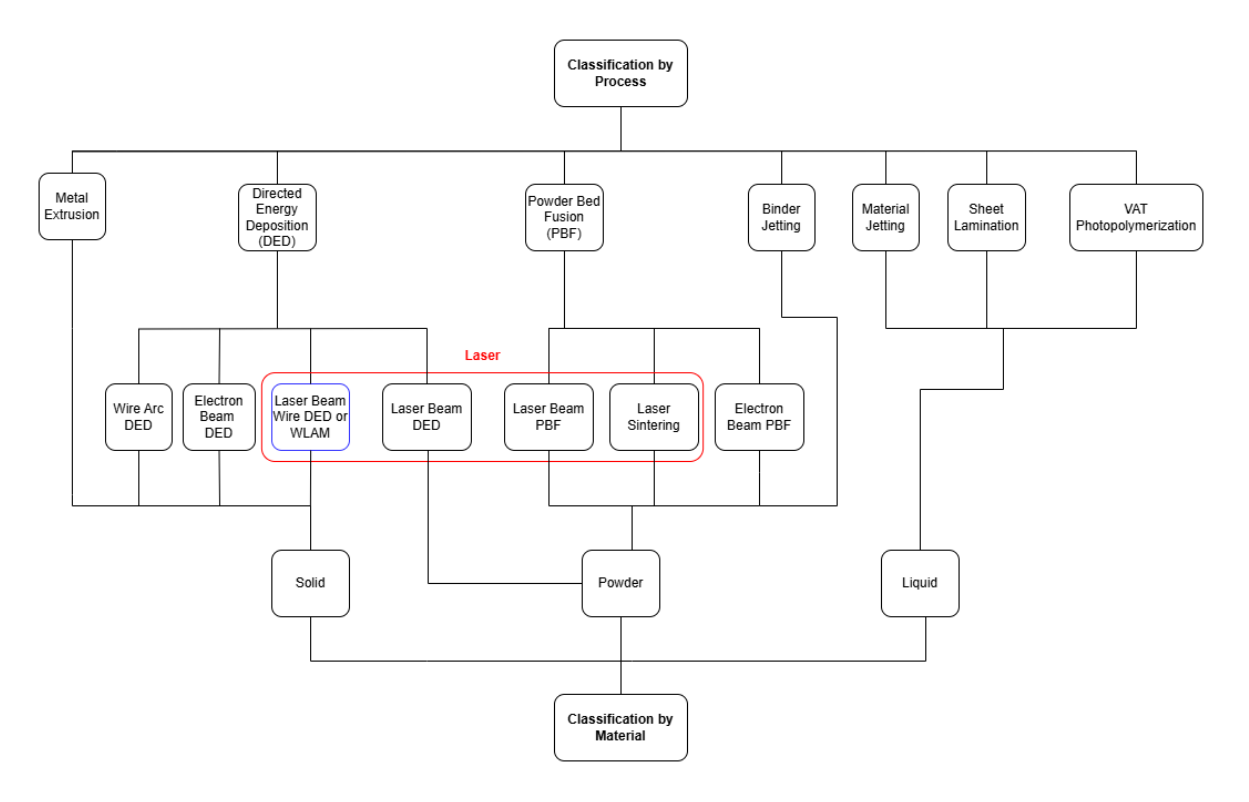
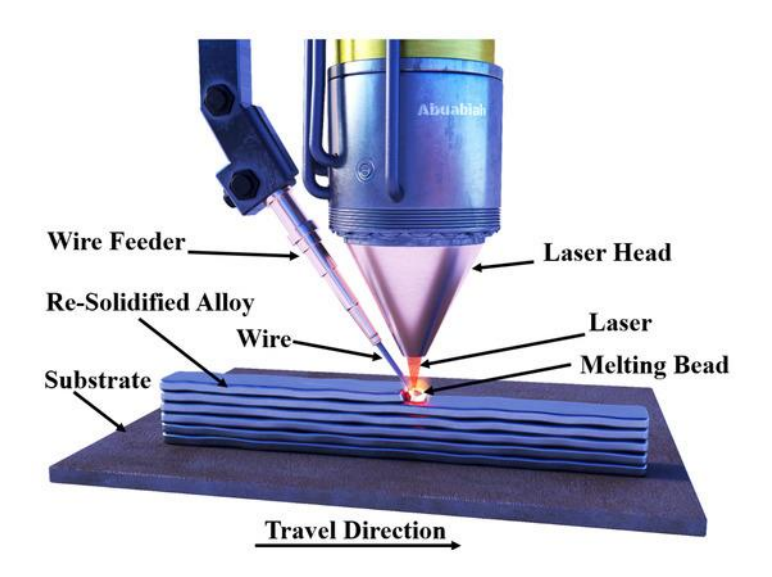


Figure 1: Classification of different AM processes.

Directed Energy Deposition (DED) is a type of AM process where material is deposited and simultaneously melted using a concentrated heat source. Wire or powder are commonly used as a feedstock material [9]. Compared to powder-based feedstocks, wire offers a higher deposition rate [10], [11], reduced material waste [12], lower overall material costs [13] and a lower risk of contamination [14]. Given these advantages, wire-laser directed energy deposition (W-LDED) has emerged as a promising manufacturing technique and is increasingly being adopted in the aerospace, automotive, and energy sectors for the fabrication of large-scale components [15].

W-LDED, also known as wire laser additive manufacturing (WLAM), a technique used for building, repairing, or coating components (Figure 3). In this process (Figure 2), a moving laser source generates a molten pool on the substrate, while a cold metal wire is simultaneously fed and melted into the melt pool. WLAM enables the production of near-net-shape, complex parts with precise material deposition. This approach reduces manufacturing time by eliminating the need for tooling design and production, while also minimizing machining and finishing operations [16].



**Figure 2**: Schematic representation of the WLAM process [2].

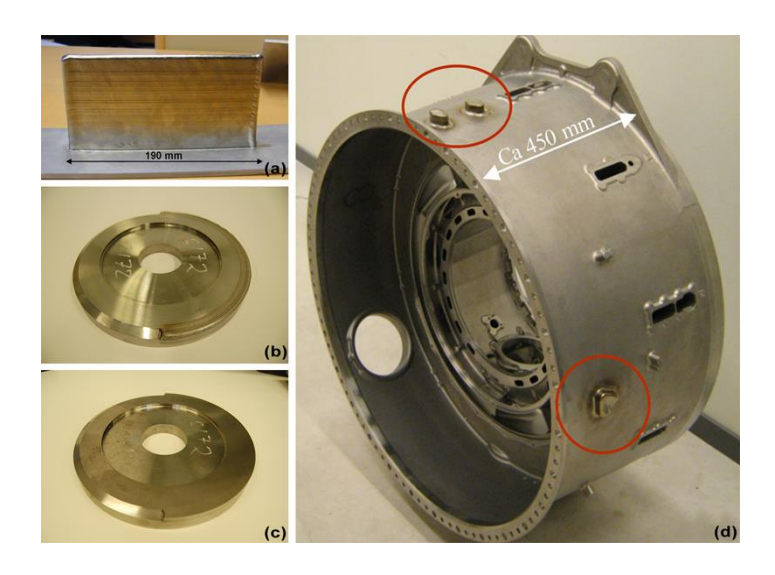


**Figure 3 :** Geometries manufactured using manually controlled WLAM (a): Multiple-bead wall. (b): Cutting edge deposited on a chamfered edge, (c): final shape is obtained after machining. (d): An aero engine casing with three different bosses deposited on the surface [17].

To further improve this technique, researchers have developed a variant known as hot wire laser additive manufacturing (HWLAM). In this method, the use of a hot wire preheated by the Joule effect provides additional benefits by enhancing thermal control and increasing productivity. Here, the energy delivered to the wire is no longer solely dependent on the laser power, allowing for a reduction in laser usage, which in turn decreases both production time and energy consumption. The HWLAM process is illustrated in Figure 4.

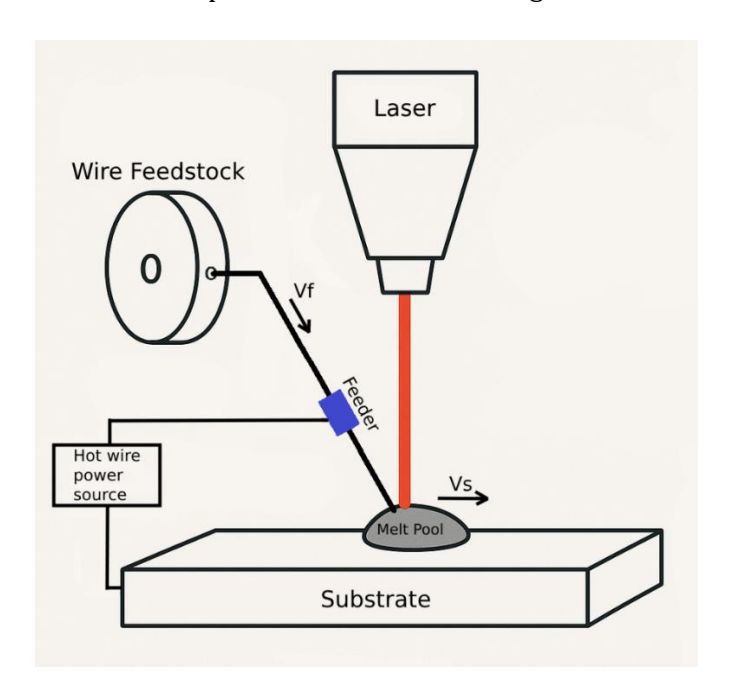


**Figure 4 :** Schematic of HWLAM process.

This study focuses on the HWLAM process, aiming to determine the optimum operating conditions for producing parts of the desired quality. The quality and accuracy of the parts produced using this technique are directly influenced by the process parameters. Unlike WLAM, where current is absent, HWLAM introduces current as a new and key parameter that significantly affects heat input, material flow, and final part quality. Therefore, special emphasis is placed on understanding the role of current, in addition to the other process parameters, and these are investigated in Section 1.2. Then, a mathematical model is presented in Section 2.1 to estimate the production window for HWLAM. In Chapter 2, the production cell as well as the experimental tools and methods are described. Subsequently, the results and conclusions are reported in Chapter 3 and Chapter 4, respectively.

#### 1.2. Process Parameters of HWLAM

The HWLAM process parameters can be classified into five categories (Figure 5). While numerous parameters influence this process, most are fixed and do not vary during manufacturing. The literature and research primarily focus on four key parameters: laser power, current, wire feeding speed, and scanning speed. This study will also focus on these four parameters.

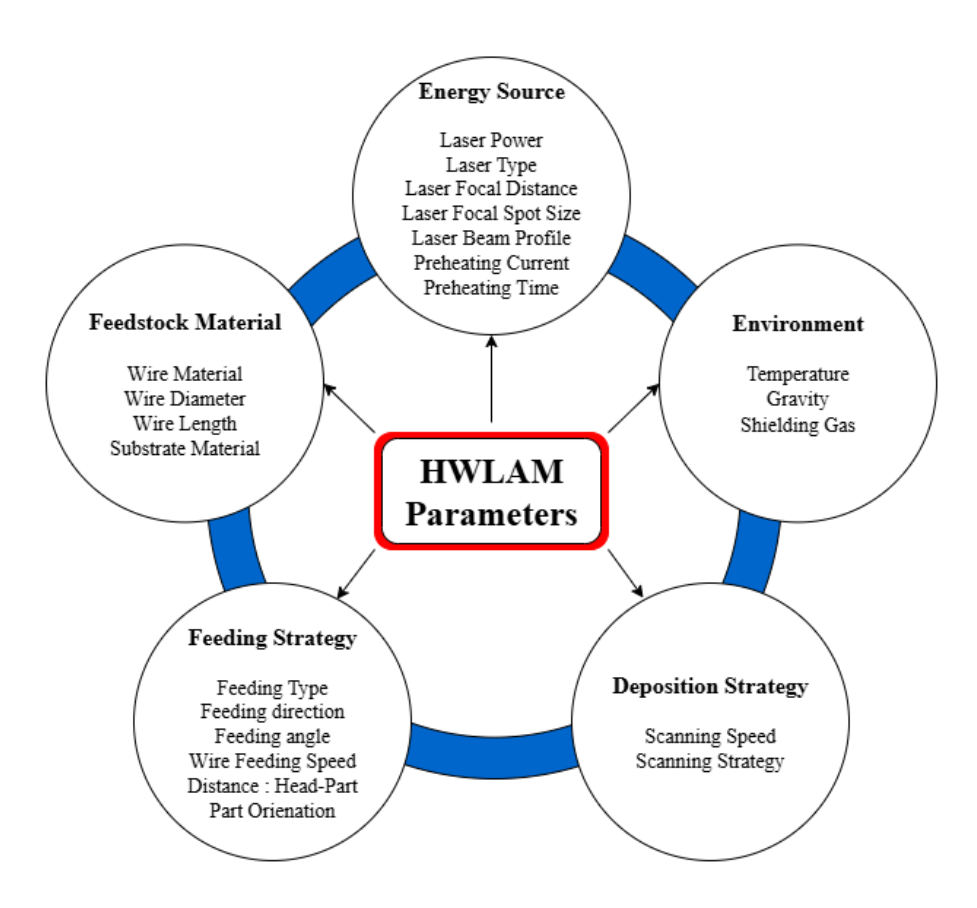


**Figure 5 :** HWLAM process parameters.

#### 1.2.1. Wire and Substrate Material

Since the manufacturing process in HWLAM closely resembles welding, materials commonly used in conventional welding are also well-suited for this technique [8]. This includes:

- Co-Cr based alloys
- · Al based alloys
- Tool steels
- Stainless steels
- Ni based alloys
- Titanium alloys

Material selection is governed by the specific performance requirements and regulatory standards of the intended industry and application. For example, the aerospace sector demands lightweight, high-strength materials such as titanium and nickel-based alloys due to their excellent mechanical properties and resistance to high temperatures [18]. In contrast, the biomedical field emphasizes biocompatibility and corrosion resistance, often utilizing materials like cobalt-chromium alloys and medical-grade stainless steels [19]. In literature, commonly used materials for WLAM and HWLAM are IN718, IN625, Ti-6Al-4V and stainless steel. Material selection has a direct impact on the process parameters. Key material characteristics that affect the process include melting temperature, viscosity, weldability, density, thermophysical properties, and surface tension. Inconel superalloys are widely used in WLAM due to their good weldability, high-temperature strength, and oxidation resistance [20]. Therefore, this material was selected for the present work.

#### **1.2.2.** Wire Size

In the literature, wire diameters used in HWLAM range from 0.1 mm to 1.2 mm, with most studies reporting values around 1.0–1.2 mm (Table 1). The choice of wire diameter may depend on the required dimensional accuracy and the size of the component being produced. Wire size also directly influences the overall process time.

## 1.2.1. Scanning Speed

Scanning speed ( $V_s$ ) is a HWLAM process parameter that refers to the speed at which the laser head moves across the substrate during deposition. Low scanning speed with constant laser power leads to high energy on the track, resulting in deeper melt pool and more energy input per point on the track. Scanning speed has a significant effect on the bead's shape and characteristics, as discussed in detail in Section 1.3.

#### 1.2.2. Wire Feeding Speed

Wire Feeding Speed ( $V_f$ ) is the speed at which the wire is fed into the melt pool. In the literature, a wide range of wire feeding speeds has been reported, depending on parameters such as wire type and size, laser power, current, and scanning speed (Table 1). Too high or too low wire feeding speed can directly cause defects in manufacturing and shape. The effect of wire feeding speed on bead's geometry and characteristics is discussed in detail in Section 1.3.

The ratio of wire feeding speed to scanning speed, often denoted as k (Equation 1.1), determines how much wire is fed per unit distance traveled [21], [22]. Since it largely depends on other process parameters, it is not accurate to define a fixed value for the k ratio. However, studies show that it is commonly set between 1 and 4. Table 1 also presents the typical values for this ratio.

$$k = \frac{V_f}{V_s}$$
 1.1

In HWLAM, higher deposition rates can be achieved compared to WLAM [23]. The deposition rate  $\dot{m}$  is defined in Equation 1.2 [24] and is expressed in g/s. Here,  $A_w$  denotes the wire cross-sectional area in mm<sup>2</sup>. The ratio k makes it easier to represent the volume deposited per unit length of travel (DVL), as shown in Equation 1.4 [25]. DVL is expressed in mm<sup>2</sup>, as it represents the deposited volume per unit length. This parameter is useful for controlling both the deposition geometry and the deposited volume, as it helps prevent overbuilding, underbuilding, and inconsistencies in layer height and width between layers.

$$\dot{m} = \rho \cdot A_w \cdot V_f \tag{1.2}$$

$$DVL = \frac{\dot{m}}{\rho \cdot V_S}$$
 1.3

$$DVL = A_w \cdot \frac{V_f}{V_s} = A_w \cdot k$$
 1.4

#### 1.2.3. Input Energy

In HWLAM, two energy sources are used: a laser and resistive heating by the Joule effect. Sufficient energy input from these sources is essential for producing high-quality deposits, as it ensures complete wire melting and proper fusion with the substrate. Insufficient or excessive energy can result in defects, hindering further fabrication [23]. That is why choosing the right

laser power and preheating current is crucial. A detailed discussion of these defects is presented in section 1.4.

Laser power is responsible for both melting the wire and forming the melt pool on the substrate, while joule heating specifically targets the wire, thereby reducing the laser's contribution to wire heating. Joule heating, also known as Ohmic heating, refers to the generation of heat when an electric current flows through a medium (either solid or liquid) that has finite electrical conductivity [26]. In HWLAM, a circuit containing a wire and substrate is established to achieve joule heating. When the wire makes contact with the substrate, the circuit is completed, allowing an electric current to flow, thereby heating the wire (Figure 6). During the manufacturing process, joule heating must remain active to ensure the quality of the process. This can only be achieved through continuous contact between the wire and the substrate.

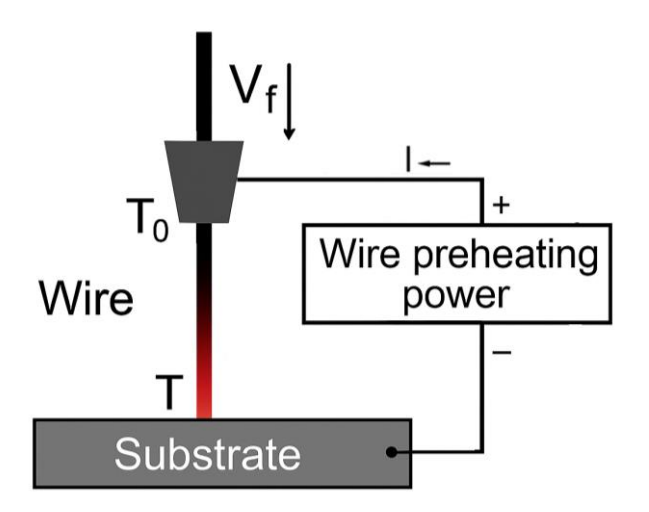


**Figure 6**: The schematic of the preheating wire [27].

In previous studies, a wide range value of laser powers and currents have been used (Table 1). This variation is often influenced by other process parameters such as the material, wire diameter, focal spot size and distance, wire feeding speed, and scanning speed. An optimized combination of laser power and current is crucial to avoid manufacturing defects.

In the literature, the energy input to the wire is commonly represented as linear energy  $(E_{l,w})$  in J/mm, as shown in Equation 1.5. It describes the amount of energy supplied per unit length of wire entering the melt pool. This approach relates the total power input  $(P_{total})$ , which includes contributions from both laser  $(P_l)$  and Joule heating  $(P_j)$ , to the wire feeding speed.

$$E_{l,w} = \frac{P_{total}}{V_f} = \frac{\left(P_l + P_j\right)}{V_f}$$
 1.5

There is also another similar parameter called track linear energy  $(E_{l,t})$ . Unlike wire linear energy, this parameter uses scanning speed instead of wire feed speed (Equation 1.6). It represents the amount of energy applied per unit length of a deposition track.

$$E_{l,t} = \frac{P_{total}}{V_{s}} = \frac{\left(P_{l} + P_{j}\right)}{V_{s}}$$
 1.6

Wire linear energy mainly relates to melting the wire itself; it indicates how much energy is delivered per unit length of wire fed, ensuring the wire melts properly to form the deposited material. While the track linear energy is more about the interaction between the melted wire and the substrate or previous layer. It governs the melt pool size, the fusion and bonding quality.

#### 1.2.4. Laser Types

Laser systems are generally classified as either continuous-wave or pulsed (Figure 7), and each type exhibits distinct behavior, particularly in relation to melt pool formation. Continuous laser causes the melt pool to move along the deposition path, contributing to heat accumulation over time. Conversely, the pulsed laser's periodic energy delivery limits thermal accumulation, thereby reducing residual heat in the material [28]. In most studies (Table 1) the continuous laser was used due to its high deposition rate and high melt pool stability [29].

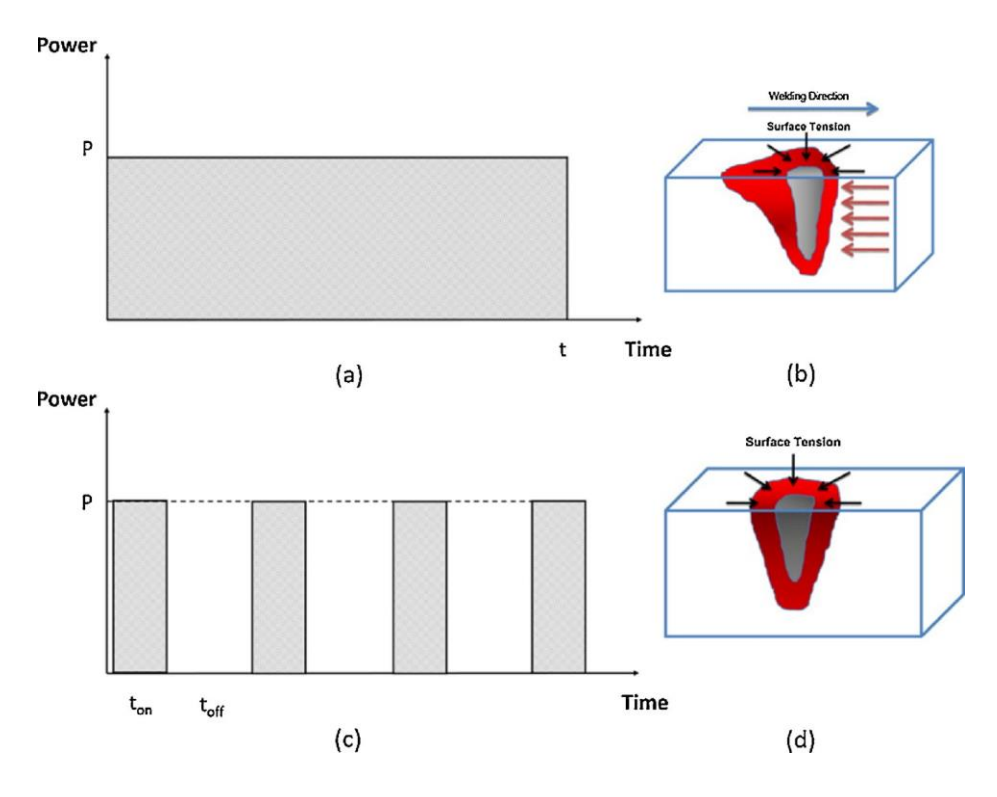
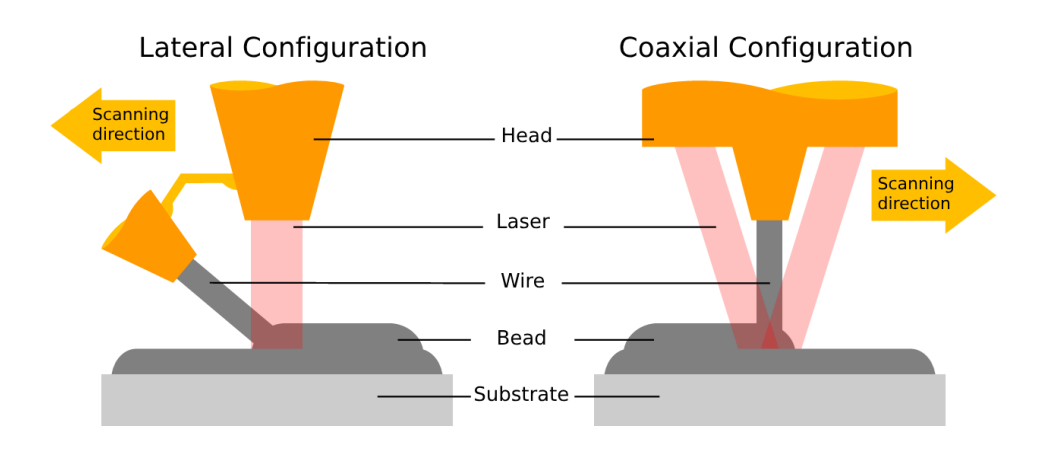


Figure 7: Comparison of pulsed and continuous laser [28].

#### 1.2.5.Wire Feeding Types

In the HWLAM process, two wire feeding strategies are discussed: coaxial feeding and lateral feeding (Figure 8). Depending on the choice of wire feeding strategy, additional parameters such as wire tip position, wire feeding angle, wire feeding direction and wire stick-out length [30] may be introduced or omitted.



**Figure 8:** Schematic of two different feeding strategies [8].

In lateral feeding, the wire can be supplied either front (in the same direction as the laser head movement) or rear (opposite to the laser head movement), with the wire tip positioned at the front, center, or rear of the laser beam (Figure 9) [12], [30].

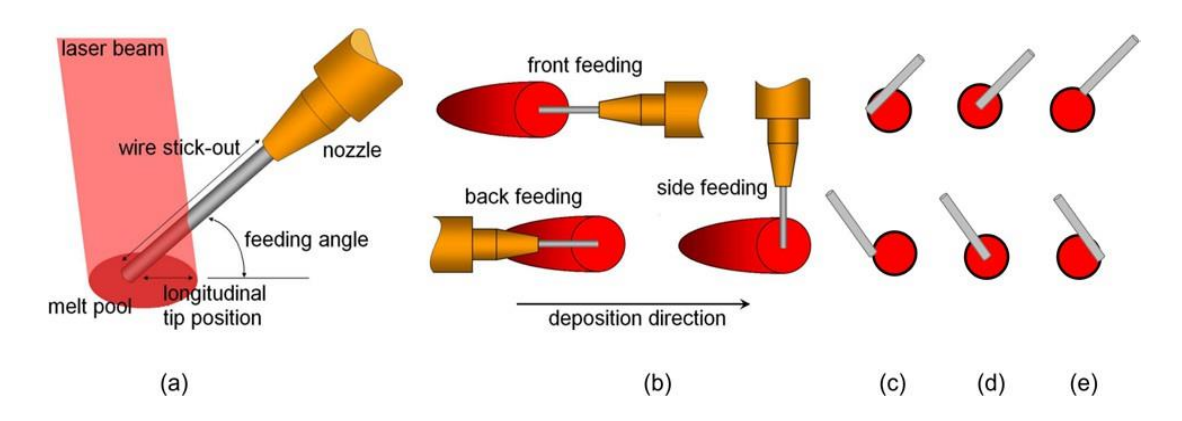


**Figure 9 :** Wire positions within a circular Gaussian-profile laser beam with wire feeding: a) Process schematic, b) Different feeding types, c) wire placed at front edge, d) wire placed at the center, and e) wire placed at the rear edge of the melt pool (top row is for rear feeding and bottom row is for front feeding) [30].

The quality of the deposition can be influenced by the choice of wire feeding mode, the position of the wire tip, and the feeding angle [31]. Mok et al. [32] found that front wire feeding with 45° angle the best feeding orientation. Syed and Li [33] reported that instead of a single optimal feeding strategy, different combinations of feeding orientations and angles could also produce good results. They achieved good deposition in front feeding when the wire was placed at the front of the laser beam, and in rear feeding, a good clad was obtained when the wire was positioned at the rear of the laser beam. Liu et al. [12] found that the rear wire feeding with the wire tip placed at the rear of the laser beam is the optimal position. Huang et al. [34] achieved best deposition rate when the wire feeding angle was 45° with front feeding. Although front feeding is promising, the optimal wire feeding strategy for achieving high-quality deposition depends on other factors such as laser power, spot size, and wire material.

In lateral feeding, achieving a uniform deposit is challenging since multiple feeding directions such as front, back, and side feeding may arise during complex component fabrication. Thus, the lateral wire feeding method limits flexibility and makes controlling the fabrication of complex components more difficult [35].

In coaxial configuration, unlike lateral configuration, the use of coaxial heads eliminates the need for head rotation, wire feeding direction and spot, allowing material deposition in any direction [36]. In this configuration, the laser beam is divided into typically three beams (though it may be four or six) using a prism, and these beams are then directed onto the focal plane by focusing mirrors (Figure 10) [35], [37], [38]. Here, wire is located in the center of multiple single beams (donut shape).

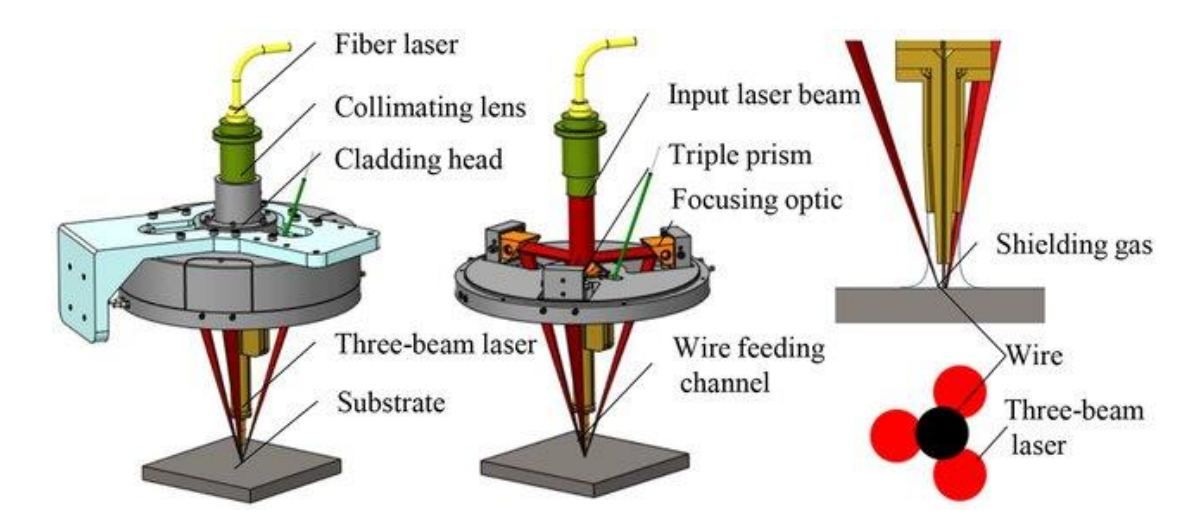


**Figure 10:** Schematic of three-beam laser with internal coaxial wire feeding laser head [39].

Different configurations of the laser beam positions can be achieved by allowing relative rotation of the laser head with respect to the substrate along the z-axis (Figure 11). Roch [8] found that different beam rotation configurations influenced the geometry of the deposited beads; symmetrical beam configurations produced more uniformly shaped beads, whereas asymmetrical configurations led to irregular bead shapes.

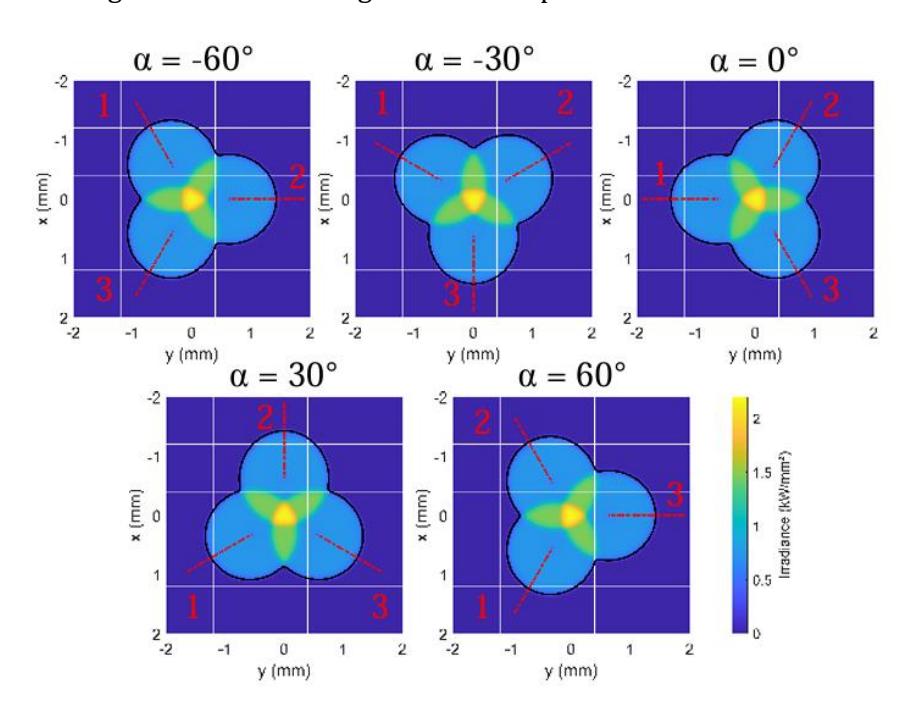


Figure 11: Example of different beam position configurations [8]. The parameter  $\alpha$  represents the rotation of the robot head around its z-axis relative to the substrate. The scanning direction is from right to left.

#### 1.2.6. Focal Spot Size

Focal spot size is an important process parameter that influences the size, depth, and shape of the melt pool. It is found that the smaller laser spot size with a given laser power and scanning speed can lead to an increment in depth of penetration [40]. Thawari et al. [41] showed that increasing the laser spot diameter reduces the melt pool temperature. Additionally, while smaller spot sizes produce narrower melt pools, they tend to be deeper due to more concentrated energy. The authors also suggested that laser power should be increased for larger spot sizes and decreased for smaller ones. It is important to adjust and optimize the spot size for the application, as it affects the size and depth of the melt pool and dilution. This, in turn, influences the metallurgical bonding, as well as the mechanical and microstructural properties of the produced part.

#### 1.2.7. Focal Spot Distance

The laser focal point is the specific location where a laser beam is focused to its smallest diameter, resulting in the highest energy density. Focal position refers to the distance from the laser's focal point to the surface of the workpiece [42]. It is important to adjust this distance since it decides the location of the focus. A high focal position causes the laser beam to focus on the wire, potentially causing the wire to overheat before reaching the melt pool, whereas a low focal position results in inadequate melting of the wire [43]. Since the wire must remain in contact with the substrate to enable joule heating, excessive heating can cause the wire to drip, leading to a loss of contact with the substrate. Moradi et al. [43] and Ji et al. [36] reported that focal spot distance has direct impact on geometry, microstructure and mechanical properties of the printed parts since it has direct effect on temperature and solidification rate.

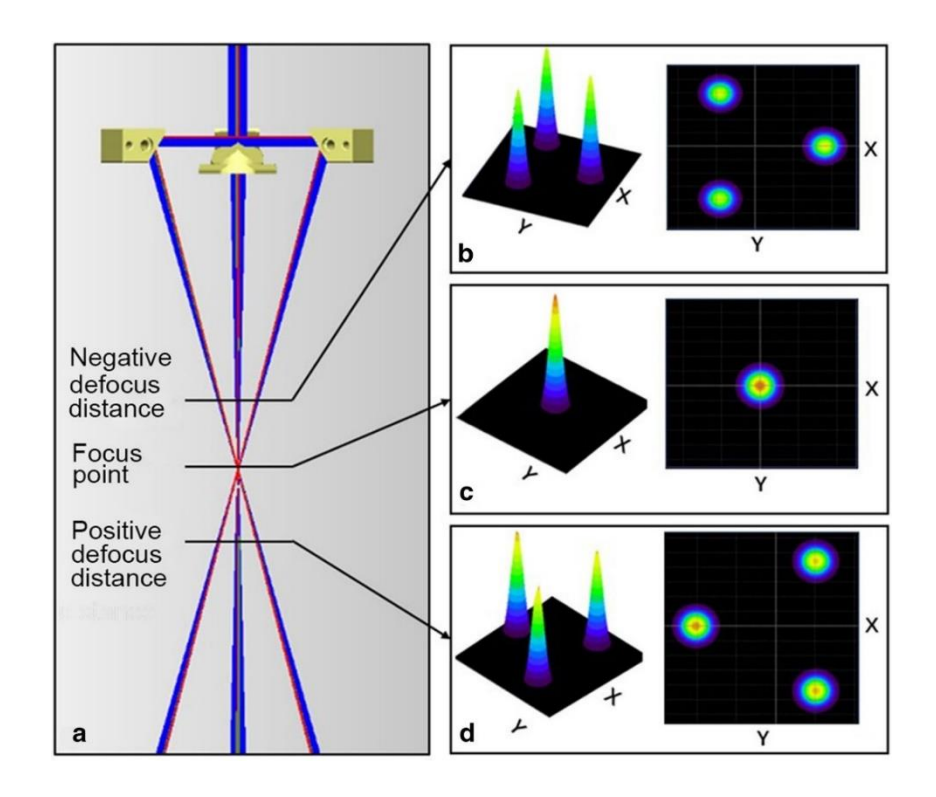


**Figure 12 :** Schematic of three-beam laser: a) transmission characteristic, b) beams at negative defocus, c) beams at focal plane, and d) beams at positive defocus [37].

#### 1.2.8. Literature Review on Parameter Selection

In the literature on HWLAM, the lateral feeding configuration is generally used (Table 1). Additionally, current and laser energy sources are usually considered together rather than separately as laser power and current. So, there is no detailed study in which each process parameter is analyzed individually using a three-beam coaxial head configuration, nor has experimental process mapping been performed under such conditions. This study investigates the effects of current, laser power, wire feeding speed, and scanning speed parameters on bead geometry, surface roughness, microstructure, and defects. At the same time, process mapping is carried out to identify safe operating regions for each wire feeding speed values. Furthermore, compared to the WLAM process, HWLAM aims to achieve lower laser energy consumption and increase the wire feeding speed. In this way, both the energy and time spent in manufacturing are intended to be reduced.

 $\textbf{Table 1:} \ \textbf{Experimental configurations and parameters recorded in literature}.$ 

	Laser Type	Continuous	Continuous	Continuous	Continuous	Continuous	Continuous	Continuous	Continuous	Continuous	Continuous	Continuous	Continuous	Continuous
	Laser Wavelength (nm)	1064	1070	1064	1070	1070	ı	1070		1070	975	1070	940-980	
	k ratio	1.3	1.3-	1.4	1.6	4-6	20	1.6-2	2.5	10.6	20	3.3	4.5-6	7.2-12
ters	Laser Spot Size (mm)	6.0	3	3	33	2-6	1.6	3	2.1	2.5	12x3	1.5		7.85
Manufacturing Parameters	Wire Feeding Rate (m/min)	1.4	3.25-6.25	2-2	5.5	3.6-7.2	6-20	3-4	0.825	9.4	5.4-6	2	0.9-5.4	0.80-3.60
Manufac	Scanning Speed (m/min)	1.08	0.5-4.75	1.5-3.5	3.5	0.9-1.2	0.3-0.5	1.5-2.5	0.5	0.89	0.18-0.3	9.0	0.2-0.9	0.11-0.3
	Laser Power (W)	1000	2400-3600	2000-3500	4000	2000-4000	2000-6000	2000-2500	700	0009	4000-6000	2500-4500	3000-0000	3000
	Preheating Current (A)	72	40-120	0-150	150		164-202	100-120	100-120	300				40-70
	Feeding Angle (°)	06	45	06	45	55	45	45	45		50	18.6		45
	Substrate	Steel	AISI 1045 Steel	S235 steel	316L SS	A36 steel	Steel	Steel	IN718	H13 Steel	A36 steel	SS 2209	Ti-6Al-4V	Ti Grade 2
Material	Wire Diameter (mm)	1	1.2	1	1.2	0.89	1.2	1.2	1	1	1.2	1.2	1.6	1.6
	Wire	IN718	IN625	1N625	IN718	IN625	IN625	IN625	IN718	H13 Steel	316L	SS 2209	Ti-6Al-4V	AMS 4951F
	Article	[44]	[45]	[46]	[27]	[12]	[47]	[48]	[49]	[20]	[51]	[52]	[53]	[54]

## 1.3. Bead Geometry and Characteristics

After describing the process and its parameters, it is important to understand the terminology and characteristics of the produced parts, commonly referred to as bead (Figure 13). In Figure 13, the red area (A) is the area of the bead, the blue area (Ap) is the penetration area, and  $\theta$  represents the contact angle. As mentioned, process parameters have a direct impact on geometry, and their effects are discussed below.

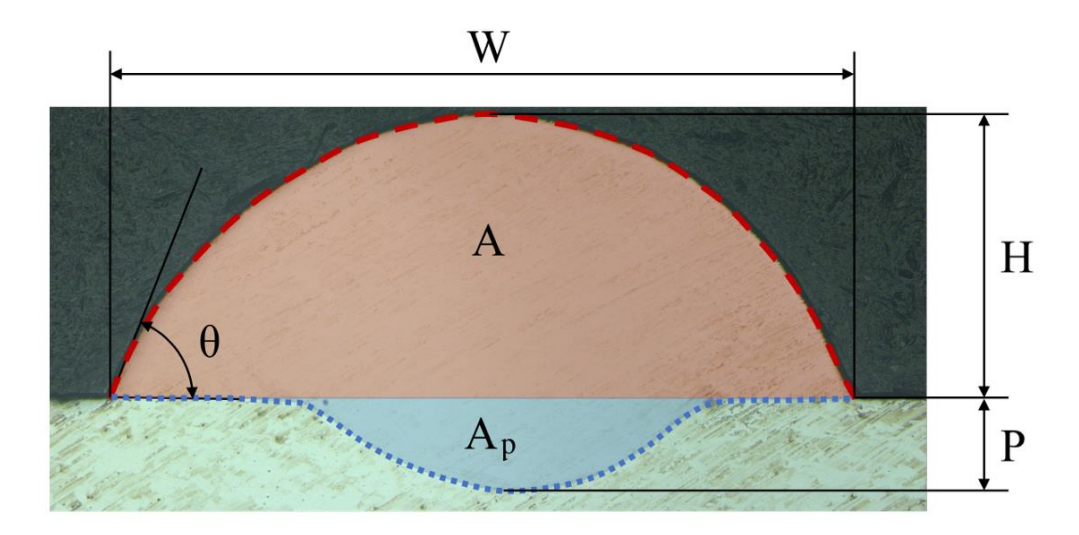


Figure 13: General shape of beads [8].

#### 1.3.1. Height and Width

It is essential to understand how process parameters affect the height and width of the bead to ensure the desired geometry is deposited. According to the literature, increasing the laser power leads to an increase in bead width but a decrease in bead height. Additionally, scanning speed is negatively correlated with bead height and width [12], [32], [34], [53], [55], [56], [57]. However, regarding wire feeding speed, there are inconsistencies in the literature. Some studies reported that an increase in wire feeding speed leads to an increase in both width and height [34], [58], while others reported an increase in height but a decrease in width [57], [59]. These differences may be due to material selection (such as the wetting properties) or the choice of other parameters. For example, the energy input might be insufficient to fully melt the wire when wire feeding speed increases, causing an increase in height but not in width.

In most studies, either only the effect of laser power is examined, or that of a combined heat input. The effect of current alone is usually not investigated, as it is often considered merely as a supporting factor to laser power. Kisielewicz et al. [52] showed that laser power is the most

influential parameter affecting bead height and width. They also found that increasing current improves penetration depth while maintaining bead geometry, thereby avoiding the typical increase in width and decrease in height observed when laser power alone is increased. Caiazzo and Alfieri [59] investigated the effect of the ratio k and found that it is directly related to bead height and inversely related to bead width.

The ratio between bead width and height is referred to as the aspect ratio ( $\lambda$ ) in the literature (Equation 1.7) [12]. A high aspect ratio indicates a flatter bead on the substrate, characterized by a large width and small height. In contrast, a low aspect ratio corresponds to a taller, narrower, balloon-like bead shape.

$$\lambda = \frac{W}{H}$$
 1.7

The general effects of process parameters on bead geometry, as reported in the literature, are shown in Table 2.

**Bead Geometry** Process Parameters W Η λ 1  $P_l$   $\uparrow$  $\downarrow$ 1 ? ?  $I \uparrow$  $V_f \uparrow$ 1 1↓ 1  $V_s$  1 1 **↓**↑ **↓**↑

**Table 2 :** Effect of Process Parameters on the Bead Geometry.

## 1.3.2. Dilution and Contact Angle

In HWLAM, dilution refers to the portion of the base material that melts and mixes with the deposited material. The penetration height (P) (Figure 13), represents the melted base material's depth. Dilution is often expressed as a percentage (Equation 1.8):

$$Dilution (\%) = \frac{A_p}{A + A_p} \cdot 100$$
 1.8

In general, low dilution is desired to maintain a homogeneous microstructure and stable deposition [58], [60], [61]. In contrast, high dilution results in excessive melting of the substrate or the previous layer, a larger heat-affected zone, and greater microstructural inhomogeneity.

The contact angle of the beads is the angle formed between the tangent to the bead profile at its toe and the surface of the substrate or previous layer [62]. This angle can be used to characterize the bead shape: a low contact angle indicates a more spread-out bead on the substrate, which generally means better bonding. In contrast, a higher contact angle may indicate poor bonding or lack of fusion, often resulting in a bead with a balloon-like shape (Figure 14).

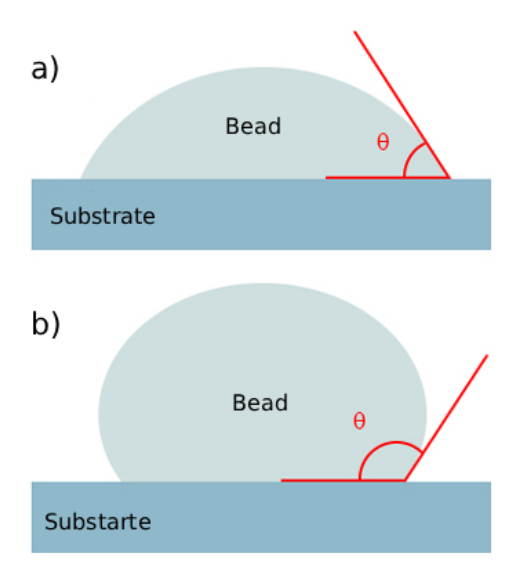


**Figure 14:** Deposited beads: a) acceptable contact angle b) high contact angle.

In the literature, dilution increases with laser power and current but decreases with higher scanning speed and wire feeding speed, whereas the contact angle shows the opposite trend, decreasing with increasing laser power and current and increasing with higher scanning speed and wire feeding rate[32], [55], [56], [57], [58], [60], [61]. The general effects of process parameters on dilution and contact angle are summarized in Table 3.

**Table 3:** Effect of Process Parameters on the Bead Characteristics.

	Bead Geometry			
Process Parameters	Dilution	θ		
$P_l \uparrow$	1	$\downarrow$		
$I$ $\uparrow$	1	$\downarrow$		
$V_f$ $\uparrow$	$\downarrow$	$\uparrow$		
V <sub>s</sub> ↑	$\downarrow$	1		

#### 1.4. Process Defects of HWLAM

As in every manufacturing process, there are process defects that need to be known and described in HWLAM. These defects may arise mainly from selecting inappropriate process parameters or from technological limitations. These defects must be avoided to achieve near net shape geometries.

When excessive energy is supplied to the wire, a defect known as "dripping" occurs. This happens when the molten wire at the tip forms a droplet that detaches from the wire without properly transferring and fusing with the melt pool (Figure 15). This is one of the most critical process defects, as it disrupts the continuity of deposition (Figure 16). Furthermore, since the wire loses contact, joule heating can no longer take place in the system. Dripping generally occurs when too much energy is introduced into the system.



**Figure 15:** Dripping defect while manufacturing from different angles.



**Figure 16 :** Manufactured single layer beads: a) good manufacturing, b) severe dripping and c) moderate dripping.

On the contrary to dripping, the defect known as "stubbing" occurs when insufficient energy is applied to the wire. In this case, the wire contacts and stubs the substrate without melting properly (Figure 17). If stubbing is excessive, the wire may leave the track, bend or damage the substrate due to the pushing force exerted on it. If the stubbing is less severe, the wire may oscillate, and this oscillatory motion can result in non-uniformities in the deposition shape (Figure 18). Here, the joule heating remains active because the wire does not lose contact with the substrate.

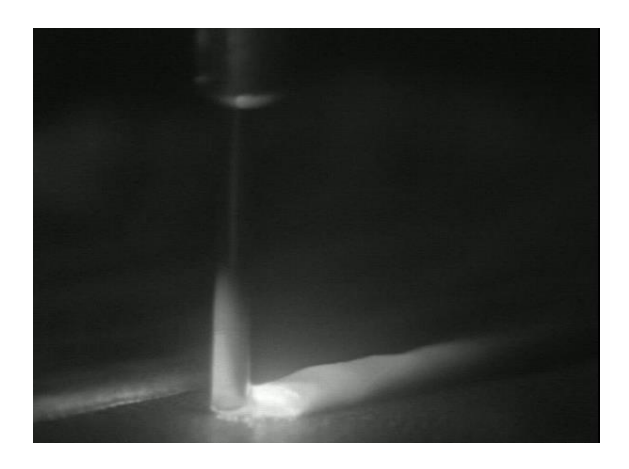


**Figure 17:** Stubbing defect while manufacturing.

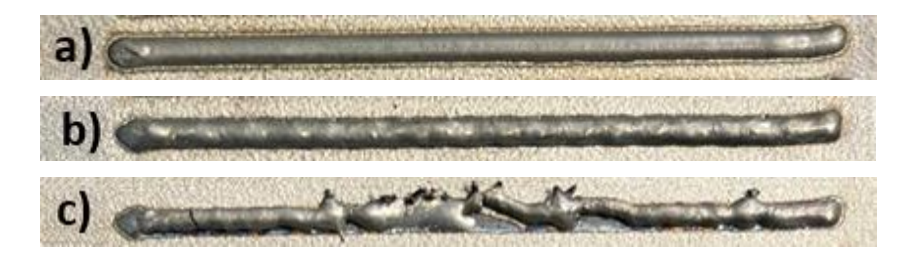


**Figure 18 :** Manufactured single layer beads: a) good manufacturing, b) moderate stubbing c) excessive stubbing.

Low energy input does not only cause stubbing. If the laser power is insufficient for a given scanning speed and wire feeding rate, the defect called "lack of fusion" can occur (Figure 19). In this case, the bonding between the deposited wire and the substrate is inadequate, which may lead to surface defects and joining cracks in the deposited material (Figure 20).

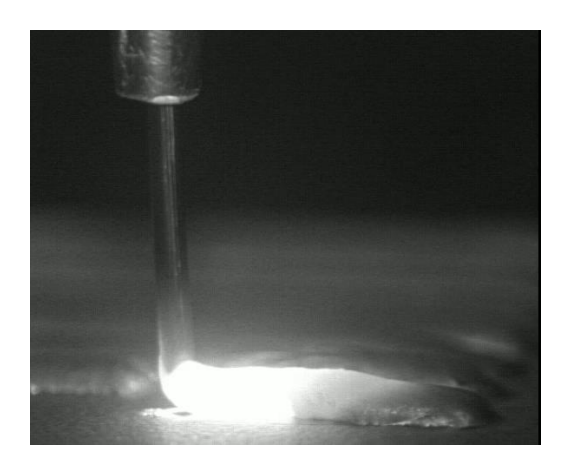


Figure 19: Lack of fusion defect while manufacturing.



Figure 20: Manufactured single layer beads: a) good manufacturing, b) lack of fusion.

The defects previously presented can be easily detected through visual inspection. Conversely, some defects, such as inner cracks and porosities, require more detailed examination due to their small size, which can be observed in parts manufactured using HLWAM. Porosity refers to small voids or pores trapped inside the built material, leading to decreased density and weakened mechanical properties such as fatigue properties, strength and ductility [63], [64]. Porosities occur inside the molten pool due to material property and alloy composition of wire, moisture, hydrogen, trapped shielding gas [64], [65]. Since some process parameters affect the solidification rate, they indirectly influence porosity as well. For example, Fu et al. [66] found that porosity in the beads decreased by preheating the wire in HWAAM process in aluminum alloys. Kobryn et al. [67] showed that gas porosity decreased as scanning speed and laser power increased.

Cracking is a defect that can occur in additive manufacturing processes. There are several types of cracking mechanisms which are hot cracking (solidification cracking), cold cracking (hydrogen induced cracking) and stress relaxation cracking [68]. Hot cracking can occur in the last stage of solidification due to rapid solidification [69]. Hydrogen induced cracking takes place after the material has solidified and is a significant issue, particularly when welding carbon steels and high-strength low-alloy steels [70]. Utilizing high energy density in laser processing leads to a steep temperature gradient, which enhances the possibility of crack formation in the fabricated components due to increased residual stresses [71].

# **Chapter 2**

# **Methodology**

## 2.1. Mathematical Model

Since the main idea of the HWLAM is to melt the wire, it is crucial to calculate the linear energy needed to melt the wire. In this study the material of the wire is IN718. As written in Equation 2.1, the energy required to melt the wire (E) can be calculated by summing the energy needed to raise the wire temperature to its melting point and the latent heat of fusion. Dividing the total energy required to melt the wire by its length gives the wire linear energy (Equation 2.4). Here,  $T_m$  is the melting temperature,  $T_0$  is the room temperature,  $c_p$  is the specific heat capacity,  $\delta H$  is the latent heat,  $\rho$  is the density, r is the radius and L is the length of the wire. The values of those parameters for IN718 are shown in Table 4 and Table 5.

$$E = (\int_{T_0}^{T_m} c_p dT + \delta H) \cdot m$$
 2.1

$$E = (\int_{T_0}^{T_m} c_p dT + \delta H) \cdot \rho V$$
 2.2

$$E = \left(\int_{T_0}^{Tm} c_p dT + \delta H\right) \cdot \rho \pi r^2 L$$

$$E_{l,w} = \left(\int_{T_0}^{Tm} c_p dT + \delta H\right) \cdot \rho \pi r^2$$
2.3

$$E_{l,w} = \left(\int_{T_0}^{Tm} c_p dT + \delta H\right) \cdot \rho \pi r^2$$
 2.4

**Table 4:** Thermophysical and dimensional properties of Inconel 718 wire [72].

$T_m$ (°C)	$T_0$ (°C)	$\delta H(J/g)$	$\rho \left( g/cm^{3}\right)$	r(mm)	L(mm)
1336	25	196.85	8.2	0.6	11

**Table 5**:  $c_p$  values for IN718 [73].

$T(^{\circ}C)$	$c_p(T)\left[\frac{J}{kgK}\right]$
0 < T < 600	$0.13 \cdot T + 411.54$
600 < T < 1000	$0.11 \cdot T + 496.97$
1000 < T < 1200	$0.22 \cdot T + 319.21$
$1200 < T < T_m$	658

$$E_{l,w} = 8.75 J/mm$$
 2.5

The linear energy needed to melt the IN718 is calculated by substituting the values in Table 4, table 5 into the Equation 2.4. The result is shown in Equation 2.5. This value was also calculated and validated experimentally by Roch [8]. By combining Equation 2.5 and Equation 1.5, the theoretical calculation is expressed in terms of the process parameters (Equation 2.8) where I is the current, R is the electrical resistance,  $A_w$  is the cross section,  $\rho_e$  is the electrical resistivity of the wire and n is the energy absorptivity constant.

$$8.75 = \frac{P_l}{V_f} + \frac{P_j}{V_f}$$
 2.6

$$8.75 = \frac{n \cdot P_l}{V_f} + \frac{I^2 \cdot R}{V_f}$$
 2.7

$$8.75 = \frac{n \cdot P_l}{V_f} + \frac{I^2 \cdot \frac{\rho_e L}{A_w}}{V_f}$$
 2.8

The value n was simulated and measured as a function of h by Roch [8] for IN718 wire, (Figure 22). The value of h depends on the relative distance between the wire section and the substrate ( $z_s$ ) as well as the laser intersection point ( $D_t$ ) (Figure 21 and Equation 2.9). Since the wire is not perfectly perpendicular to the substrate and has an approximately 7.5° incline in reality, he plotted the n values for both wire types, such as inclined and straight at different h values. In this work,  $D_t$  was set to -2 mm, corresponding to the n value of approximately 1.2. Additionally, the value of  $\rho_e$  was set to 1.35 × 10<sup>-6</sup>  $\Omega$ ·m [73], [74] and was assumed to remain constant throughout the process, neglecting the temperature dependence.

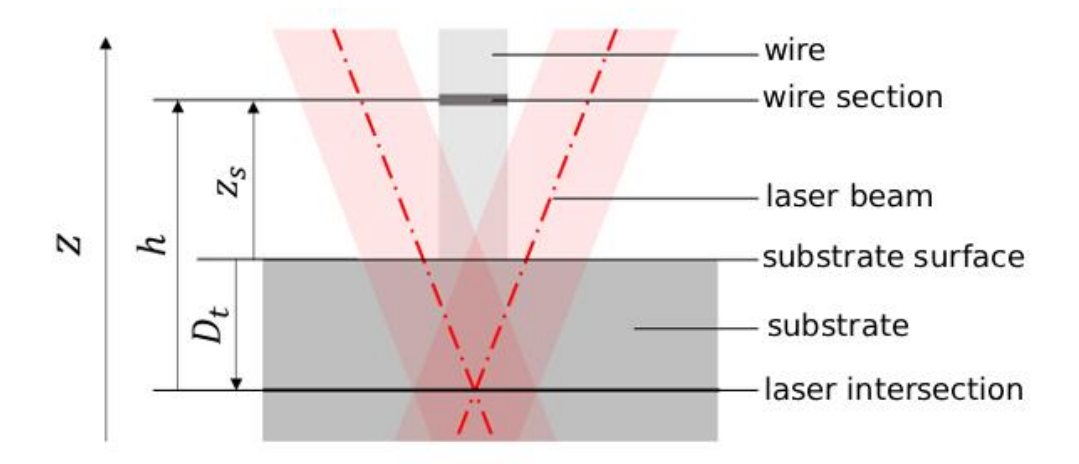


**Figure 21:** Diagram of the laser-wire interaction with the working distance and heights relative to the intersection plane and the substrate [8].

$$h = z_s - D_t 2.9$$

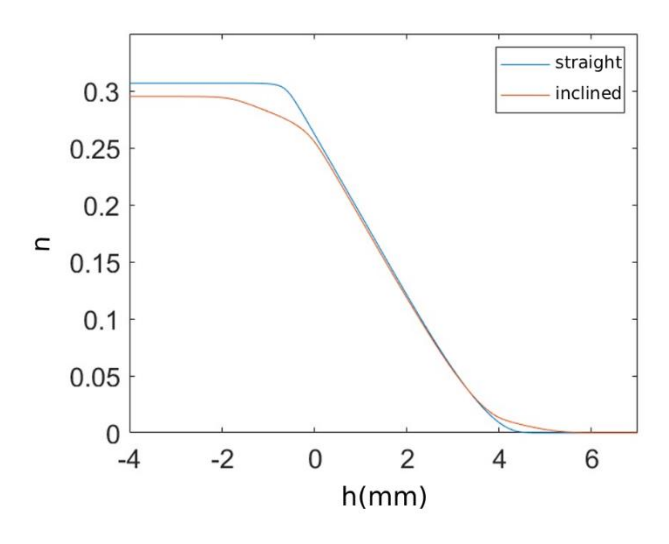


**Figure 22:** Evolution of the value n as a function of h for a straight inclined wire [8].

#### 2.2. Robot Cell

The experiments were conducted at the Laboratory for Research in Automated Production (LURPA) at ENS Paris-Saclay. The cell (Figure 24) includes:

- An orange ABB IRB 6640-185/2.8 robot fitted with a machining spindle
- A white ABB IRB 4600-45/2.05 robot equipped with the laser-wire additive manufacturing head
- An ABB IRBP A-250 positioner, which supported the vice holding the substrate

The cell and the components are shown in Figure 24, Figure 25, and Figure 26.

A coaxial laser head was used for the process. The head is equipped with an IPG™ YLS-4000 fiber laser of 4000 W continuous power, with a wavelength of 1070 nm. Its operating range is between 400 W and 4000 W. An optical fiber carries the beam to the head, and it divides the original laser beam into three separate beams that are arranged in a conical pattern, while feeding the wire through the center axis of the cone. The optical components that split and align the beams are rigidly mounted within the head. By adjusting the position of the laser head and its optics, both the beam size and power can be controlled. The configuration of the laser beam which was used for experiments is not axisymmetric, noting that asymmetric configurations can cause uneven energy distribution in the melt pool. Roch [8] investigated various configurations and their impact on weld bead quality. In this study, the "standard" setup is applied, where two beams are placed behind and one beam ahead of the scanning direction, promoting symmetrical deposition and reducing defects.

The wire is fed to the center of the nozzle from a DINSE™ spool with a maximum speed of 6m/min. This spool is located outside of the cell and pushes the wire using its own rollers. The wire is protected and connected to the HWLAM robot head with a flexible plastic sheath. For heating the wire, DINSE DIX HW 300 PULS power source was used with a DIX CM 592.HW cooling module. To cool down the laser head, a SMC thermo-chiller (model HRR018-AF-20-MT) was used, using water circulation as the cooling medium.

Proper centering of the wire and precise height adjustment, both of which are done manually, are essential to ensure symmetric energy distribution and consistent production. Adjustment screws on the head are used to correct the wire's position and make sure it is properly centered within the laser beams, as the wire can sometimes shift away from the center of the laser spots. For the height adjustment, the tip of the nozzle is automatically positioned at the planned point for production, which is 11 mm relative to the substrate. Then, the wire is manually fed until it reaches the substrate. When contact is detected, the feeding must be

stopped, and this is recorded in the system. The wire making contact is important to precisely achieve the 11 mm distance and to benefit from the joule heating effect. Excessive contact causes the laser head to be pushed backward and results in the wire length being recorded in the system as longer than 11 mm which also affects the position of the focal point. Additionally, after each production, the wire tip is cut and filed to be smooth (Figure 23). This is important to ensure that the contact area is as flat as possible.

During production, the cell remains closed to ensure safety, so cameras are installed inside the cell. A Xiris XVC-1000/1100 welding camera is used to record the process. Thanks to this camera, errors, issues, and other events occurring throughout production can be observed. Real-time monitoring is essential to determine whether the process is running smoothly or if any problems arise.

Additionally, a coaxial E-MAqS camera captures images of the molten pool by looking through the laser's optical path. This camera is connected to the LompocPro software, which monitors the molten pool temperature. Based on the images, the software calculates the average temperature of the melt pool.

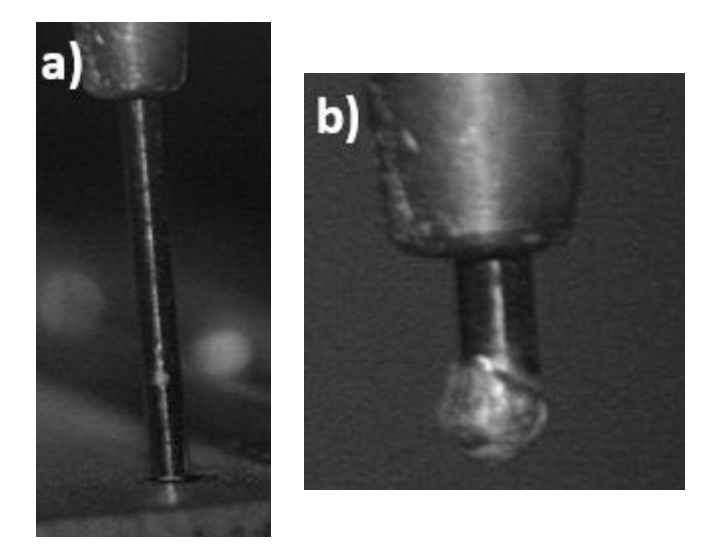


**Figure 23:** Wire tip: a) before the start of production, b) after the production.

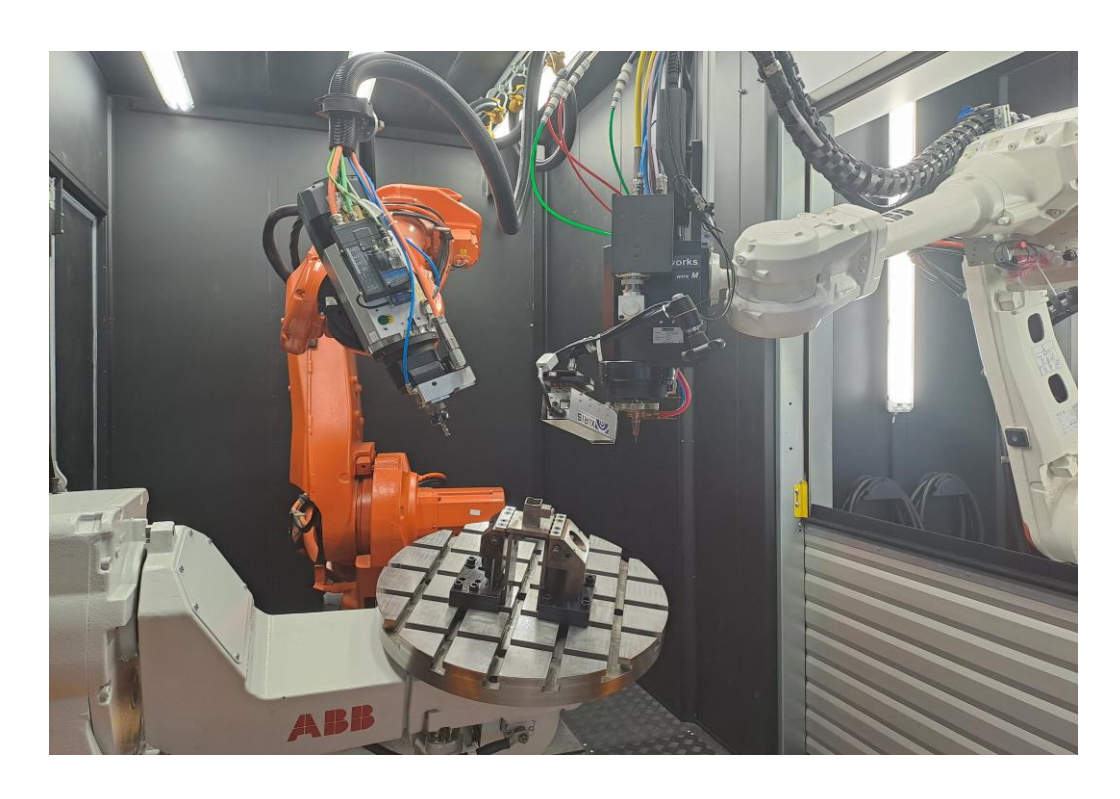


**Figure 24:** Picture of the production cell [75].

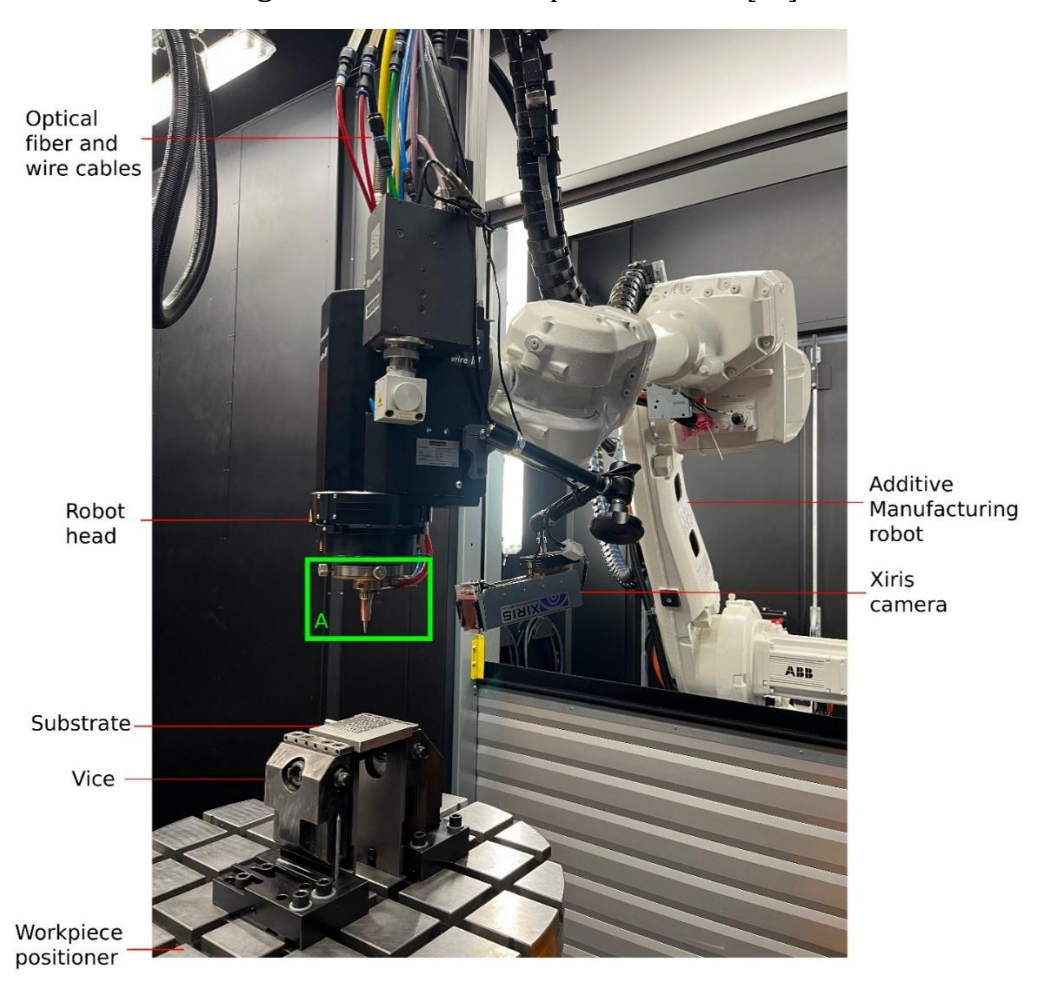
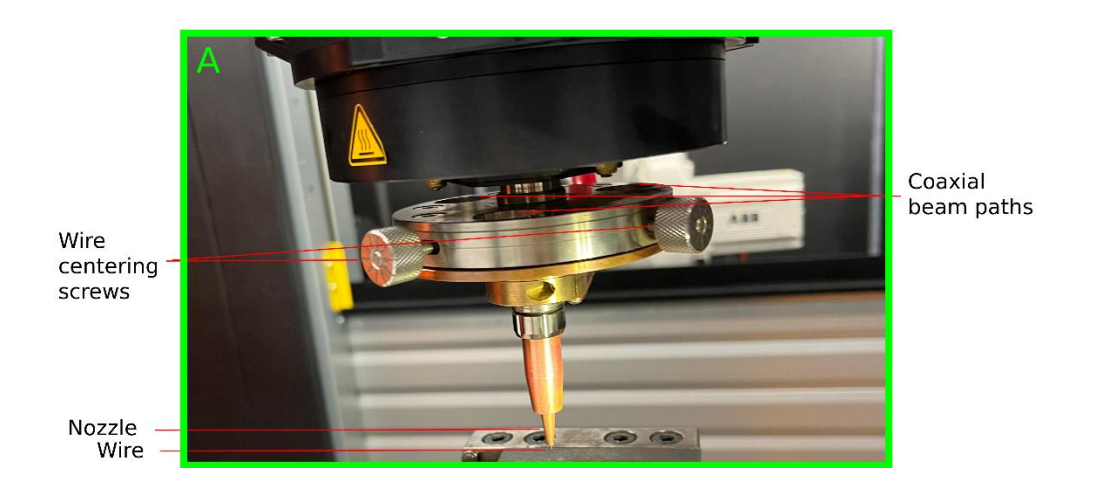


Figure 25: Components of the additive manufacturing robot and cell.



**Figure 26:** Components in Section A in Figure 25.

## 2.3. Experiments and Measurements

### 2.3.1. Experiments

The experiments can be divided into two categories. The first set of experiments was conducted to map the process, while the second set focused on evaluating the effect of process parameters on the bead characteristics.

The values for the process mapping experiments are presented in Table 6 and the composition of the wire and substrate are presented in Table 7. In these tests, four different  $V_f$  were selected: 2, 3, 4, and 5 m/min. Throughout all experiments, the parameters k and preheating time were kept constant at 2 and 0.2s, respectively. Preheating time represents the time that wire is heated by joule heating before the start of the process. After this period, the laser is activated, and both the laser head and wire begin to move. The  $P_l$  and I values were varied according to the mathematical model with an upper limit of 2000 W and 250 A, respectively. The reason laser powers above 2000 W were not tested is that Roch [8] used a 2200W laser power in the process he described as optimal for cold wire laser additive manufacturing at low wire feeding speeds. In the HWLAM process, however, the aim is to operate with lower laser power.

**Table 6:** Parameters for process mapping experiments.

Parameter	Value
$P_l$	750-2000 W
I	20-250 A
$V_f$	2, 3, 4, and 5 m/min
k	2
Preheating time	0.2
Shielding Gas	Argon (%99.9999)
Substrate	IN718 (90 × 90 × 13 mm)
Wire	IN718 (Ø1.2 mm, L = 11 mm)

**Table 7:** Chemical compositions of IN718 wire and substrate (wt%).

Part	С	Cr	Mo	Ni	Ti	Al	Nb	Fe	В	Со	Cu	Mn	P	Si
Wire	0.04	19	3.05	52.5	0.9	0.5	5.13	Bal.	-	0.5	-	-	-	-
Substrate	0.052	18.4	3.03	52.6	1.02	0.53	4.92	Bal.	0.004	0.52	0.06	0.24	0.009	0.09

For process mapping tests, each recipe was repeated 3 or 4 times to determine whether it was classified as good or bad. The deposition was considered "good" if the deposition was smooth, exhibited sound bonding between the melted wire and the substrate, and showed consistent geometrical continuity. If defects such as dripping, lack of fusion, or extreme stubbing occurred, the deposition was classified as "bad". In cases where moderate stubbing was observed, the deposition was labeled as "moderate". Recipes were defined as good only if they achieved at least 75% success in the repeated tests, which corresponds to a 3 out of 3 or 3 out of 4 success rates.

In the process parameter effect tests, all other parameters were kept constant while only the parameter of interest was changed to observe its effect. This was done to all 4 parameters  $(V_f, V_S, P_l, I)$ .

Each deposition is 65 mm in length. At the beginning and end of each deposition, a gap of 15 mm and 10 mm, respectively, is left from the substrate. These gaps are used both for numbering the depositions and for clamping the substrate. The deposition starts from the right side of the substrate and ends on the left side (Figure 27). After each deposition is completed, as described in Section 2.2, the tip of the wire is flattened, and height and centering adjustments

are made for the next deposition. The new deposition begins 5 mm below the previously produced deposition. In total, 17 depositions are made on one side of the substrate.

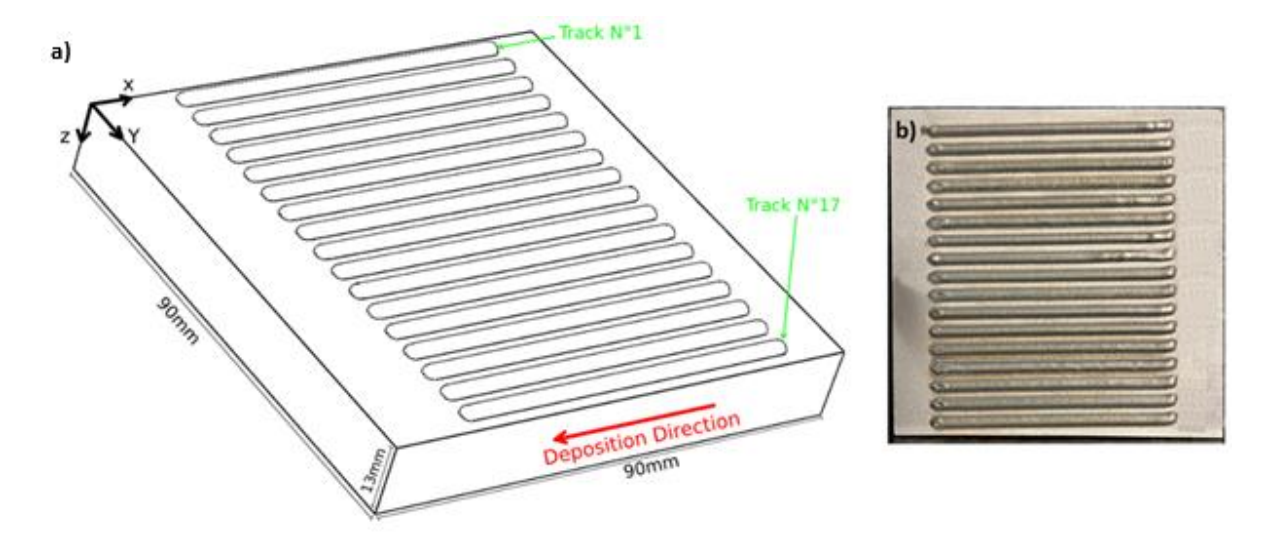


**Figure 27:** a) Overview of HWLAM depositions with the target geometry and deposition strategy. b) Manufactured tracks.

## 2.3.2. Manufacturing Planning

To avoid random process parameter selection and to prevent wasting time and resources, it is essential to plan a manufacturing path. First, a method referred to as the coarse approach was applied. In this approach, the upper and lower limit points of the desired working region were selected (Figure 28). Based on the results of these points, new points were determined accordingly. If two points resulted "bad", no additional points needed to be tested between them, as they were also expected to be bad. Similarly, if two points produced "good" results, no further testing was conducted between them, as good results were anticipated. This approach helped eliminate unnecessary testing. Following the coarse approach, a method involving testing more points was implemented, referred to as the fine approach. Figure 28 is an example of how coarse approach point selection and the chart version of Equation 2.8 looks like. Since some parameters in the mathematical model were assumed to be constant or neglected, isolines for 11 J/mm and 7 J/mm were also included, in addition to the required 8.7 J/mm energy line for wire melting. In all charts, the upper and lower white isolines represent wire linear energy values of 11 J/mm and 7 J/mm, respectively, while the red line represents the theoretically calculated value at Section 1, which is 8.7 J/mm.

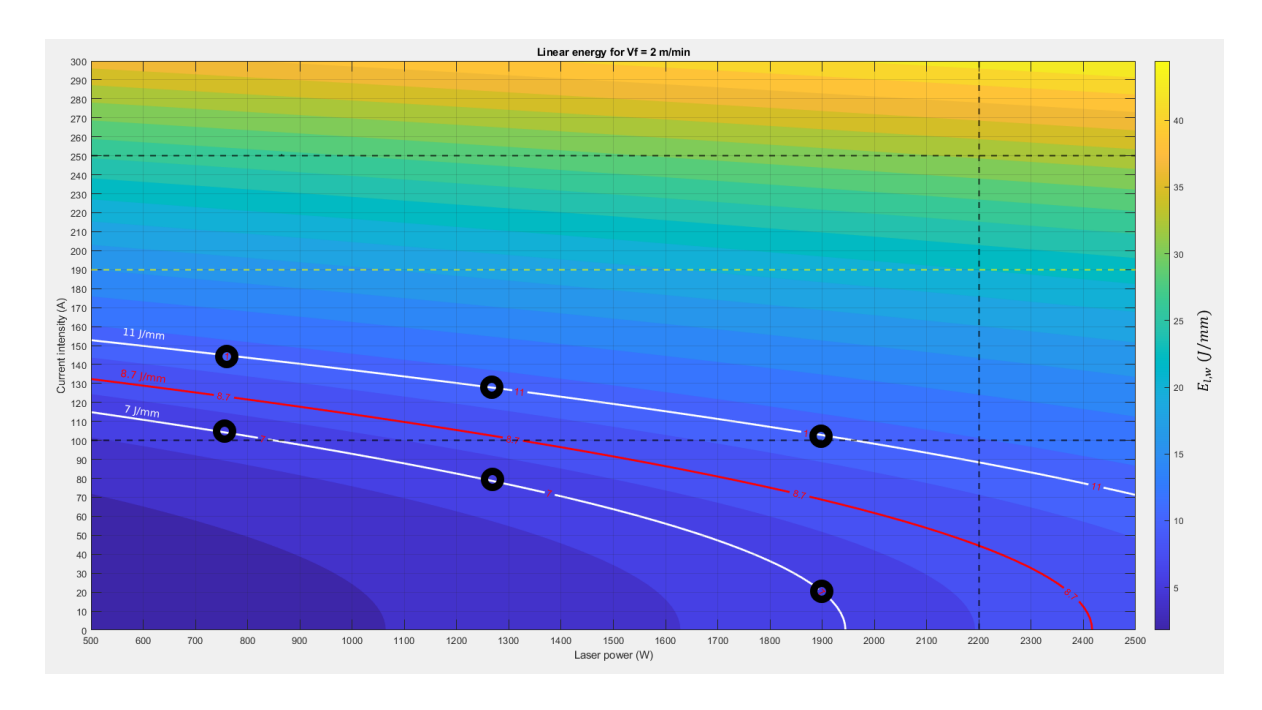


**Figure 28:** Example of selected points (shown as black) for coarse approach when  $V_f$ =2m/min.

#### 2.3.3. Measurements

After manufacturing, the height and width of the acceptable beads were measured using an Alicona IF-SensorR25 optical 3D microscope. Each track was measured once at the beginning, middle, and end points. Since each recipe was repeated 3 to 4 times, a total of 9 or 12 measurements were obtained per recipe.

For surface roughness and profile analyses, a Taylor Hobson Surtronic 25 stylus profilometer was used. A 25 mm measurement was performed from the end to the beginning of the track using a 2  $\mu$ m stylus tip. Each track was measured three times from different starting points, resulting in 9 or 12 measurements per recipe. A cutoff of 0.8 mm and 2.5 mm was applied to extract the roughness and waviness values, respectively.

For porosity, microstructure and dilution analyses, the tracks were cut at their midpoints using Electrical Discharge Machining (EDM), exposing the bead cross-sections in the build plane (ZY plane). A brass 0.25 mm diameter wire was used for cutting, with a wire speed of 10 m/min and a feed rate of 1 m/min. After cutting, the cross-sections were polished using SiC abrasive papers of 320, 800, 1200, and 2000 grit, followed by polishing with 3  $\mu$ m and 1  $\mu$ m diamond suspensions to achieve a mirror-like surface finish [76]. Finally, a chemical-mechanical polishing step was carried out using OP-S NonDry colloidal silica suspension for 10 minutes to reveal the microstructure. ImageJ tool is used for calculation of dilution, penetration area and contact angle.

## **Chapter 3**

## **Results and Discussion**

## 3.1. Manufacturing Results

Results of the fine approach method for different  $V_f$  values are listed below. In Figure 27, when both laser power and current values are low (on the left side of the 7 J/mm line), Lack of fusion was observed. When the current increases while keeping laser power low (on the left side of the 11 J/mm line), dripping occurs. This is not surprising, since the required linear energy to melt the wire was theoretically calculated as 8.7 J/mm. Conversely, at relatively high laser power levels, good depositions were observed even along both low and high energy lines. Since current is directly applied to the wire, whereas a portion of the laser power is reflected, it is considered that current has a more direct and sensitive effect.

The wire linear energy lines shift upward due to the increase in wire feeding speed, as can be seen from Figure 29 to Figure 32. The upward shift of these linear energy lines indicates that higher current values are being applied. This results in a reduced number of good track outcomes. At current values above 200 A, dripping was always observed. When the wire contacted the substrate, it melted very quickly. One possible explanation is that at high current levels, the thermomechanical effects, which were often neglected in the mathematical model, may become more influential. This suggests that at higher  $V_f$  values, lower laser powers and selected upper limit value (2000W) are not suitable. Laser powers above 2000 W should be tested to decrease the contribution of current.

Based on the tests conducted, it was observed that the 8.7 J/mm linear energy line yielded the best results when  $V_f$  was equal to 2 and 3 m/min. Additionally, for a detailed examination of the proportions of laser and current in the total wire linear energy delivered to the system, all test results are compiled into a single graph (Figure 34). Here, the current wire linear energy (J/mm) refers to the linear energy supplied to the wire by the electrical current, while the laser wire linear energy (J/mm) refers to the energy delivered to the wire by the laser power. More successful productions are achieved when the ratio of laser to current energy is balanced (close to one) or when the laser proportion is higher. In cases where the current energy is higher, dripping occurs, while stubbing and lack of fusion are observed when both current and laser energies are low. The maximum number of good recipes is achieved when the ratio of laser

wire linear energy to total wire linear energy is between 0.4 and 0.6 (Figure 35). This is likely because most tests were carried out within the 0.3–0.6 range. Notably, all recipes resulted in good outcomes when the laser ratio was equal to or higher than 0.5. This supports the idea of using joule preheating as a supplementary heat source, while maintaining the laser power as the primary source of energy.

With WLAM, Roch [8] achieved maximum wire feeding speed of 4.2m/min while using 4000W laser power. In contrast, with HWLAM, a wire feeding speed of 5 m/min was achieved using only 1900W of laser power and 195A of current. This demonstrates that HWLAM can achieve higher deposition rates with lower overall energy consumption compared to WLAM.

By connecting the good points, a safe operating window was established for all  $V_f$  values, with one example shown in Figure 33. The safe zone was widest when  $V_f$  was 2 m/min, as the required current at this wire feeding speed is lower than at other speeds. Consequently, new parameter recipes were chosen within this safe window to investigate the influence of process parameters. The results of all tested points along with their corresponding process parameters are presented in Figure 57 (Appendix A).

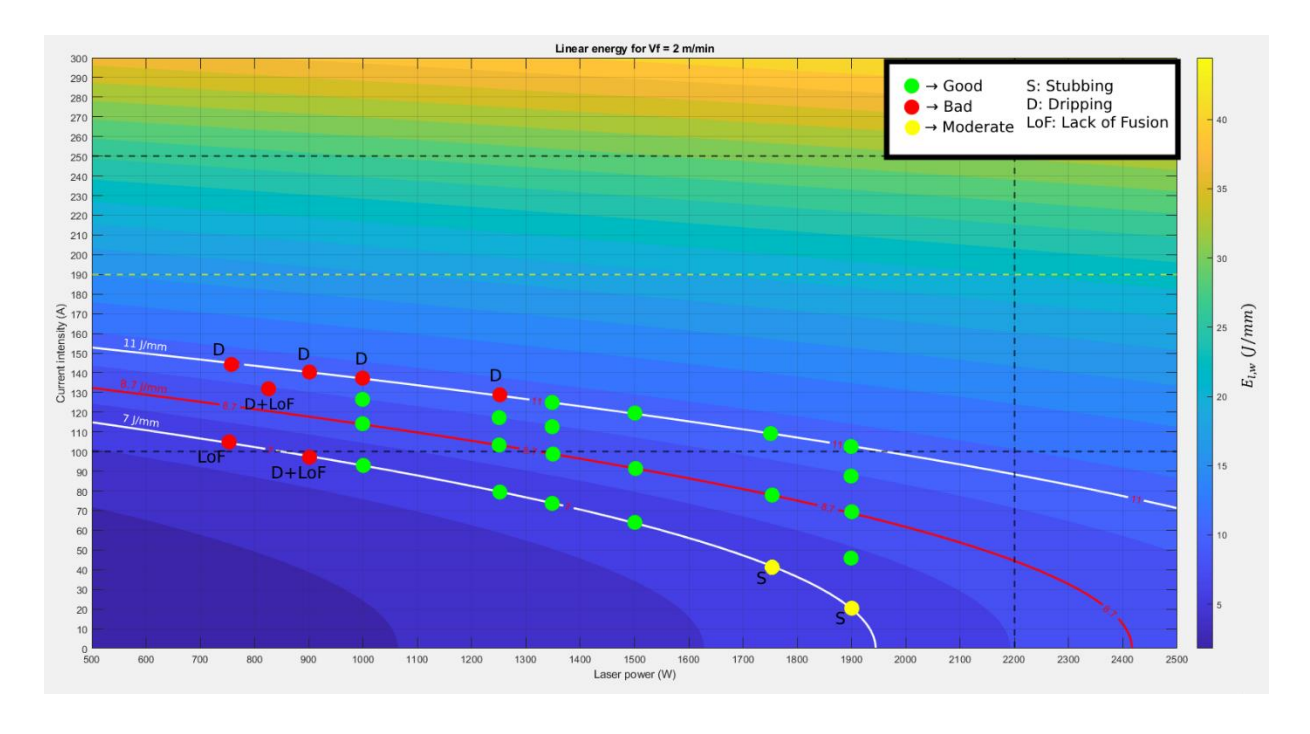


**Figure 29:** Fine approach process mapping test results when  $V_f$  = 2 m/min and k= 2.

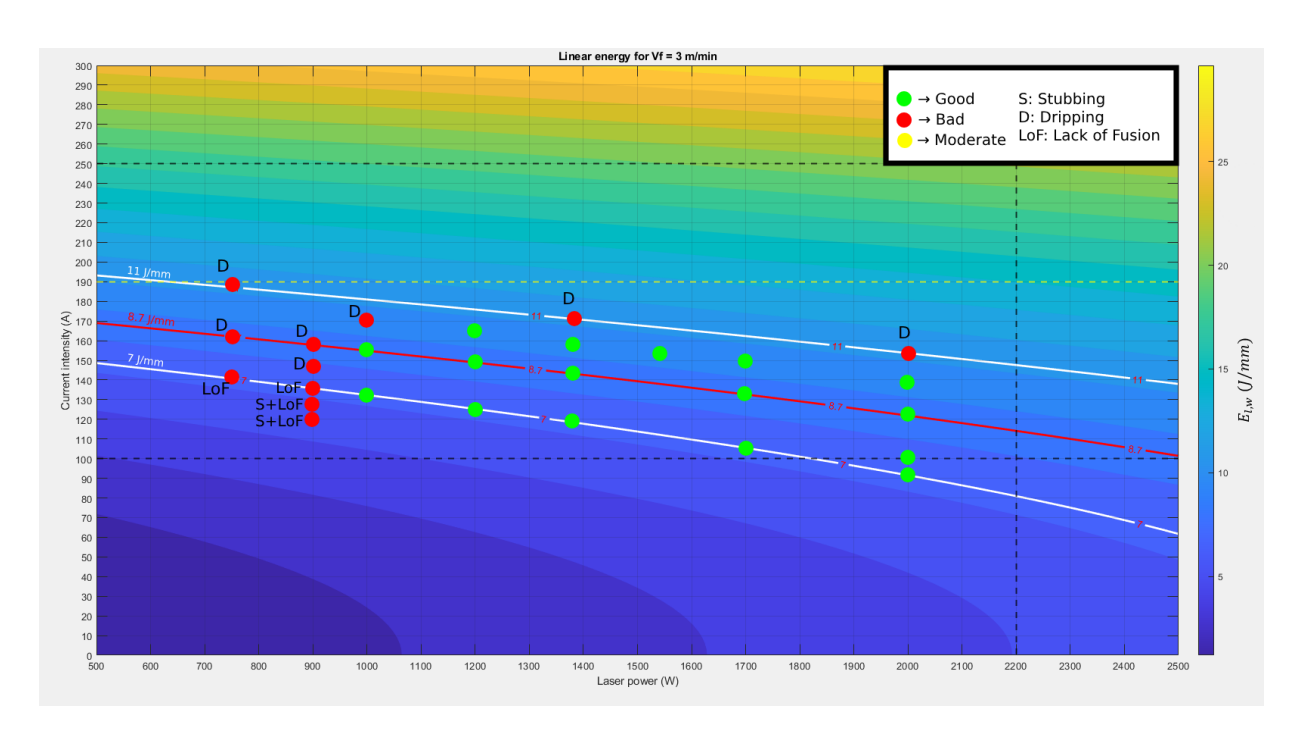


**Figure 30:** Fine approach process mapping test results when  $V_f$ =3 m/min and k=2.

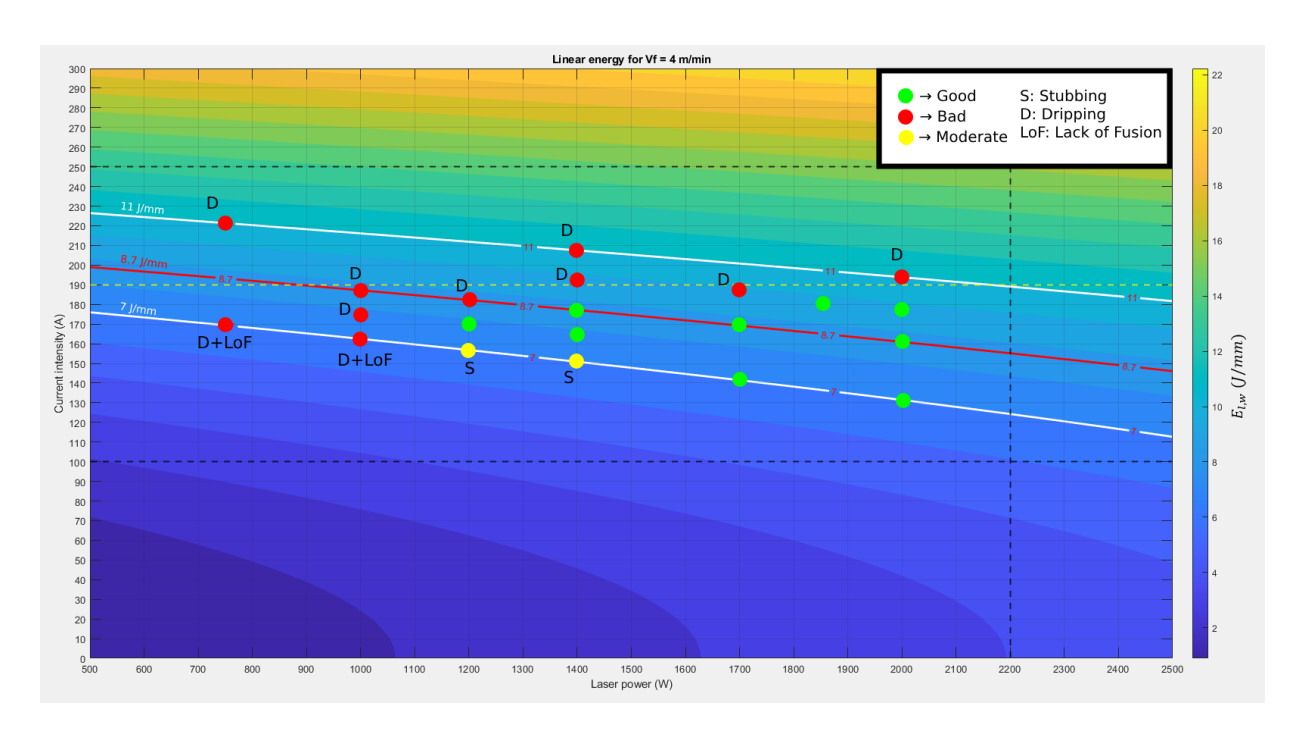


**Figure 31:** Fine approach process mapping test results when  $V_f$ =4 m/min and k=2.

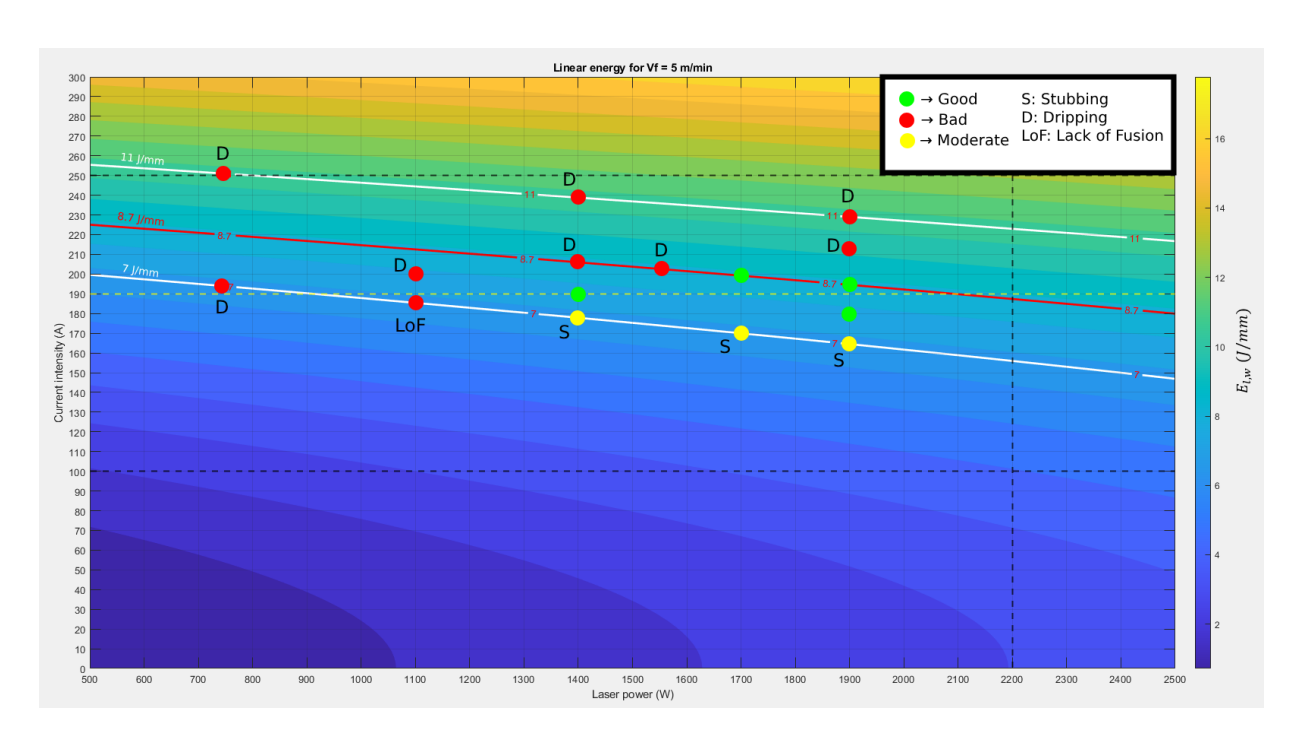


**Figure 32:** Fine approach process mapping test results when  $V_f$ =5 m/min and k=2.

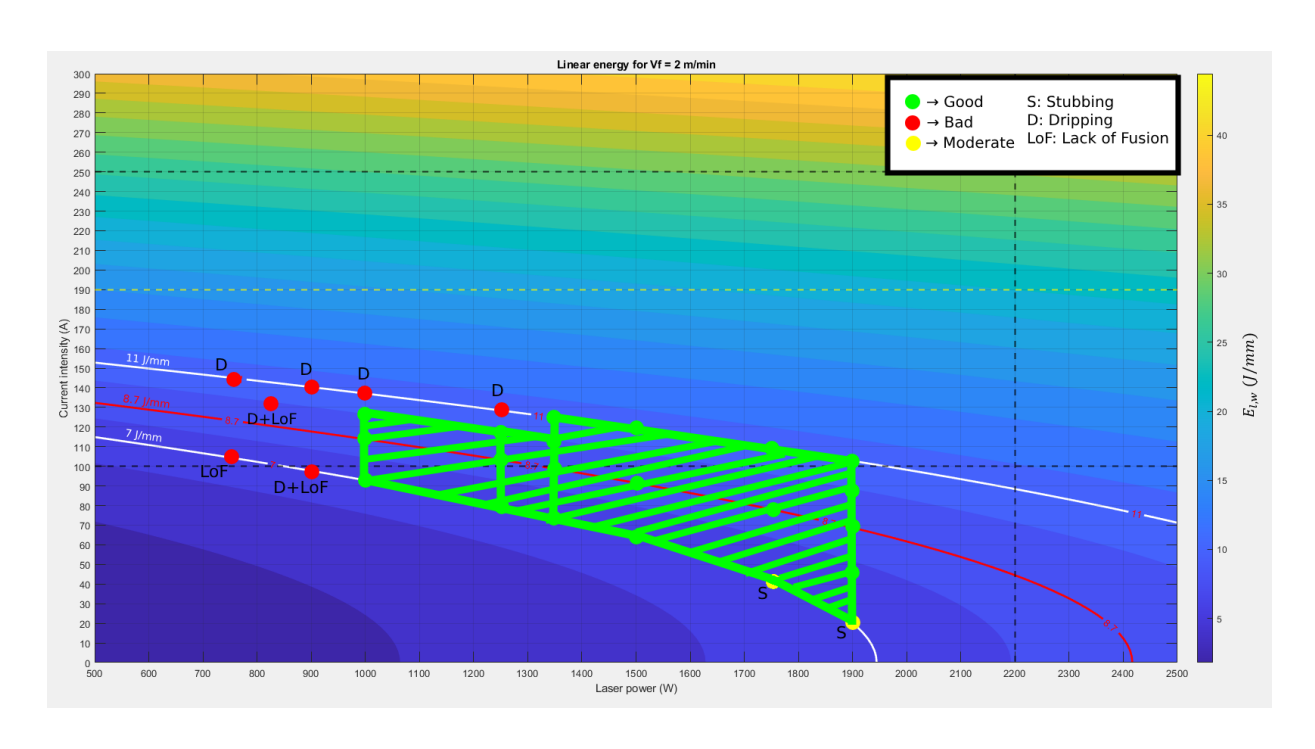


**Figure 33:** Safe manufacturing zone when  $V_f$  = 2 m/min and k=2.

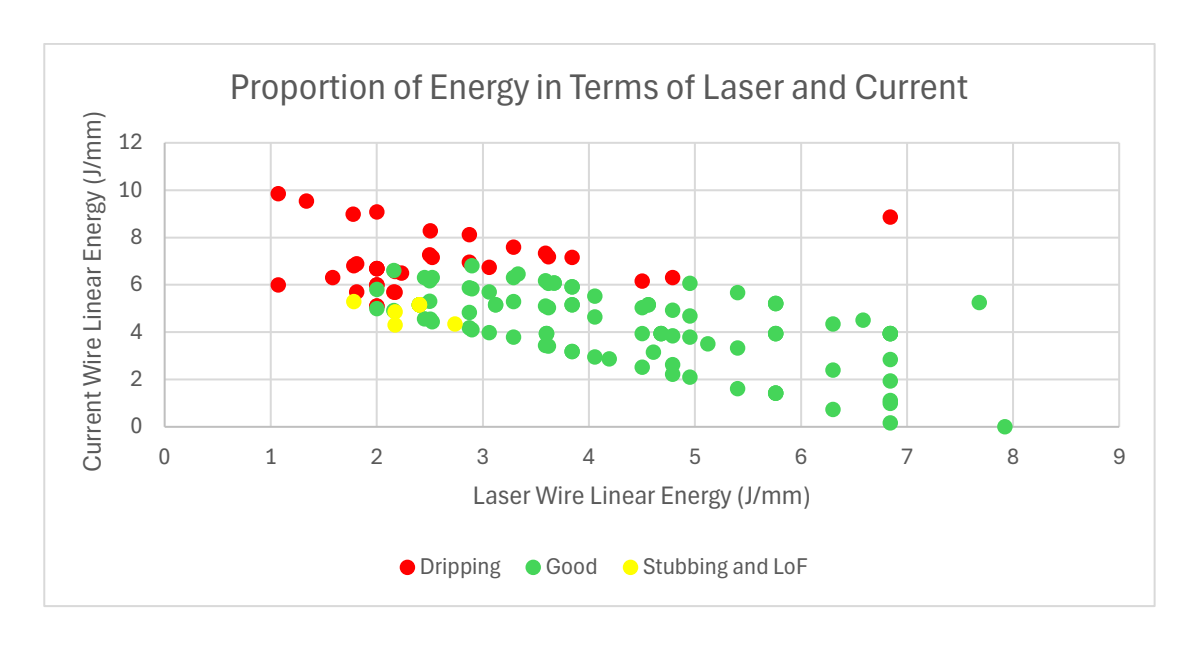


**Figure 34:** The distribution of laser and current wire linear energy values. Green dots represent good productions, red dots represent productions where dripping is observed, and yellow dots represent productions where lack of fusion and stubbing are observed.

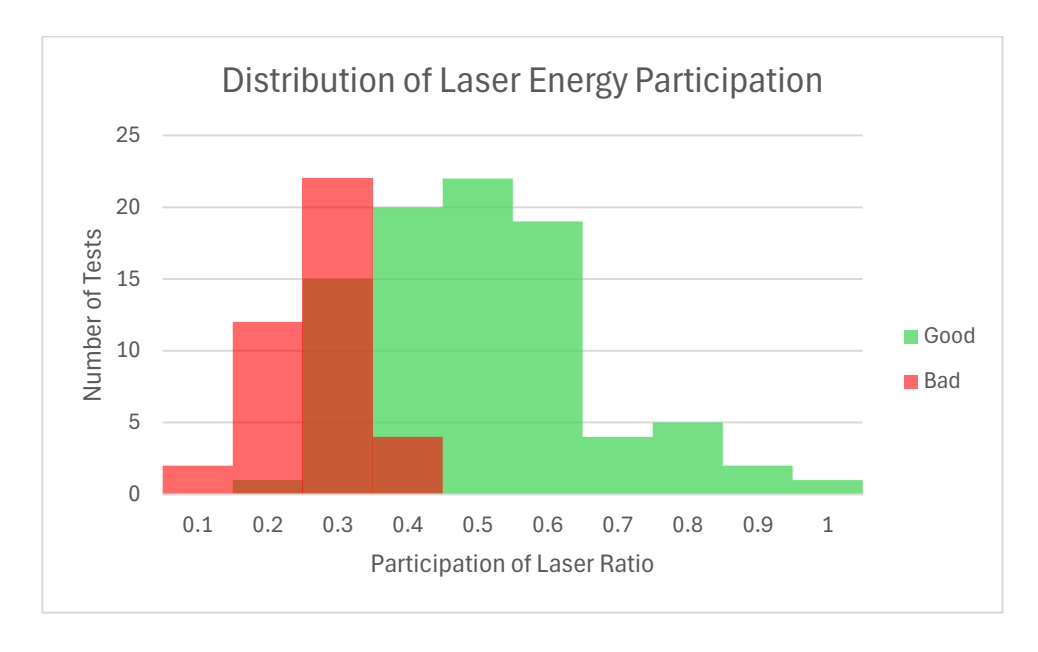


**Figure 35:** Distribution of laser energy participation into the system. Participation of laser represents the ratio of laser wire linear energy (J/mm) to the total wire linear energy (J/mm).

## 3.2. Bead Geometry Results

Based on experimental measurements of good beads (85 recipes in total), an empirical correlation was developed to relate the bead geometry to the process parameters. The bead height and bead width were expressed using a power-law form. The power-law model coefficients were obtained by applying linear regression on the natural logarithm of the experimental data. The resulting correlations enable prediction of bead geometry for a given set of process parameters, thereby facilitating process optimization and control.

$$W(mm) = 0.506 \cdot V_s^{-0.172} \cdot V_f^{0.046} \cdot P_l^{0.197} \cdot I^{0.065}$$
3.1

$$H(mm) = 2.466 \cdot V_s^{-0.737} \cdot V_f^{0.78} \cdot P_l^{-0.162} \cdot I^{-0.044}$$
3.2

The power-law model predicts bead geometry with a mean error of 2.2% and a maximum error of 8.5% (Figure 58), demonstrating strong correlation and predictive reliability for process parameter effects HWLAM.

## 3.2.1. Laser Power and Scanning Speed

Figure 36 and Figure 37 show the effects of laser power and scanning speed on bead geometry. Increase in laser power increases the bead width but decreases the height. This means that higher laser power expanded the melt pool laterally, causing the bead to spread out and become wider. Since the wire feeding speed is constant, the volume of wire which is fed into the melt pool does not change, resulting in a wider but flatter bead. When the scanning speed increases, both the width and height of the bead decrease. This is because at higher scanning speeds, less wire volume is fed, and the laser spends less time at each point on the substrate surface. The obtained results showed the same trend as in previous HWLAM / WLAM studies (Table 2).

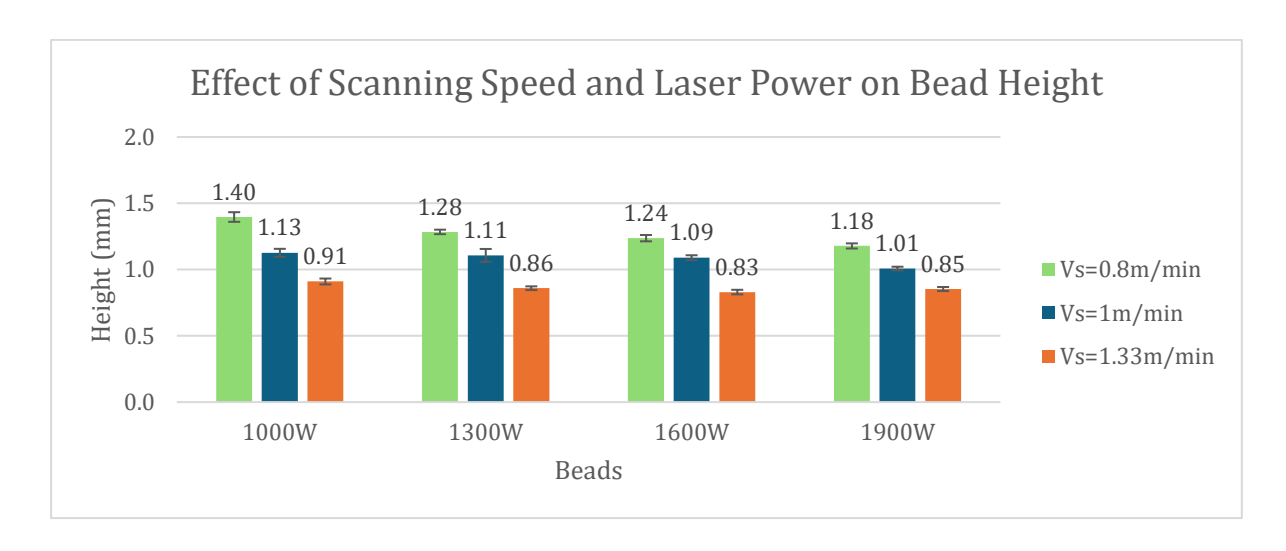


**Figure 36:** Effects of laser power and scanning speed on bead height with varying  $P_l$  and  $V_s$ , while the other parameters were kept constant:  $V_f$ =2m/min and I=100A.

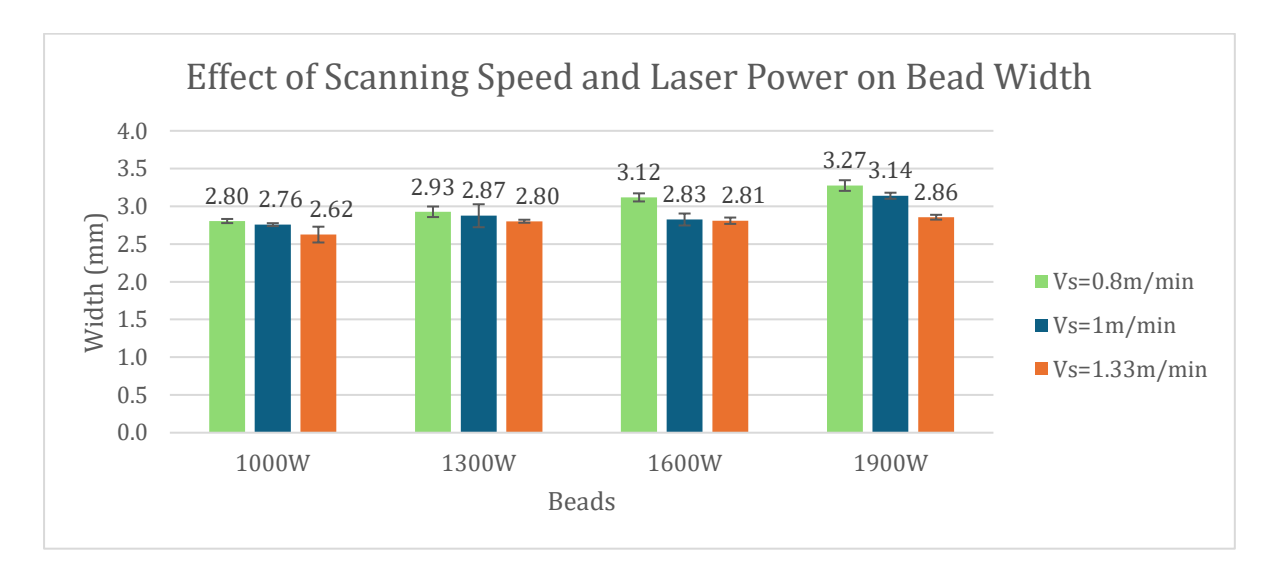


**Figure 37:** Effects of laser power and scanning speed on bead width with varying  $P_l$  and  $V_s$ , while the other parameters were kept constant:  $V_f$ =2m/min and I=100A.

## 3.2.2. Wire Feeding Speed

Different wire feeding speed values were tested while keeping the other process parameters constant. The results are shown in Figure 38 and Figure 39. It is observed that as the wire feeding speed increases, the bead height also increases; this is due to more wire being transferred into the melt pool. However, it is observed that the bead width remains largely constant, showing only a minimal decrease, as the wire feeding speed increases. This may suggest that the chosen laser power was not sufficient to fully melt and spread the additional wire material laterally. As a result, the extra material accumulates vertically, causing an increase

in bead height rather than bead width. Previous studies in literature have reported two distinct trends regarding the effect of wire feeding speed on bead width (Table 2). The results obtained in this study align with those reports that observed changes in bead height but not in bead width with variations in wire feeding speed [57], [59].

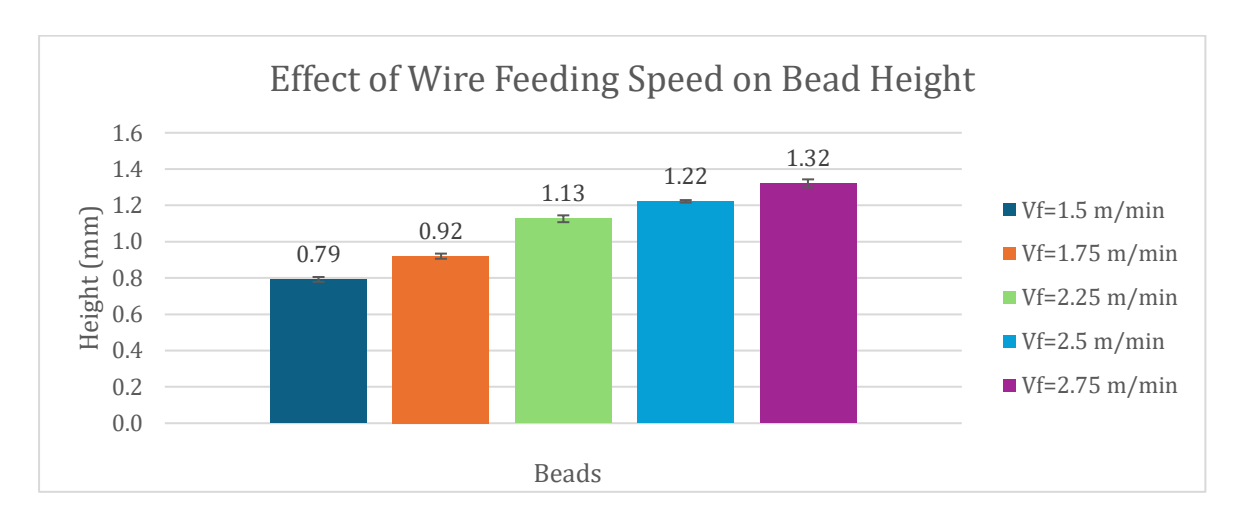


**Figure 38:** Effect of wire feeding speed on bead height with varying  $V_f$ , while the other parameters were kept constant:  $P_l$ =1600W,  $V_s$ =1m/min and I=100A.

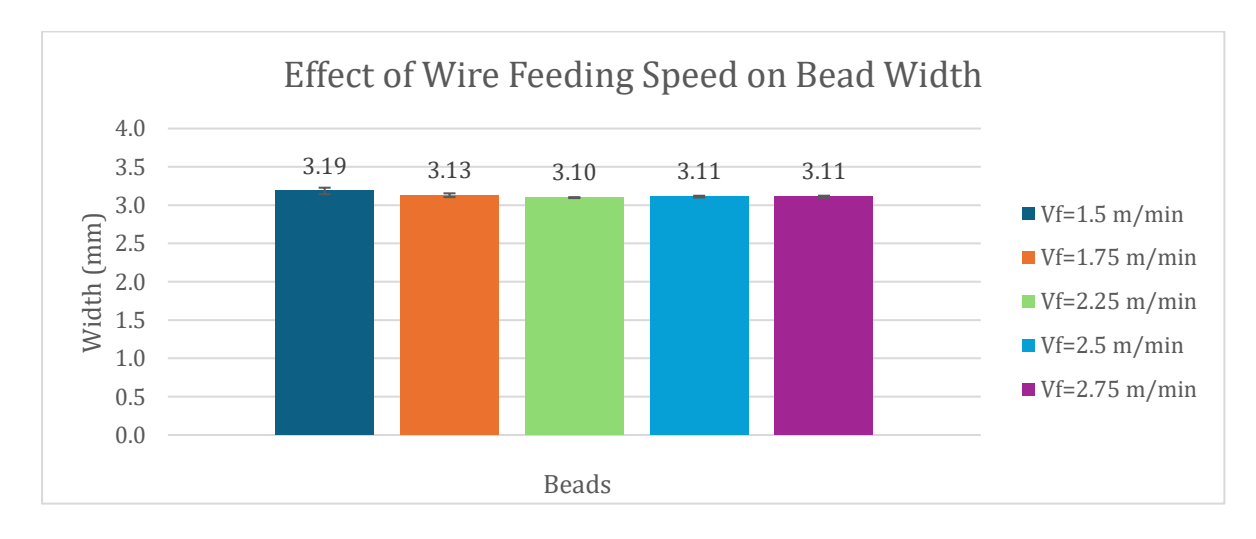


**Figure 39:** Effect of wire feeding speed on bead width with varying  $V_f$ , while the other parameters were kept constant:  $P_l$ =1600W,  $V_s$ =1m/min and I=100A.

#### **3.2.3. Current**

The effect of current and scanning speed is shown in Figure 40 and Figure 41. Here, the main focus is current, since the effect of scanning speed was already discussed in Section 3.2.1. When the current is increased from 60 A to 115 A while keeping the other parameters constant, both the height and width of the beads remain the same, with only small variations observed. This is likely because the laser power dominates melt-pool formation and geometric control. The

current only provides heat to the wire and the additional heat that may contribute to the melt pool is small compared to the laser input (Figure 35). The results are also in correspondence with findings of Kisielewicz et al. [52]. They found that current had limited to no impact on bead width and height, while laser power had considerable effect on bead geometry.

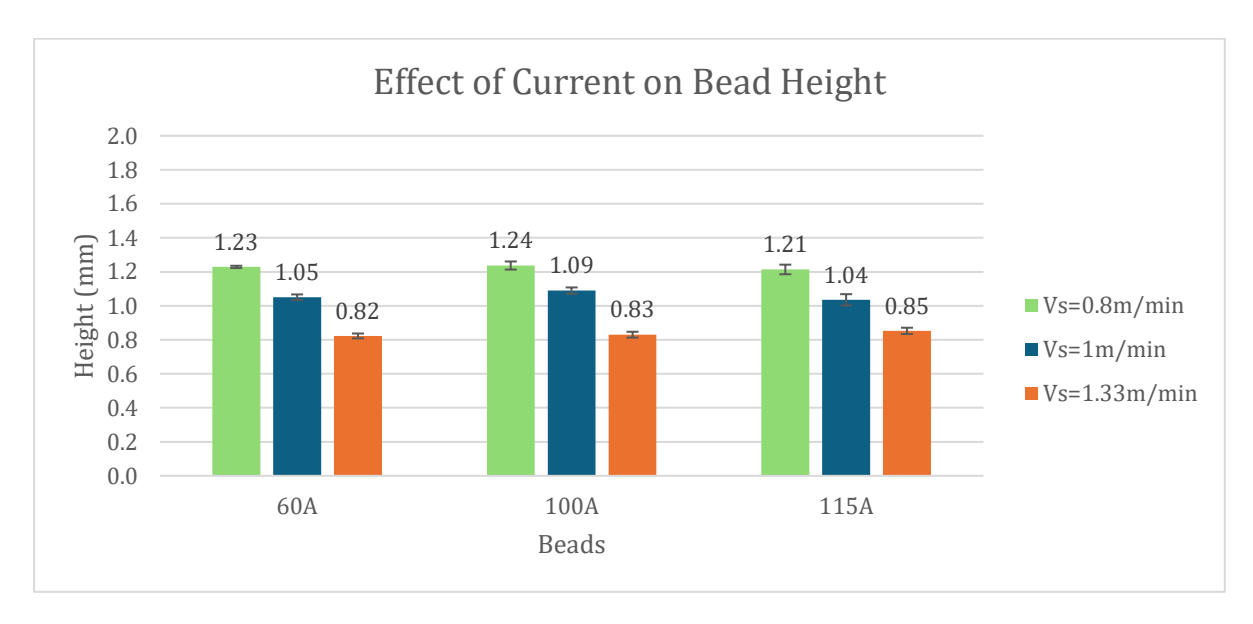


**Figure 40:** Effects of current on bead height with varying I and  $V_s$ , while the other parameters were kept constant:  $P_l$ =1600 and  $V_f$ =2m/min.

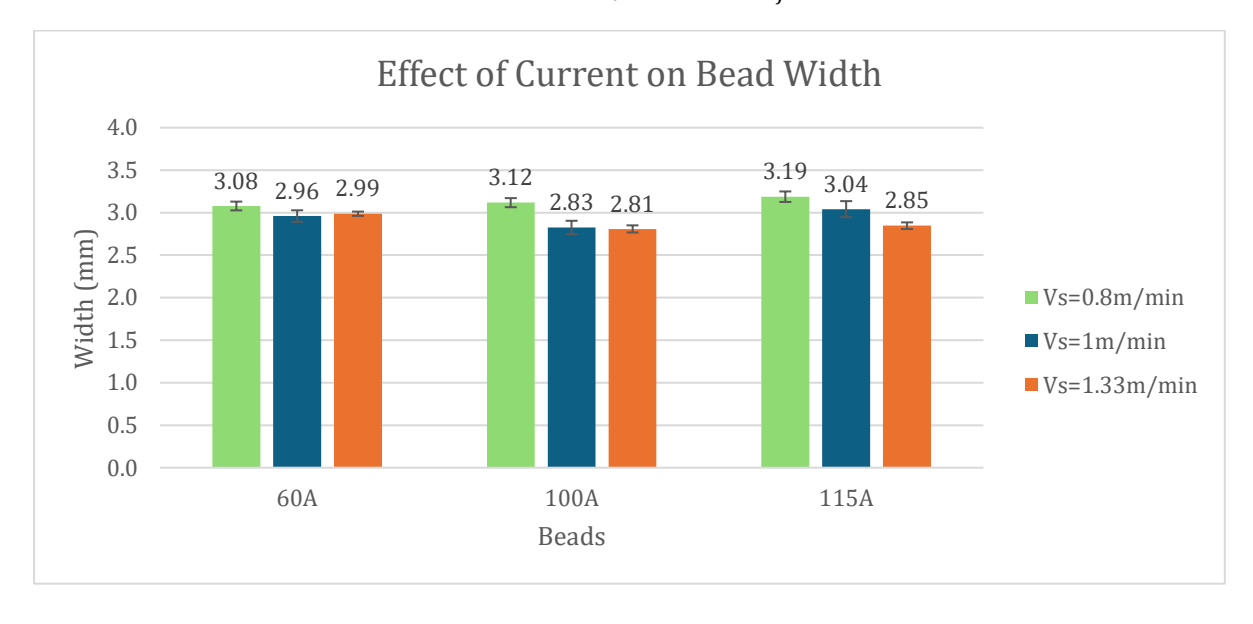


**Figure 41:** Effects of current on bead width with varying I and  $V_s$ , while the other parameters were kept constant:  $P_l$ =1600 and  $V_f$ =2m/min.

## 3.3. Surface Roughness Results

Surface profile results are presented below. Measurement uncertainties for each track are provided in Table 11 (Appendix C). Ra and Rz were used to represent the roughness measurements of the profile, while Wt, Wq, and Wsm were used to represent the waviness measurements. The Ra parameter provides the average deviation of the profile and is the most commonly used for roughness measurements. However, in all the tracks, the surface roughness along the profile was not constant during the measurements. Beginning of the track showed rougher profile, likely due to the time required for the process to stabilize (Figure 42 and Figure 43). For this reason, the Rz parameter was also used, as it provides a more sensitive representation of surface variations across multiple sampling lengths. Wq was used to provide a statistically robust measure of the average waviness amplitude, while Wt represents the total peak to valley height, indicating the extreme waviness. Wsm describes the spacing between waviness peaks, showing the periodicity of the surface waviness. Thus, with these three waviness parameters, the surface waviness can be fully characterized in terms of average amplitude, extreme height, and spacing.

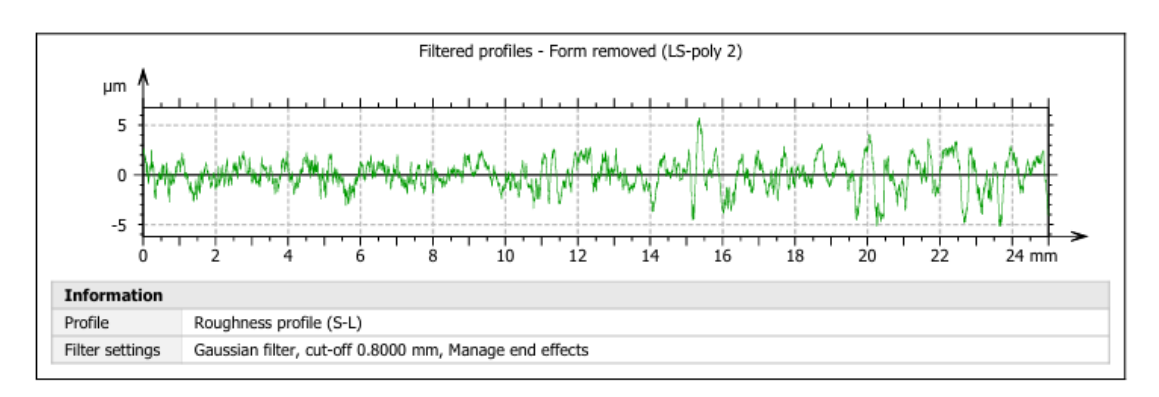


**Figure 42:** Roughness profile of track 104 where  $V_s = 1$  m/min,  $P_l = 1900$  W,  $V_f = 2$  m/min and I = 100A.

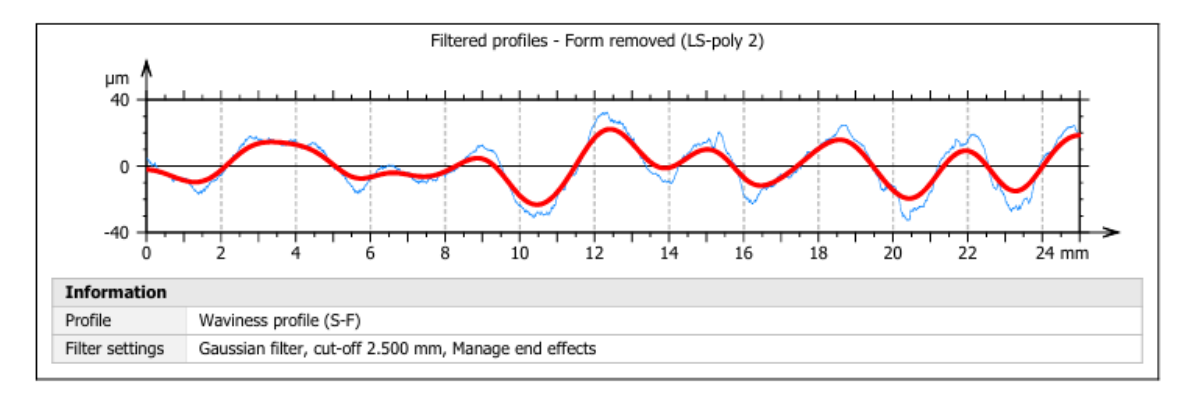


**Figure 43:** Waviness profile of track 104 where  $V_s = 1$  m/min,  $P_l = 1900$  W,  $V_f = 2$  m/min and I = 100A.

## 3.3.1. Laser Power and Scanning Speed

Table 8 presents the results of roughness and waviness for different  $V_s$  and  $P_l$  values. For clarity, tracks are grouped according to their  $V_s$  values, and the corresponding laser power values are shown in the adjacent column for ease of comparison. For all  $V_s$  groups, the roughness values decrease when the laser power increases from 1000 W to 1300 W, and then increases again, with the highest roughness value observed at 1900 W for each V<sub>s</sub> value. To understand the reason for this behavior, Alicona images of the tracks were examined. While porosity was observed on the surfaces of the tracks with low laser power, no porosity was observed on the surfaces of the tracks with high laser power (Figure 44) or with WLAM, where only high laser power was applied and no current was used. The reason for the high roughness values of the tracks with low laser power is the surface porosity. These porosities may occur because lower laser power results in less heating of the track, causing faster solidification that traps gases before they can escape. For the tracks with high laser power, the high roughness values may be due to the high energy creating an uncontrolled/unstable melt pool, resulting in surface some defects, rougher texture, spatters, etc. The highest waviness values were also observed in the tracks with high laser power, which again supports the idea of an uncontrolled and unstable melt pool. Similarly, tracks with lower  $V_s$  exhibited higher roughness and waviness, consistent with the same reasoning about energy input and melt pool dynamics. At high laser powers, excessive energy input can lead to melt pool oscillations and rapid surface evaporation, which further destabilize the molten pool and contribute to rougher textures, spatters, and increased surface waviness. This phenomenon has also been reported in previous studies [62], [77], [78], where high laser power caused surface ripples and splatters that increased the surface roughness and waviness.

**Table 8:** Roughness and waviness values of different tracks with varying laser power and scanning speed, where  $V_f$ =2m/min and I=100A.

	Trac	ck Number	$P_l(W)$	Ra (µm)	Rz (μm)	Wt (µm)	Wq (µm)	Wsm (mm)
		113	1000	1.48	7.66	23.99	5.60	5.12
9.0	nin	114	1300	1.33	6.62	26.85	6.00	5.35
Vs=0.8	m/min	115	1600	1.21	6.06	32.37	7.50	7.50
		116	1900	1.70	7.96	59.21	13.64	6.79
		101	1000	1.49	7.61	29.49	7.38	8.59
<del></del>	Vs=1 m/min	102	1300	1.25	6.44	31.34	7.39	6.89
VS=		103	1600	1.37	6.62	31.68	7.44	7.62
		104	1900	1.39	6.57	43.51	9.74	5.21
		107	1000	1.29	6.41	26.07	5.60	4.84
1.33	nin	108	1300	1.14	5.74	24.10	4.91	5.60
Vs=1.33	m/min	109	1600	1.37	6.43	21.81	4.99	5.39
		110	1900	1.70	7.61	37.24	8.53	6.67

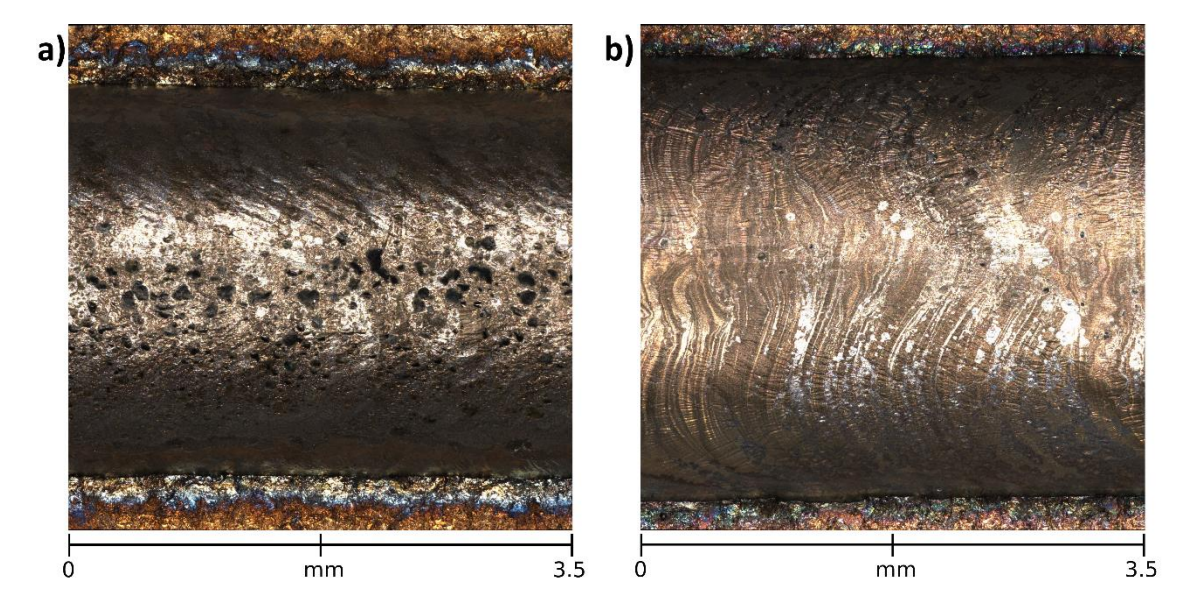


**Figure 44:** Alicona images of two different tracks with the following varying parameters: a)  $V_s = 0.8$  m/min,  $P_l = 1000$  W and b)  $V_s = 0.8$  m/min,  $P_l = 1900$  W. The remaining parameters were kept constant:  $V_f = 2$  m/min and I = 100A.

## 3.3.2. Wire Feeding Speed

The results of roughness and waviness for different wire feeding speed values are presented in Table 9. Both roughness and waviness values increase with an increase in  $V_f$ . As  $V_f$  increases, the wire linear energy decreases. The increase in roughness and waviness may be caused by some small stubbing or faster wire addition may disturb the melt pool dynamics. Although no visible stubbings were observed during production, some small vibrations might cause irregularities on the surface.

**Table 9:** Roughness and waviness values of different tracks with varying wire feeding speed, where  $V_s$ =1m/min, I=100A and  $P_I$ =1600W.

Track Number	$V_f$ ( $m/min$ )	Ra (µm)	Rz (µm)	Wt (µm)	Wq (µm)	Wsm (mm)
137	1.5	1.17	6.01	28.34	6.96	5.90
138	1.75	1.25	6.17	28.87	6.53	6.74
139	2.25	1.35	6.40	31.86	6.92	5.40
135	2.5	1.63	7.74	30.80	7.46	5.61
136	2.75	1.61	7.30	34.40	7.94	6.83

#### **3.3.3. Current**

The results of roughness and waviness for different current values are presented in Table 10. Both waviness and roughness values tend to decrease when the current increases. Increasing the current increase the wire temperature before it enters the melt pool, resulting in the wire melting faster and more smoothly when it reaches the melt pool. This may improve the melt pool stability. A higher wire temperature reduces the thermal gradient between the wire and melt pool, and this may result in more uniform melting and fluid flow.

Although no study has directly reported the effect of current on surface roughness in the HWLAM process, Sang et al. [79] found that surface roughness (Ra) decreased 30% when the wire is heated compared to the cold version. This indicates that the introduction of joule heating can lead to smoother depositions.

**Table 10:** Roughness and waviness values of different tracks with varying current, where  $V_S=1$ m/min,  $V_f=2$ m/min and  $P_l=1600$ W.

Track Number	I(A)	Ra (µm)	Rz (μm)	Wt (µm)	Wq (µm)	Wsm (mm)
105	60	1.52	7.42	32.23	7.21	6.52
103	100	1.37	6.62	31.68	7.44	7.62
106	115	1.31	6.44	30.74	6.84	6.07

## 3.4. Dilution and Contact Angle Results

## 3.4.1. Laser Power and Scanning Speed

When the laser power increases, the penetration area also increases (Figure 45). Conversely, higher  $V_s$  values result in lower penetration depth, since the time the laser stays on a specific point of the surface is shorter. However, in the case of dilution and contact angle calculations, the situation is not this straightforward. When the laser power increases, the dilution also increases (Figure 46). This is because the penetration area increases, and since the wire feeding speed was kept constant, the volume of wire fed into the melt pool remains the same. For  $V_s$ , the situation is somewhat different.  $V_s$  directly affects both the time that laser stays on a certain point of the substrate and the volume of wire fed to that point. Therefore, no clear trend could be identified. When the laser power is low (1000 W), the dominant factor that determines dilution may be the wire feeding volume, and therefore the bead area. When the laser power is high (1900 W), the dominant factor that determines dilution may be the laser power, and therefore the penetration area. This idea is supported by the fact that, at low laser power, the dilution results with varying  $V_s$  values follow the same trend as the wire feeding speed (Figure 49). The obtained results are consistent with previous HWLAM/WLAM studies (Table 3).

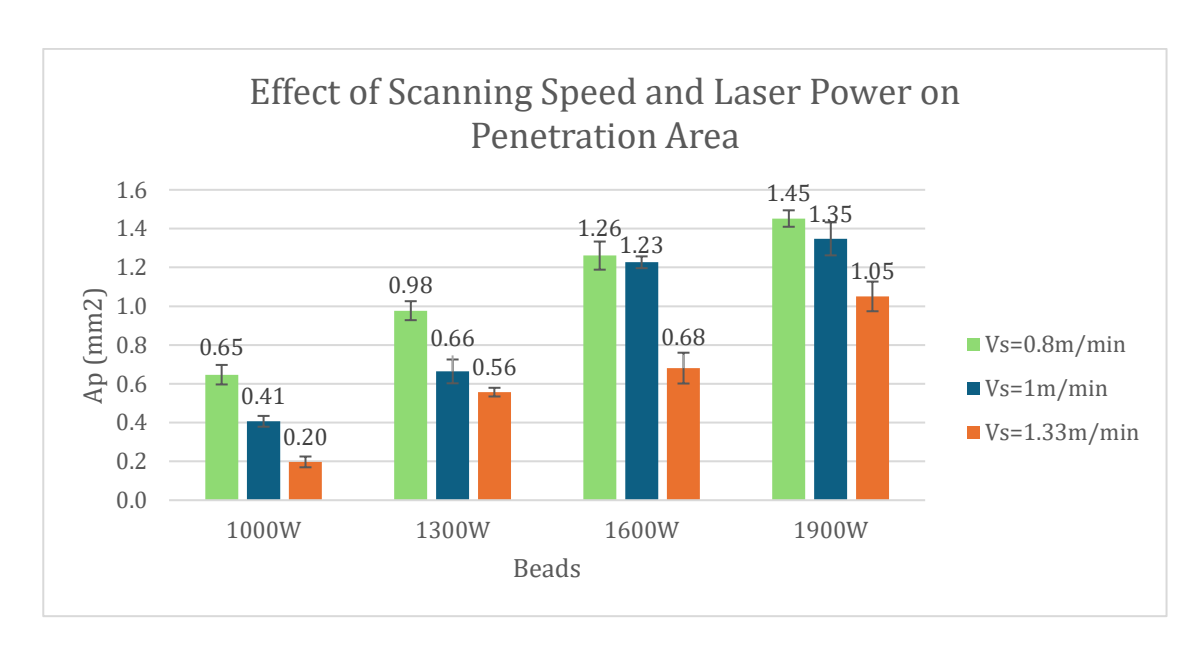


**Figure 45:** Effects of laser power and scanning speed on penetration area with varying  $P_l$  and  $V_s$ , while the other parameters were kept constant:  $V_f$ =1m/min and I=100A.

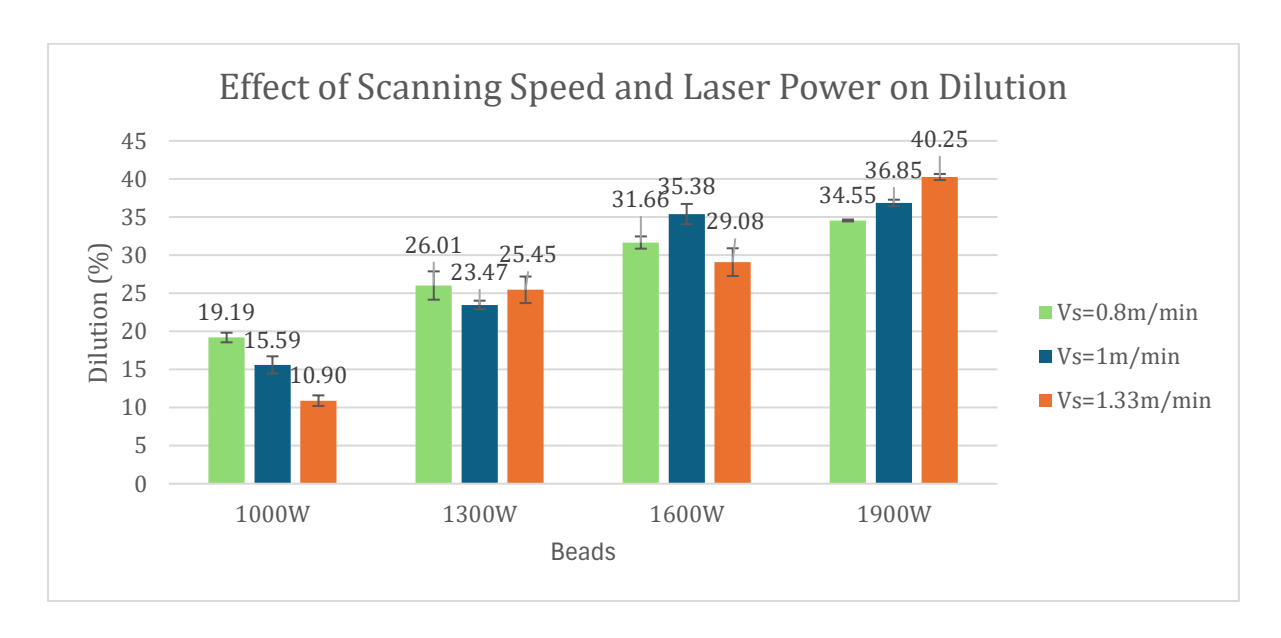


**Figure 46:** Effects of laser power and scanning speed on dilution with varying  $P_l$  and  $V_s$ , while the other parameters were kept constant:  $V_f$ =1m/min and I=100A.

Effects of laser power and scanning speed on contact angle is shown in Figure 47. At low  $V_s$  values, the contact angle values are higher. This is most likely due, as previously discussed, to the robot head staying longer at a specific point on the substrate, resulting in more material being fed. When the laser power is increased, however, the contact angle decreases, indicating that the wire flattens on the surface due to more melting.

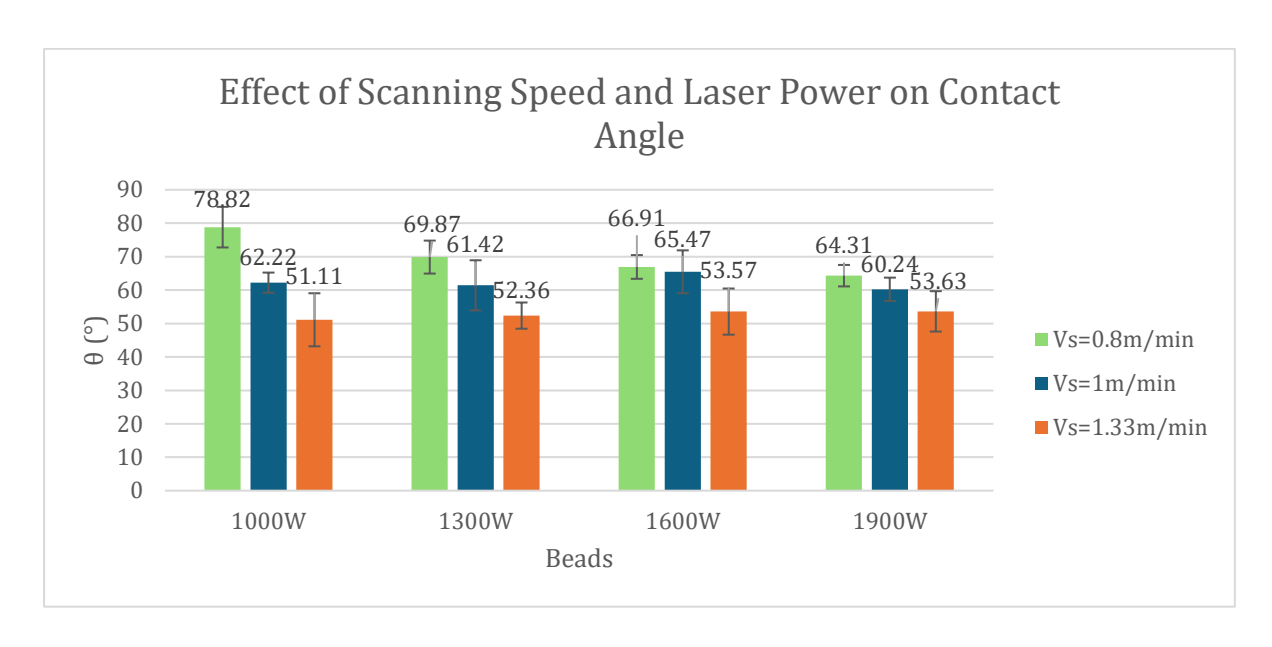


**Figure 47:** Effects of laser power and scanning speed on contact angle with varying  $P_l$  and  $V_s$ , while the other parameters were kept constant:  $V_f$ =1m/min and I=100A.

## 3.4.2. Wire Feeding Speed

Since the total energy supplied to the system remains the same, increasing the wire feed speed results in more wire entering the melt pool being relatively cooler than at lower feeding speeds. This is because, at lower wire feed speeds, each portion of the wire is exposed to the laser for a longer time and absorbs more heat, resulting in a hotter melt pool with greater penetration depth and area. At higher wire feed speeds, the wire is exposed to the laser for a shorter time, absorbs less heat, and produces a less deep melt pool (Figure 48). Since the bead area was also smaller at lower wire feed speeds (Figure 38 and Figure 39), combination of these two resulted in a higher dilution percentage (Figure 49). Feeding more wire with the same energy leads to higher contact angle values and caused the beads to take on a more balloon-like shape (Figure 50). These results are consistent with previously reported HWLAM/WLAM studies (Table 3).

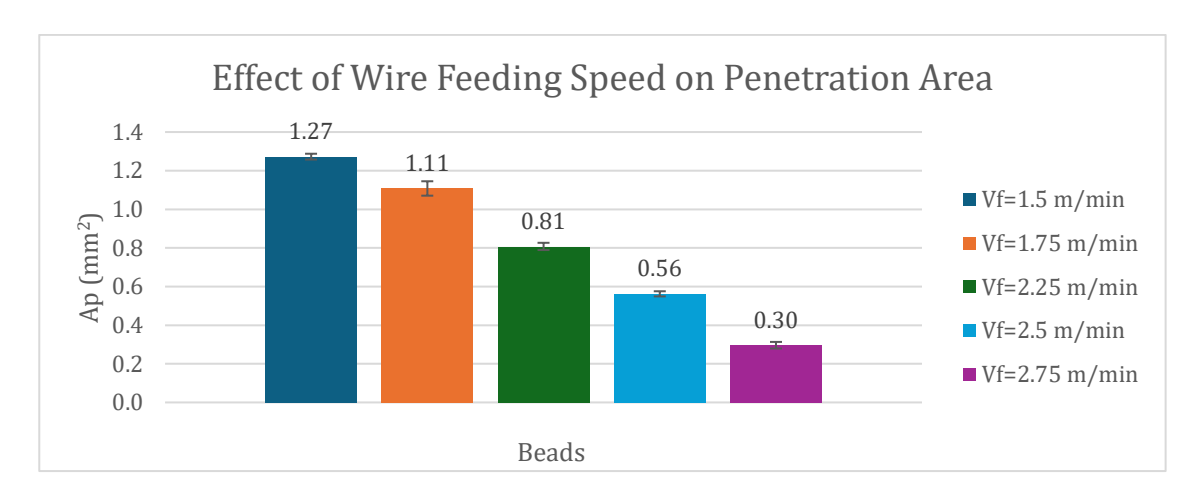


**Figure 48:** Effect of wire feeding speed on penetration area with varying  $V_f$ , while the other parameters were kept constant:  $P_l$ =1600W,  $V_s$ =1m/min and I=100A.

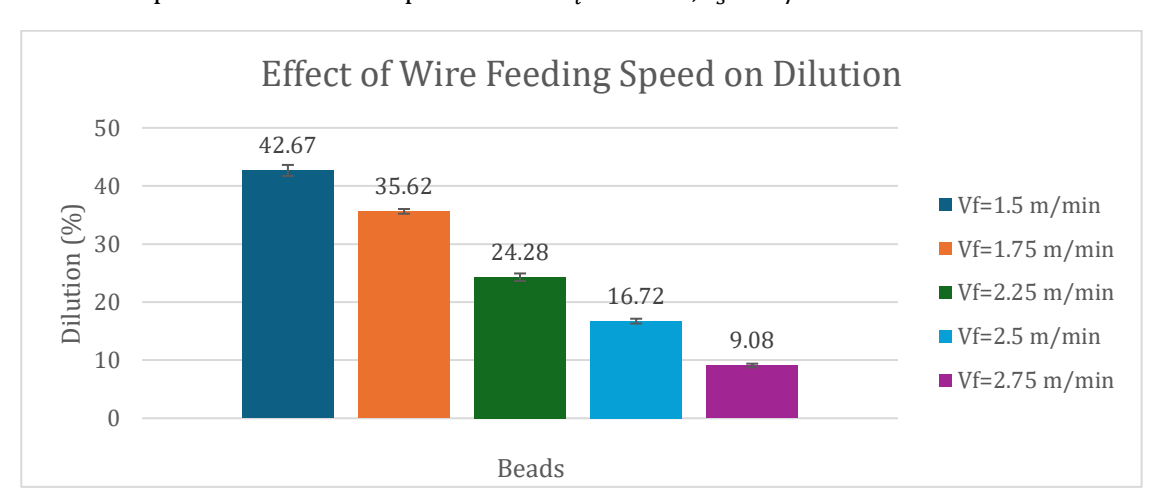


**Figure 49:** Effect of wire feeding speed on dilution with varying  $V_f$ , while the other parameters were kept constant:  $P_l$ =1600W,  $V_s$ =1m/min and I=100A.

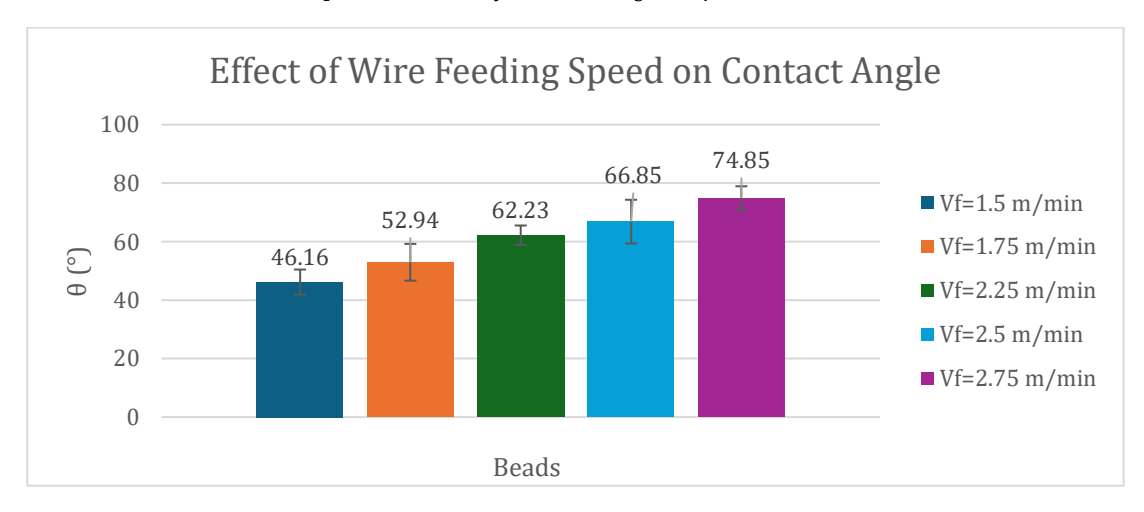
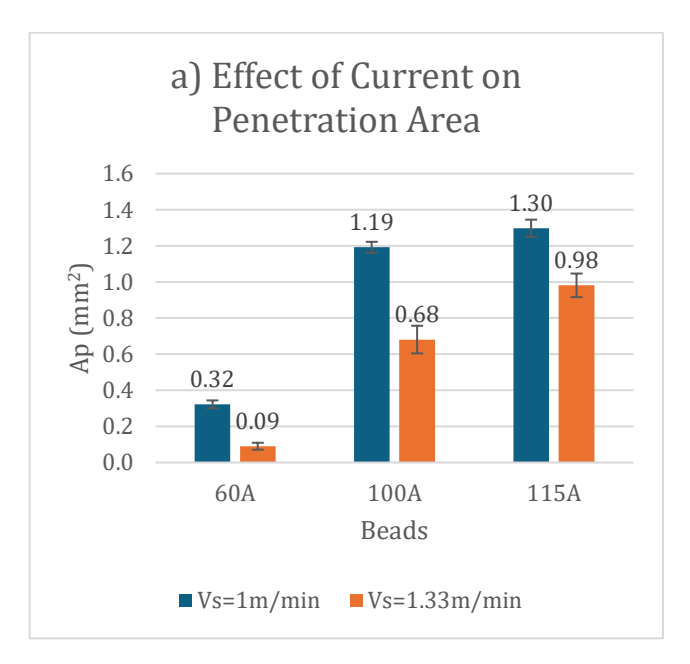


**Figure 50:** Effect of wire feeding speed on contact angle with varying  $V_f$ , while the other parameters were kept constant:  $P_l$ =1600W,  $V_s$ =1m/min and I=100A.

#### **3.4.3. Current**

Figure 51 shows the effect of current on penetration area and dilution. When the current increases, the penetration area and dilution increase. The increase in penetration area at higher currents occurs because the wire is heated more, creating a hotter melt pool that leads to greater penetration depth and area. Since current has almost no effect on bead area (Section 3.2.3), the increase in penetration area results in increased dilution. Since current almost has no effect on bead height and width, the contact angle is expected to not be affected by current. No obvious trend is observed in the contact angle with changes in current (Figure 52). Some fluctuations are seen, but these might be due to the manufacturing process.

The results shown in Figure 51 are consistent with those of Kisielewicz et al. [52], who also reported that increasing the heating voltage leads to greater dilution and penetration. They reported a significant increase in dilution and penetration area when current heating was introduced to the cold wire process. However, beyond a certain voltage, further increases resulted in only minor improvements. In other words, the trend showed a sharp initial rise followed by a more gradual increase.



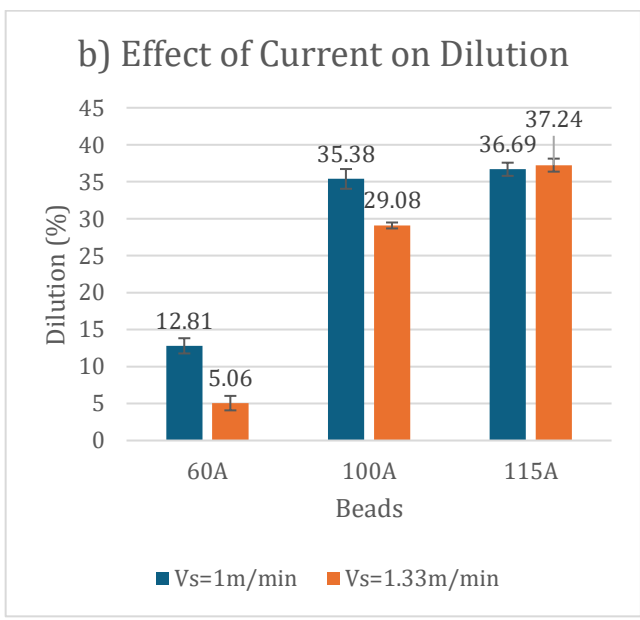


**Figure 51:** Effects of current on a) penetration area and b) dilution with varying I and  $V_s$ , while the other parameters were kept constant:  $P_l$ =1600W and  $V_f$ =2m/min.

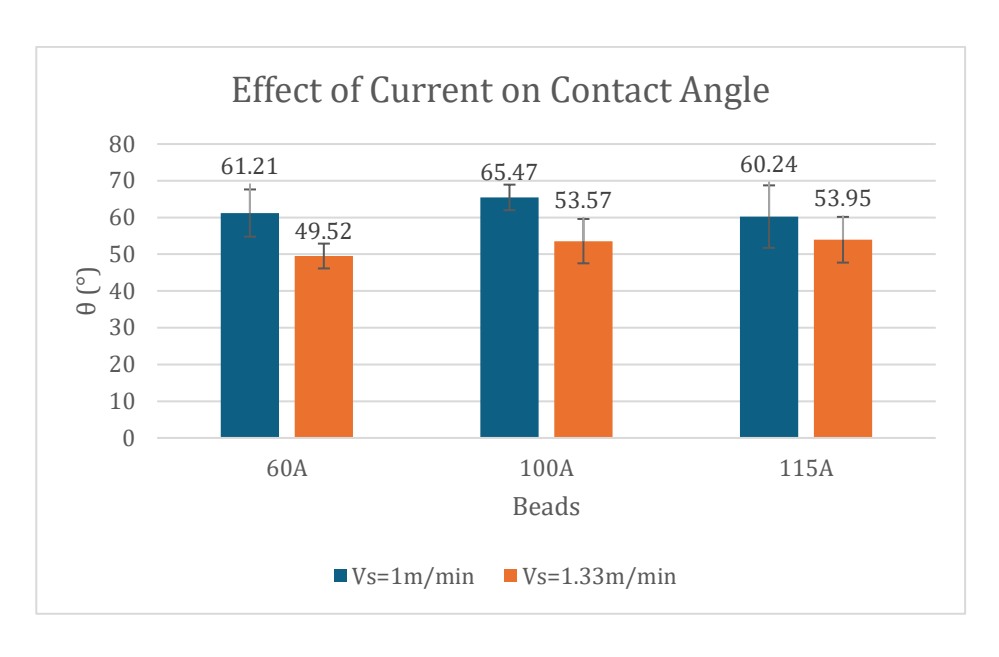


**Figure 52:** Effects of current on contact angle with varying *I* and  $V_s$ , while the other parameters were kept constant:  $P_l$ =1600W and  $V_f$ =2m/min.

### 3.5. Microstructure Results

Inner porosity was also examined for the beads tested for dilution in Section 3.4, and no inner porosity is observed in any of them. An example of optical microscope image is shown in Figure 53, where the observation plane corresponds to the Z–Y plane (build direction). The orientation of the grains is perpendicular to the remelted zone line and directed toward the top of the bead. This corresponds to the direction of the temperature gradient during solidification. Generally, beads show columnar dendritic microstructure. Higher energy or linear energy input into the system results in coarser columnar grains, while lower input leads to finer columnar grains or the absence of columnar grains, (Figure 54 and Figure 55). In Figure 54, sample (a) exhibits finer columnar dendrites due to lower heat input, indicating a higher cooling rate and stronger thermal gradient during solidification. In contrast, sample (b) exhibited coarser and more elongated dendrites due to the greater heat input and slower cooling. This demonstrates how increasing laser power or heat input promotes coarser solidification structures.

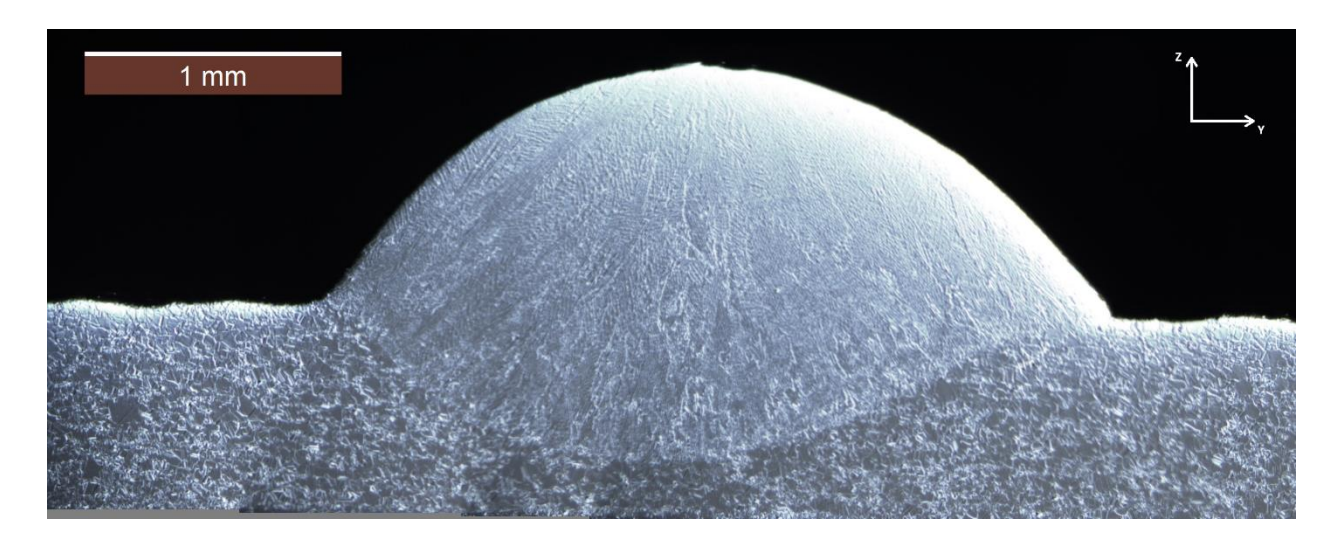


**Figure 53:** Optical microscope image of Bead 138 where  $V_s$ =1m/min,  $V_f$ =1.75m/min, I=100A and  $P_I$ =1600W.

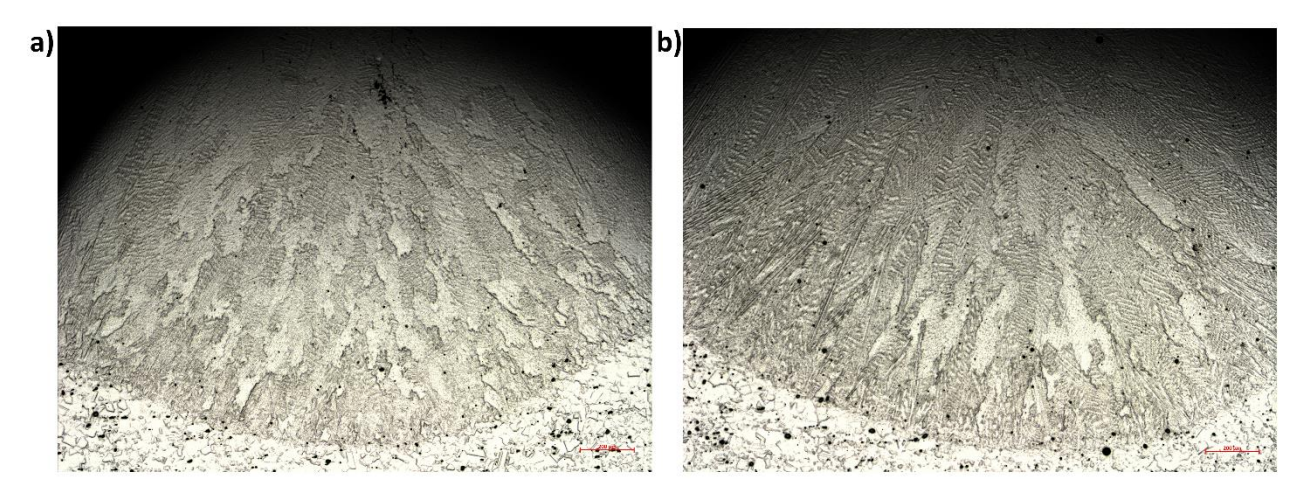


**Figure 54:** Optical microscope images of beads with a)  $P_l$ =1000W and b)  $P_l$ =1900W, with all other parameters kept constant:  $V_s$ =0.8m/min,  $V_f$ =2m/min, I=100A.

In Figure 55, the lower regions with equiaxed grains correspond to the substrate, while the upper regions are deposited bead with a distinct separation of diffusion line. Sample (a) clearly showed more columnar grains growing in the build direction, whereas sample (b) had much less elongated columnar structure. The calculated wire linear energy is 12.93 J/mm for sample (a) and 10.97 J/mm for sample (b), indicating a higher energy input per unit length of wire in sample (a). This difference in total energy input directly influences the solidification rates thus the microstructure as shown.

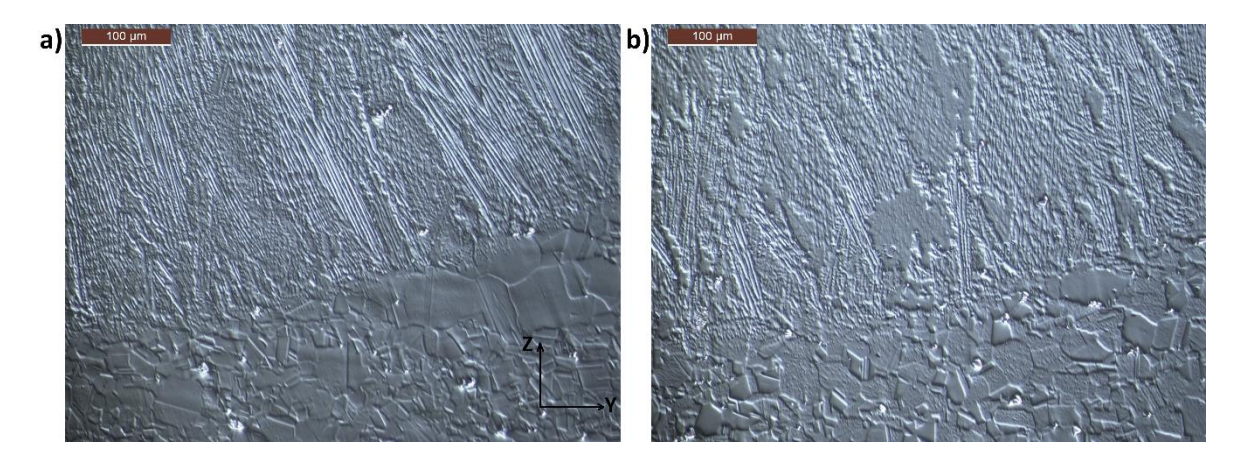


**Figure 55:** Optical microscope images of beads with a)  $P_l$ =1600W,  $V_s$ =1m/min,  $V_f$ =1.5m/min, I=100A and  $E_{l,w}$ = 12.93 J/mm and b)  $P_l$ =1600W,  $V_s$ =1m/min,  $V_f$ =2m/min, I=115A and  $E_{l,w}$ = 10.97 J/mm.

The proportion of the energy sources has a significant impact on microstructure, even when the total wire linear energy is kept the same. In Figure 56, bead (a) was deposited using only laser power of 2200W, whereas bead (b) was produced with a laser power of 1000 W and an additional current of 105 A. Although the total wire linear energy in both cases is 7.9 J/mm, the microstructures are notably different. In bead (a), the grains are elongated, columnar, and oriented upward from the fusion line toward the bead surface. This columnar structure is characteristic of high thermal gradients and strong directional solidification, driven by the high 2200 W laser input. The high laser power creates a deep, hot melt pool that maintains both the pool and the substrate at elevated temperatures for long periods, resulting in slow cooling rates and high thermal gradients (G). The combination of high G and low solidification rate (R) produces a high G/R ratio, which favors elongated columnar growth with a dominant (001) texture oriented along the primary heat flow direction. In contrast, bead (b) exhibits finer, less elongated columnar grains with more random orientations. The lower laser power leads to a smaller, shallower melt pool, while the substrate remains relatively cooler, promoting faster solidification. The resulting lower G/R results finer, less elongated grains with more varied crystallographic orientations [80].

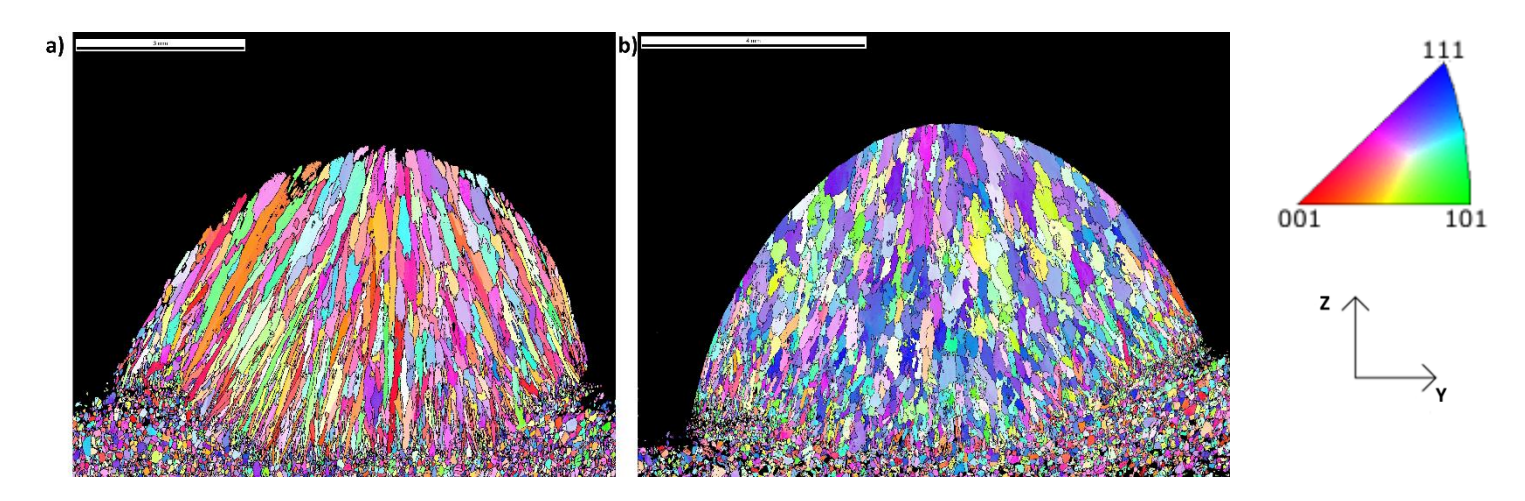


**Figure 56:** EBSD results of two beads produced with the same wire linear energy  $E_{l,w}$ = 7.9 J/mm , but with different energy proportions : a)  $P_l$ =2200W and no current; b)  $P_l$ =1000W and I=105A. Other process parameters were kept constant:  $V_s$ =1m/min,  $V_f$ =2m/min,

## **Chapter 4**

## **Conclusion and Future Work**

#### 4.1.1. Conclusion

In this work, the process–structure–integrity relationships of deposited IN718 beads were investigated for HWLAM. The presented mathematical model was used to perform an extensive experimental process mapping, covering 142 different parameter sets and a total of 450 depositions. A minimum success rate of 75% was chosen as the criterion for a successful recipe. The detailed results and analyses are presented and listed below.

- The wire linear energy value of 8.7 J/mm, obtained from theoretical calculations, was experimentally validated. The highest number of good production results was observed in the 8.5–9.5 J/mm range. It was found that current preheating should be considered more as a supplementary energy source instead of main one. In good productions, the laser provides 50% or more of the total energy, which explains this effect. At high wire feeding speeds (4–5 m/min), the number of good productions decreased, which can be attributed to the high current values. Additionally, some thermal properties of the wire were assumed to be constant in the model; at high currents, this assumption may no longer be valid due to the increased sensitivity of these properties.
- Since laser power is used as the main energy source, it becomes the dominant parameter controlling the bead geometry. Increasing the energy increases the bead while reducing its height, indicating more melting and a flatter bead on the substrate surface. Compared to laser power, current intensity has minimal to no effect on width and height of the bead.
- Highest surface roughness and waviness occurred at higher laser power and wire feeding speed, coupled with lower scanning speeds. An increase in current resulted in a decrease in both roughness and waviness while keeping the laser power intermediate.
- It was determined that penetration area is directly proportional to laser power and current intensity, and inversely proportional to scanning and wire feeding speed. Lowest dilution values are seen when the total energy input is low.
- In general, as the wire's linear energy increases, the melt pool temperature rises, which leads to longer solidification. As a result, more elongated and coarser dendritic grains are observed in the microstructure. EBSD analysis showed that when the molten pool and substrate remain hotter for longer, solidification is slower, promoting elongated and

- coarser columnar grains. In contrast, faster cooling favors finer grains with more random orientations. No internal porosity was observed in any of the beads examined with an optical microscope.
- When the HWLAM process is compared with WLAM, the addition of the current parameter enabled achieving higher deposition rates. Wire feeding speeds of 4–5 m/min became attainable. Moreover, these deposition rates were achieved with almost half the laser power compared to WLAM, indicating that the HWLAM process can enable faster production with lower energy consumption compared to WLAM. In addition, the introduction of current resulted in tracks with reduced roughness and waviness values without affecting the bead geometry, ensuring a smoother deposition without affecting the bead geometry. However, it should be noted that in depositions where laser power played a minor role in energy distribution, surface porosities were observed. As mentioned earlier, joule heating should therefore be employed as a supporting energy source.

#### 4.1.2. Future Work

In this study, detailed temperature control and analysis were not performed for the wire or the melt pool. To address this, a simulation model of the process should be developed in which all thermal material properties vary with temperature, since some were treated as constant in this work. This would improve the accuracy of the model and help reduce production errors. The model can also be validated using experimental recipes from this study.

Only single-layer depositions of 65 mm length were produced in this work. Future research should focus on applying the HWLAM process to more complex and larger components. Instead of employing a single constant current value throughout the entire process, varying current levels may be investigated. Additionally, when producing larger and more complex parts, the issue of wire tip deformation must be addressed. As discussed, after deposition the wire tip is not flat but becomes more spherical in shape, which alters the contact area between the wire and the substrate for joule heating.

# **Appendix A**

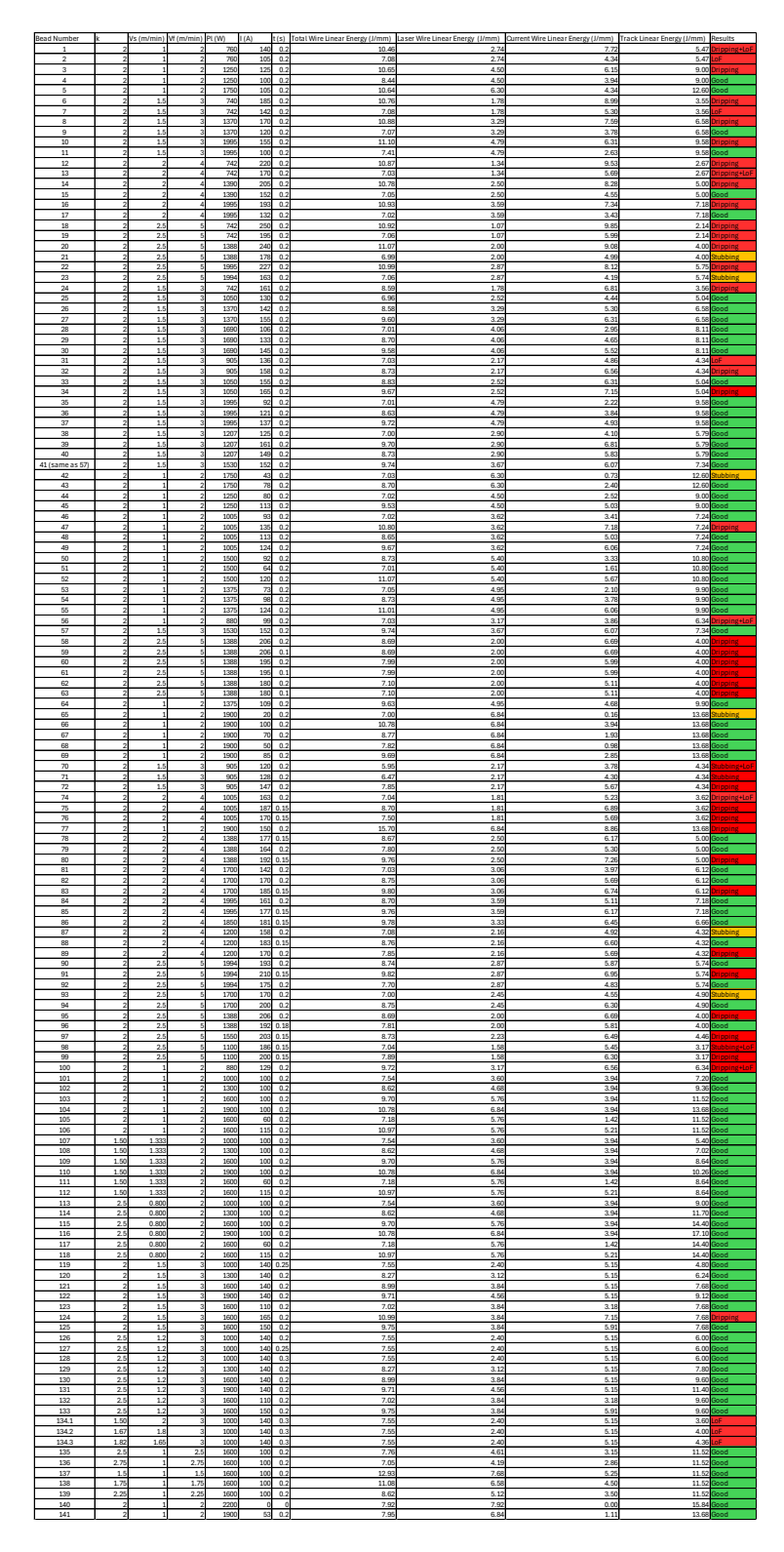


**Figure 57:** Table of all tested recipes with their process parameters and results.

# **Appendix B**

N° Bead	Real Heigth (mm)	Real Width (mm)	Model Heigth (mm)	Model Width (mm)	Error Height (%)	Error Width (%)
4	1.1193	2.8538	1.0934	2.8660	2.3	0.4
5	1.0426	3.0290	1.0333	3.0719	0.9	1.4
42	1.0430	2.9128	1.0743	2.8986	3.0	0.5
43	1.0570	2.9796	1.0468	3.0131	1.0	1.1
44	1.0808	2.9858	1.1041	2.8247	2.2	5.4
45	1.1118	2.8409	1.0876	2.8889	2.2	1.7
46 48	1.1978	2.5952	1.1362	2.7327	5.1	5.3
	1.1433 1.1199	2.7128	1.1266	2.7675	1.5	2.0
49 50		2.8306	1.1221	2.7843	0.2	1.6
	1.0801	2.8872	1.0655	2.9547	1.4	2.3
51 52	1.1322 1.1094	2.7314 2.8328	1.0825 1.0532	2.8857 3.0062	5.1	5.6 6.1
53	1.1527	2.7073	1.0915	2.8611	5.3	5.7
54	1.1240	2.9270	1.0776	2.9165	4.1	0.4
55	1.0598	2,9864	1.0666	2.9614	0.6	0.8
64	1.0843	2.8895	1.0726	2,9367	1.1	1.6
66	1.0263	3.0426	1.0218	3.1122	0.4	2.3
67	1.0251	3.0701	1.0378	3.0408	1.2	1.0
68	1.0522	3.0590	1.0532	2.9750	0.1	2.7
69	1.0410	3.0840	1.0291	3.0794	1.1	0.1
101	1.1263	2.7567	1.1335	2.7429	0.6	0.5
102	1.1072	2.8747	1.0865	2.8882	1.9	0.5
103	1.0895	2.8250	1.0506	3.0087	3.6	6.5
104	1.0077	3.1395	1.0218	3.1122	1.4	0.9
105	1.0507	2.9602	1.0743	2.9103	2.2	1.7
106	1.0352	3.0413	1.0442	3.0362	0.9	0.2
107	0.9101	2.6248	0.9172	2.6107	0.8	0.5
108	0.8593	2.8017	0.8791	2.7491	2.3	1.9
109	0.8302	2.8087	0.8501	2.8637	2.4	2.0
110	0.8532	2.8553	0.8268	2.9622	3.1	3.7
111	0.8228	2.9872	0.8692	2.7701	5.6	7.3
112	0.8527	2.8467	0.8449	2.8899	0.9	1.5
113 114	1.3965 1.2840	2.8047 2.9270	1.3361 1.2806	2.8501 3.0011	4.3 0.3	1.6 2.5
	1.2370	3.1177				
115 116	1.1783	3.11//	1.2383 1.2044	3.1263 3.2338	0.1 2.2	0.3
117	1.2288	3.0783	1.2662	3.0241	3.0	1.8
118	1.2138	3.1877	1.2308	3.1548	1.4	1.0
9	1.1097	2.7292	1.0876	2.8065	2.0	2.8
11	1.0958	2.7527	1.0316	2.9862	5.9	8.5
25	1.1812	2.5042	1.1314	2.6772	4.2	6.9
26	1.0851	2.8215	1.0796	2.8374	0.5	0.6
27	1.0618	2.8132	1.0755	2.8536	1.3	1.4
28	1.0847	2.8223	1.0570	2.9013	2.6	2.8
29	1.0652	2.8880	1.0466	2.9444	1.7	2.0
30	1.0493	2.9711	1.0427	2.9610	0.6	0.3
33	1.0568	2.8575	1.1228	2.7080	6.2	5.2
35	1.0452	2.9353	1.0354	2.9701	0.9	1.2
36	1.0353	2.9844	1.0231	3.0235	1.2	1.3
37	1.0541	2.9513	1.0176	3.0480	3.5	3.3
38	1.0854	2.7888	1.1081	2.7446	2.1	1.6
39	1.0980	2.7550	1.0960	2.7902	0.2	1.3
40	1.1286	2.6770	1.0997	2.7762	2.6	3.7
57	1.0812	2.8524	1.0574	2.9126	2.2	2.1
119	1.1104	2.7145	1.1367	2.6645	2.4	1.8
120	1.0433	2.9843	1.0895	2.8056	4.4	6.0
121 122	1.0293 0.9797	3.0282 3.1455	1.0535	2.9226	2.4	3.5
122	1.0267	3.1455	1.0247 1.0647	3.0232 2.8771	3.7	3.9 4.5
125	1.0267	3.0680	1.0504	2.9358	3.1	4.3
126-127-128	1.0183	2.8030	1.0504	2.9358	2.4	1.2
120-127-128	1.2605	3,0078	1.2842	2.7666	1.9	3.1
130	1.2225	3.0078	1.2418	3.0369	1.6	2.0
131	1.2105	3.1330	1.2078	3.1413	0.2	0.3
132	1.2305	3.0310	1.2549	2.9896	2.0	1.4
133	1.2097	3.1147	1.2381	3.0505	2.3	2.1
139	1.1263	3.0983	1.1517	3.0251	2.2	2.4
135	1.2225	3.1117	1.2503	3.0399	2.3	2.3
136	1.3212	3.1108	1.3468	3.0533	1.9	1.8
137	0.7922	3.1855	0.8394	2.9689	6.0	6.8
138	0.9203	3.1298	0.9467	2.9902	2.9	4.5
78	1.0972	2.7063	1.0804	2.7834	1.5	2.8
79	1.0388	2.8516	1.0840	2.7696	4.4	2.9
81	1.0896	2.7911	1.0556	2.8554	3.1	2.3
82	1.0421	2.9490	1.0474	2.8891	0.5	2.0
17	1.0741	2.8534	1.0319	2.9328	3.9	2.8
84	1.0290	2.9683	1.0230	2.9709	0.6	0.1
85	1.0257	3.0296	1.0188	2.9893	0.7	1.3
86	1.0283	3.0383	1.0303	2.9495	0.2	2.9
15	1.0802	2.8595	1.0873	2.7567	0.7	3.6
89	1.1043	2.6918	1.1080	2.6977	0.3	0.2
90	1.0455	2.7692	1.0249	2.9228	2.0	5.5
92	1.0174	2.9838	1.0293	2.9043	1.2	2.7
94	1.0266	2.9326	1.0500	2.8391	2.3	3.2
96	1.1143	2.5944	1.0869	2.7208	2.5	4.9

**Figure 58:** Experimental and model-predicted bead geometry values with associated error percentages. The yellow column indicates the bead track number, the blue columns represent the measured (real) height and width, the pink columns show the model-predicted height and width, and the grey columns present the corresponding percentage errors.

# **Appendix C**

**Table 11:** Measurement uncertainty for roughness and waviness parameters. The values shown represent the expanded uncertainty (±) at the 90% confidence level for each parameter. Corresponding main measurement values are reported in Section 3.2 of the main text.

Track Number	Ra (µm)	Rz (μm)	Wt (µm)	Wsm (mm)	Wq (µm)
105	0.14	0.54	7.79	2.04	1.62
103	0.11	0.29	5.73	1.85	1.37
106	0.12	0.55	4.79	0.67	0.89
137	0.05	0.25	5.88	1.12	1.57
138	0.11	0.53	2.78	1.43	0.67
139	0.10	0.42	3.84	0.66	0.74
135	0.37	1.47	5.94	0.61	1.63
136	0.09	0.24	5.34	2.71	1.40
113	0.10	0.53	2.21	1.24	0.49
114	0.07	0.28	2.95	0.39	0.57
115	0.10	0.48	3.99	0.87	1.01
116	0.43	1.69	16.06	2.14	3.63
101	0.13	0.58	4.48	2.19	1.08
102	0.09	0.41	2.89	1.35	0.65
103	0.11	0.29	5.73	1.85	1.37
104	0.20	0.92	5.07	0.86	1.09
107	0.09	0.39	3.58	0.86	0.88
108	0.10	0.39	1.93	1.03	0.48
109	0.17	0.71	2.33	0.78	0.50
110	0.23	0.92	5.70	2.04	1.16

## **Bibliography**

- [1] ISO/ASTM International, *Additive manufacturing General principles Terminology*, ISO/ASTM 52900:2021(E), 2021.
- [2] M. Abuabiah *et al.*, "Advancements in Laser Wire-Feed Metal Additive Manufacturing: A Brief Review," *Materials*, vol. 16, no. 5, 2023, doi: 10.3390/ma16052030.
- [3] I. Ribeiro *et al.*, "Framework for Life Cycle Sustainability Assessment of Additive Manufacturing," *Sustainability*, vol. 12, no. 3, 2020, doi: 10.3390/su12030929.
- [4] ISO/ASTM International, *Additive manufacturing General principles Part 2: Overview of process categories and feedstock*, ISO/ASTM 17296-2:2015(E), 2015.
- [5] S. Saleh Alghamdi, S. John, N. Roy Choudhury, and N. K. Dutta, "Additive Manufacturing of Polymer Materials: Progress, Promise and Challenges," *Polymers*, vol. 13, no. 5, 2021, doi: 10.3390/polym13050753.
- [6] M. Nirish and R. Rajendra, "Suitability of metal additive manufacturing processes for part topology optimization A comparative study," *Materials Today: Proceedings*, vol. 27, pp. 1601–1607, Jan. 2020, doi: 10.1016/j.matpr.2020.03.275.
- [7] A. Kafle, E. Luis, R. Silwal, H. M. Pan, P. L. Shrestha, and A. K. Bastola, "3D/4D Printing of Polymers: Fused Deposition Modelling (FDM), Selective Laser Sintering (SLS), and Stereolithography (SLA)," *Polymers*, vol. 13, no. 18, 2021, doi: 10.3390/polym13183101.
- [8] Clément Roch, "Intégration des spécificités d'une configuration coaxiale multifaisceaux pour la maîtrise du procédé de fabrication additive laser-fil," Université Paris Saclay, 2024. [Online]. Available: https://theses.hal.science/tel-04971085
- [9] D. Ding, Z. Pan, D. Cuiuri, and H. Li, "Wire-feed additive manufacturing of metal components: technologies, developments and future interests," *The International Journal of Advanced Manufacturing Technology*, vol. 81, no. 1, pp. 465–481, Oct. 2015, doi: 10.1007/s00170-015-7077-3.
- [10] D. Becker *et al.*, "Influence of a closed-loop controlled laser metal wire deposition process of S Al 5356 on the quality of manufactured parts before and after subsequent machining," *Production Engineering*, vol. 15, no. 3, pp. 489–507, June 2021, doi: 10.1007/s11740-021-01030-w
- [11] X. Xu, G. Mi, Y. Luo, P. Jiang, X. Shao, and C. Wang, "Morphologies, microstructures, and mechanical properties of samples produced using laser metal deposition with 316L stainless steel wire," *Optics and Lasers in Engineering*, vol. 94, pp. 1–11, July 2017, doi: 10.1016/j.optlaseng.2017.02.008.
- [12] S. Liu, W. Liu, and R. Kovacevic, "Experimental investigation of laser hot-wire cladding," *Proceedings of the Institution of Mechanical Engineers, Part B: Journal of Engineering Manufacture*, vol. 231, no. 6, pp. 1007–1020, May 2017, doi: 10.1177/0954405415578722.
- [13] G. Piscopo and L. Iuliano, "Current research and industrial application of laser powder directed energy deposition," *The International Journal of Advanced Manufacturing Technology*, vol. 119, no. 11, pp. 6893–6917, Apr. 2022, doi: 10.1007/s00170-021-08596-w.
- [14] B. Baufeld, E. Brandl, and O. van der Biest, "Wire based additive layer manufacturing: Comparison of microstructure and mechanical properties of Ti-6Al-4V components fabricated by laser-beam deposition and shaped metal deposition," *Journal of Materials Processing Technology*, vol. 211, no. 6, pp. 1146–1158, June 2011, doi: 10.1016/j.jmatprotec.2011.01.018.
- [15] L. Gao *et al.*, "Tailoring material microstructure and property in wire-laser directed energy deposition through a wiggle deposition strategy," *Additive Manufacturing*, vol. 77, p. 103801, Sept. 2023, doi: 10.1016/j.addma.2023.103801.
- [16] Y. Fu, N. Guo, G. Wang, M. Yu, Q. Cheng, and D. Zhang, "Underwater additive manufacturing of Ti-6Al-4V alloy by laser metal deposition: Formability, gran growth and

- microstructure evolution," *Materials & Design*, vol. 197, p. 109196, Jan. 2021, doi: 10.1016/j.matdes.2020.109196.
- [17] A. Heralic, "Monitoring and Control of Robotized Laser Metal-Wire Deposition," Doctoral thesis, comprehensive summary, Chalmers University of Technology, Göteborg, 2012. Accessed: Mar. 14, 2012. [Online]. Available: http://urn.kb.se/resolve?urn=urn:nbn:se:hv:diva-4206
- [18] A. Marques, B. Guimarães, F. Bartolomeu, G. Miranda, F. S. Silva, and O. Carvalho, "Multimaterial Inconel 718 Aluminium parts targeting aerospace applications: A suitable combination of low-weight and thermal properties," *Optics & Laser Technology*, vol. 158, p. 108913, Feb. 2023, doi: 10.1016/j.optlastec.2022.108913.
- [19] A. Vaicelyte, C. Janssen, M. Le Borgne, and B. Grosgogeat, "Cobalt-Chromium Dental Alloys: Metal Exposures, Toxicological Risks, CMR Classification, and EU Regulatory Framework," *Crystals*, vol. 10, no. 12, 2020, doi: 10.3390/cryst10121151.
- [20] X. Wang, X. Gong, and K. Chou, "Review on powder-bed laser additive manufacturing of Inconel 718 parts," Proceedings of the Institution of Mechanical Engineers, Part B: Journal of Engineering Manufacture, vol. 231, pp. 1890–1903, Sept. 2017, doi: 10.1177/0954405415619883.
- [21] S. Zhu, Y. Nakahara, and M. Yamamoto, "Optimization of Process Conditions for Additive Manufacturing Technology Combining High-Power Diode Laser and Hot Wire," *Metals*, vol. 11, no. 10, 2021, doi: 10.3390/met11101583.
- [22] A. Zapata, C. Bernauer, C. Stadter, C. G. Kolb, and M. F. Zaeh, "Investigation on the Cause-Effect Relationships between the Process Parameters and the Resulting Geometric Properties for Wire-Based Coaxial Laser Metal Deposition," *Metals*, vol. 12, no. 3, 2022, doi: 10.3390/met12030455.
- [23] M. Bambach, I. Sizova, F. Silze, and M. Schnick, "Comparison of laser metal deposition of Inconel 718 from powder, hot and cold wire," *Procedia CIRP*, vol. 74, pp. 206–209, Jan. 2018, doi: 10.1016/j.procir.2018.08.095.
- [24] A. G. Demir, "Micro laser metal wire deposition for additive manufacturing of thin-walled structures," *Optics and Lasers in Engineering*, vol. 100, pp. 9–17, Jan. 2018, doi: 10.1016/j.optlaseng.2017.07.003.
- [25] T. E. Abioye, J. Folkes, and A. T. Clare, "A parametric study of Inconel 625 wire laser deposition," *Journal of Materials Processing Technology*, vol. 213, no. 12, pp. 2145–2151, Dec. 2013, doi: 10.1016/j.jmatprotec.2013.06.007.
- [26] X. Xuan, "Joule heating in electrokinetic flow," *ELECTROPHORESIS*, vol. 29, no. 1, pp. 33–43, Jan. 2008, doi: 10.1002/elps.200700302.
- [27] G. Su, Y. Shi, M. Zhu, and G. Zhang, "Application of hot wire laser directed energy deposition for efficient fabrication of large nickel-based alloy components: Process, microstructure, and mechanical properties," *Journal of Materials Processing Technology*, vol. 338, p. 118789, Apr. 2025, doi: 10.1016/j.jmatprotec.2025.118789.
- [28] C. A. Biffi, J. Fiocchi, P. Bassani, and A. Tuissi, "Continuous wave vs pulsed wave laser emission in selective laser melting of AlSi10Mg parts with industrial optimized process parameters: Microstructure and mechanical behaviour," *Additive Manufacturing*, vol. 24, pp. 639–646, Dec. 2018, doi: 10.1016/j.addma.2018.10.021.
- [29] L. Caprio, A. G. Demir, and B. Previtali, "Comparative study between CW and PW emissions in selective laser melting," *Journal of Laser Applications*, vol. 30, no. 3, p. 032305, June 2018, doi: 10.2351/1.5040631.
- [30] M. Yao and F. Kong, "A review on laser cladding with wire feeding: process fundamentals, theoretical analyses, online monitoring, and quality controls," *The International Journal of Advanced Manufacturing Technology*, vol. 137, no. 9, pp. 4209–4242, Apr. 2025, doi: 10.1007/s00170-025-15447-5.
- [31] Y. Jia *et al.*, "Influence of follow-up wire feeding strategy on aluminum alloy laser wire additive manufacturing forming," *Optics & Laser Technology*, vol. 192, p. 113457, Dec. 2025, doi: 10.1016/j.optlastec.2025.113457.

- [32] S. H. Mok, G. Bi, J. Folkes, and I. Pashby, "Deposition of Ti–6Al–4V using a high power diode laser and wire, Part I: Investigation on the process characteristics," *Surface and Coatings Technology*, vol. 202, no. 16, pp. 3933–3939, May 2008, doi: 10.1016/j.surfcoat.2008.02.008.
- [33] W. U. H. Syed and L. Li, "Effects of wire feeding direction and location in multiple layer diode laser direct metal deposition," *Applied Surface Science*, vol. 248, no. 1, pp. 518–524, July 2005, doi: 10.1016/j.apsusc.2005.03.039.
- [34] W. Huang, S. Chen, J. Xiao, X. Jiang, and Y. Jia, "Laser wire-feed metal additive manufacturing of the Al alloy," *Optics & Laser Technology*, vol. 134, p. 106627, Feb. 2021, doi: 10.1016/j.optlastec.2020.106627.
- [35] Y. Chen *et al.*, "Coaxial laser metal wire deposition of Ti6Al4V alloy: process, microstructure and mechanical properties," *Journal of Materials Research and Technology*, vol. 20, pp. 2578–2590, Sept. 2022, doi: 10.1016/j.jmrt.2022.08.068.
- [36] H. Pajukoski, J. Näkki, S. Thieme, J. Tuominen, S. Nowotny, and P. Vuoristo, *Laser cladding with coaxial wire feeding*. 2012. doi: 10.2351/1.5062408.
- [37] S. Ji, F. Liu, T. Shi, G. Fu, and S. Shi, "Effects of Defocus Distance on Three-Beam Laser Internal Coaxial Wire Cladding," *Chinese Journal of Mechanical Engineering*, vol. 34, no. 1, p. 45, May 2021, doi: 10.1186/s10033-021-00560-9.
- [38] M. Motta, A. G. Demir, and B. Previtali, "High-speed imaging and process characterization of coaxial laser metal wire deposition," *Additive Manufacturing*, vol. 22, pp. 497–507, Aug. 2018, doi: 10.1016/j.addma.2018.05.043.
- [39] F. Liu, S.-S. Ji, T. Shi, L. Wan, S.-H. Shi, and G.-Y. Fu, "Parametric study of the three-beam laser inside coaxial wire feeding additive manufacturing," *The International Journal of Advanced Manufacturing Technology*, vol. 123, pp. 1–18, Sept. 2022, doi: 10.1007/s00170-022-10144-z.
- [40] J. S. Weaver, J. C. Heigel, and B. M. Lane, "Laser spot size and scaling laws for laser beam additive manufacturing," *Journal of Manufacturing Processes*, vol. 73, pp. 26–39, Jan. 2022, doi: 10.1016/j.jmapro.2021.10.053.
- [41] N. Thawari, C. Gullipalli, and V. Thammana, "Effect of Laser Spot Diameter on Melt Pool Thermal History During Laser Cladding on Inconel 718 Coatings," 2022, pp. 65–73. doi: 10.1007/978-981-16-4083-4\_6.
- [42] J. Shan, "17 Laser welding of magnesium alloys," in *Welding and Joining of Magnesium Alloys*, L. Liu, Ed., Woodhead Publishing, 2010, pp. 306–350. doi: 10.1533/9780857090423.2.306.
- [43] W. Liu, J. Ma, S. Liu, and R. Kovacevic, "Experimental and numerical investigation of laser hot wire welding," *The International Journal of Advanced Manufacturing Technology*, vol. 78, no. 9, pp. 1485–1499, June 2015, doi: 10.1007/s00170-014-6756-9.
- [44] M. Bambach, I. Sizova, F. Kies, and C. Haase, "Directed energy deposition of Inconel 718 powder, cold and hot wire using a six-beam direct diode laser set-up," *Additive Manufacturing*, vol. 47, p. 102269, Nov. 2021, doi: 10.1016/j.addma.2021.102269.
- [45] G. Su, Y. Shi, G. Li, G. Zhang, and Y. Xu, "Improving the deposition efficiency and mechanical properties of additive manufactured Inconel 625 through hot wire laser metal deposition," *Journal of Materials Processing Technology*, vol. 322, p. 118175, Dec. 2023, doi: 10.1016/j.jmatprotec.2023.118175.
- [46] H. Pajukoski, J. Näkki, S. Thieme, J. Tuominen, S. Nowotny, and P. Vuoristo, "High performance corrosion resistant coatings by novel coaxial cold- and hot-wire laser cladding methods," *Journal of Laser Applications*, vol. 28, no. 1, p. 012011, Dec. 2015, doi: 10.2351/1.4936988.
- [47] S. Zhu, Y. Nakahara, M. Yamamoto, K. Shinozaki, H. Aono, and R. Ejima, "Additive manufacturing phenomena of various wires using a hot-wire and diode laser," *Welding in the World*, vol. 66, no. 7, pp. 1315–1327, July 2022, doi: 10.1007/s40194-022-01273-w.
- [48] G. Su, Y. Shi, G. Li, G. Zhang, and Y. Xu, "Highly-efficient additive manufacturing of Inconel 625 thin wall using hot-wire laser metal deposition: Process optimization, microstructure,

- and mechanical properties," *Optics & Laser Technology*, vol. 175, p. 110763, Aug. 2024, doi: 10.1016/j.optlastec.2024.110763.
- [49] J. I. Arrizubieta, F. Klocke, N. Klingbeil, K. Arntz, A. Lamikiz, and S. Martinez, "Evaluation of efficiency and mechanical properties of Inconel 718 components built by wire and powder laser material deposition," *Rapid Prototyping Journal*, vol. 23, no. 6, pp. 965–972, Oct. 2017, doi: 10.1108/RPJ-01-2016-0012.
- [50] Z. Nie *et al.*, "Experimental study and modeling of H13 steel deposition using laser hotwire additive manufacturing," *Journal of Materials Processing Technology*, vol. 235, pp. 171–186, Sept. 2016, doi: 10.1016/j.jmatprotec.2016.04.006.
- [51] M. Yao, X. Chen, F. Kong, and W. Tong, "Process optimization of laser hot-wire cladding with high-power direct diode laser via the response surface methodology," *The International Journal of Advanced Manufacturing Technology*, vol. 120, no. 11, pp. 8089–8103, June 2022, doi: 10.1007/s00170-022-09300-2.
- [52] A. Kisielewicz *et al.*, "Hot-Wire Laser-Directed Energy Deposition: Process Characteristics and Benefits of Resistive Pre-Heating of the Feedstock Wire," *Metals*, vol. 11, no. 4, 2021, doi: 10.3390/met11040634.
- [53] B. Abranovic, E. Chang-Davidson, and J. Beuth, "Process mapping for laser hot wire additive manufacturing of Ti-6Al-4V," *Rapid Prototyping Journal*, vol. 31, Feb. 2025, doi: 10.1108/RPJ-05-2024-0216.
- [54] N. Naksuk, P. Poolperm, J. Nakngoenthong, W. Printrakoon, and R. Yuttawiriya, "Experimental investigation of hot-wire laser deposition for the additive manufacturing of titanium parts," *Materials Research Express*, vol. 9, no. 5, p. 056515, May 2022, doi: 10.1088/2053-1591/ac6ec2.
- [55] S. Liu, W. Liu, M. Harooni, J. Ma, and R. Kovacevic, "Real-time monitoring of laser hot-wire cladding of Inconel 625," *Optics & Laser Technology*, vol. 62, pp. 124–134, Oct. 2014, doi: 10.1016/j.optlastec.2014.03.007.
- [56] M. Shaikh *et al.*, "Additive manufacturing using fine wire-based laser metal deposition," *Rapid Prototyping Journal*, vol. ahead-of-print, Nov. 2019, doi: 10.1108/RPJ-04-2019-0110.
- [57] M. Akbari, Y. Ding, and R. Kovacevic, *Process development for a robotized laser wire additive manufacturing system*. 2017. doi: 10.1115/MSEC2017-2951.
- [58] F. Caiazzo, "Additive manufacturing by means of laser-aided directed metal deposition of titanium wire," *The International Journal of Advanced Manufacturing Technology*, vol. 96, no. 5, pp. 2699–2707, May 2018, doi: 10.1007/s00170-018-1760-0.
- [59] F. Caiazzo and V. Alfieri, "Directed Energy Deposition of stainless steel wire with laser beam: evaluation of geometry and affection depth," *Procedia CIRP*, vol. 99, pp. 348–351, Jan. 2021, doi: 10.1016/j.procir.2021.03.121.
- [60] J.-D. Kim and Y. Peng, "Melt pool shape and dilution of laser cladding with wire feeding," *Journal of Materials Processing Technology*, vol. 104, no. 3, pp. 284–293, Aug. 2000, doi: 10.1016/S0924-0136(00)00528-8.
- [61] D. Tyralla *et al.*, "Laser hot wire cladding (LHWC) with single and multiple wires for high deposition rates and low dilution," *Welding and Cutting*, vol. 19, pp. 220–226, Sept. 2020.
- [62] N. Ghanadi and S. Pasebani, "A Review on Wire-Laser Directed Energy Deposition: Parameter Control, Process Stability, and Future Research Paths," *Journal of Manufacturing and Materials Processing*, vol. 8, no. 2, 2024, doi: 10.3390/jmmp8020084.
- [63] A. Y. Al-Maharma, S. P. Patil, and B. Markert, "Effects of porosity on the mechanical properties of additively manufactured components: a critical review," *Materials Research Express*, vol. 7, no. 12, p. 122001, Dec. 2020, doi: 10.1088/2053-1591/abcc5d.
- [64] S. Sinha and T. Mukherjee, "Mitigation of Gas Porosity in Additive Manufacturing Using Experimental Data Analysis and Mechanistic Modeling," *Materials*, vol. 17, no. 7, 2024, doi: 10.3390/ma17071569.
- [65] M. Arana, E. Ukar, I. Rodriguez, A. Iturrioz, and P. Alvarez, "Strategies to Reduce Porosity in Al-Mg WAAM Parts and Their Impact on Mechanical Properties," *Metals*, vol. 11, no. 3, 2021, doi: 10.3390/met11030524.

- [66] R. Fu *et al.*, "Hot-wire arc additive manufacturing of aluminum alloy with reduced porosity and high deposition rate," *Materials & Design*, vol. 199, p. 109370, Feb. 2021, doi: 10.1016/j.matdes.2020.109370.
- [67] P. A. Kobryn, E. H. Moore, and S. L. Semiatin, "The effect of laser power and traverse speed on microstructure, porosity, and build height in laser-deposited Ti-6Al-4V," *Scripta Materialia*, vol. 43, no. 4, pp. 299–305, July 2000, doi: 10.1016/S1359-6462(00)00408-5.
- [68] S. Mooraj *et al.*, "Crack mitigation in additively manufactured AlCrFe2Ni2 high-entropy alloys through engineering phase transformation pathway," *Communications Materials*, vol. 5, no. 1, p. 101, June 2024, doi: 10.1038/s43246-024-00542-z.
- [69] M. Wang, N. Al-Hamdany, Y. Deng, E. Maawad, S. Luo, and N. Kashaev, "Unravelling the cracking mechanism in wire-based laser-directed energy deposition processing high-strength aluminum alloy," *Journal of Manufacturing Processes*, vol. 137, pp. 437–456, Mar. 2025, doi: 10.1016/j.jmapro.2025.01.046.
- [70] Q. Wei, Y. Xie, Q. Teng, M. Shen, S. Sun, and C. Cai, "Crack Types, Mechanisms, and Suppression Methods during High-energy Beam Additive Manufacturing of Nickel-based Superalloys: A Review," *Chinese Journal of Mechanical Engineering: Additive Manufacturing Frontiers*, vol. 1, no. 4, p. 100055, Dec. 2022, doi: 10.1016/j.cjmeam.2022.100055.
- [71] Y. Chen *et al.*, "In situ observation and reduction of hot-cracks in laser additive manufacturing," *Communications Materials*, vol. 5, no. 1, p. 84, May 2024, doi: 10.1038/s43246-024-00522-3.
- [72] A. Agazhanov, D. Samoshkin, and Y. Kozlovskii, "Thermophysical properties of Inconel 718 alloy," *Journal of Physics Conference Series*, vol. 1382, p. 012175, Nov. 2019, doi: 10.1088/1742-6596/1382/1/012175.
- [73] VDM Metals International GmbH, "VDM® Alloy 718 Nicrofer 5219 Nb." Nov. 23, 2020.
- [74] D. Basak, R. Overfelt, and D. Wang, "Measurement of Specific Heat Capacity and Electrical Resistivity of Industrial Alloys Using Sub-Second and Super-Second Pulse Heating Techniques," Oct. 2008.
- [75] Michèle Bréhier, "Synthèse de stratégies de fabrication pour la maîtrise de la microstructure des pièces produites par dépôt de matière sous énergie concentrée," Université Paris-Saclay, 2024. [Online]. Available: https://theses.hal.science/tel-04991830
- [76] G. Vander Voort, "Metallography of superalloys," vol. 70, Jan. 2003.
- [77] M. Yao, J. Sheng, F. Kong, and W. Tong, "A multi-sensor based online monitoring system for laser hot-wire surface cladding process," *Optics & Laser Technology*, vol. 177, p. 111074, Oct. 2024, doi: 10.1016/j.optlastec.2024.111074.
- [78] B. Abranovic, S. Sarkar, E. Chang-Davidson, and J. Beuth, "Melt pool level flaw detection in laser hot wire directed energy deposition using a convolutional long short-term memory autoencoder," *Additive Manufacturing*, vol. 79, p. 103843, Jan. 2024, doi: 10.1016/j.addma.2023.103843.
- [79] Y.-X. Sang, M.-Z. Xiao, Z.-J. Zhang, and Q.-Y. Fu, "Effect of auxiliary heating process on low power pulsed laser wire feeding deposition," *Materials & Design*, vol. 218, p. 110666, June 2022, doi: 10.1016/j.matdes.2022.110666.
- [80] A. Shrivastava, S. Anand Kumar, and S. Rao, "5 Postprocessing challenges in metal AM: Strategies for achieving homogeneous microstructure in Ni-based superalloys," in *Advances in Metal Additive Manufacturing*, S. Salunkhe, S. T. Amancio-Filho, and J. P. Davim, Eds., Woodhead Publishing, 2023, pp. 179–202. doi: 10.1016/B978-0-323-91230-3.00001-9.